THESIS

FROM RAIN GAUGES TO RETWEETS: USING DIVERSE DATASETS TO EXPLORE OVERLAPPING HAZARDS AND HUMAN EXPERIENCES IN LANDFALLING TROPICAL CYCLONES

Submitted by

Alexandra C. Mazurek

Department of Atmospheric Science

In partial fulfillment of the requirements

For the Degree of Master of Science

Colorado State University

Fort Collins, Colorado

Fall 2021

Master's Committee:

Advisor: Russ Schumacher

Jen Henderson
Ryan Morrison
Kristen Rasmussen

ABSTRACT

FROM RAIN GAUGES TO RETWEETS: USING DIVERSE DATASETS TO EXPLORE OVERLAPPING HAZARDS AND HUMAN EXPERIENCES IN LANDFALLING TROPICAL CYCLONES

Landfalling tropical cyclones (LTCs) are responsible for numerous hazards, including damaging winds, storm surge, inland flooding, and tornadoes. Furthermore, multiple hazards may threaten an area at the same time, which raises challenges from a prediction, warning operations, and human impacts standpoint. Previous research has approached overlapping tornado and flash flood events—which exemplify these challenges because the recommended protective actions can be in conflict—in continental systems from multidisciplinary perspectives, but less work has been done to explore these phenomena in LTC environments. Because LTCs also introduce other hazards, additional complexities may exacerbate already challenging circumstances. This work integrates meteorological and social sciences to broadly advance the understanding and implications of simultaneous flash flood and tornado events in LTCs.

Part I of this thesis investigates the relationship between two predecessors to tornadoes and flash floods—meso- to storm-scale rotation and heavy rainfall rates, respectively—using observations. Motivated by previous work that has drawn linkages between these two processes in continental convective storms, this connection is explored in Tropical Storm Imelda, a system that was among the wettest LTCs on record to impact the contiguous United States (CONUS), producing rainfall accumulations in excess of 1000 mm when it made landfall on the western Gulf Coast in September 2019. First, a synoptic and mesoscale overview of the tropical cyclone (TC) is presented as motivation for its utility in examining overlapping embedded rotation and extreme rainfall rates. Then, rain gauges from a high-density observing network in southeast Texas are analyzed alongside polarimetric radar data to compare rainfall rates that occur in the presence of embedded rotation to those that occur when no rotation is evident on radar. According to these results, 5-minute rainfall rates that followed subjectively-identified meso-γ to storm-scale rotation on radar tended to be statistically significantly greater, and when accumulated over time, more than twice as much rainfall was recorded at gauge sites when rotation was present near the gauge compared to when there was no rotation located nearby. To further quantify the spatial and temporal relationships of embedded rotation and heavy rainfall rates, quantitative precipitation estimates (QPE) and rotation tracks from the Multi-Radar Multi-Sensor system are compared in time and space. A positive correlation was found to exist between the hourly-accumulated 0-2 km rotation tracks and hourly local gauge bias-corrected QPE, suggesting that more rain tends to fall in the presence of low-level rotation.

In Part II of this thesis, social science methods are used to investigate another LTC: Hurricane Harvey (2017)—an unprecedented event that became the wettest LTC on record to impact CONUS and spawned over 50 tornadoes when it affected the western Gulf Coast. This work aims to explore the notion of experience as it evolves on Twitter in real-time during Harvey among a group of users who were located in areas that were impacted by the LTC and its overlapping hazards. Though a significant amount of research has investigated experience through surveying and interview techniques after LTCs occur, much less work has been done to study experience as it is shared live during an event or through the lens of social media. Using this motivation and drawing on the overarching theme of concurrent hazards, this research begins with a database of tweets composed during the period surrounding Hurricane Harvey that reference tornadoes and flash flooding. The sample is refined through a multi-step querying process, ultimately resulting in a group of 39 users who shared 158 tweets about “past events”—that is, events related to LTCs and/or the hazards that are associated with them. These tweets are thematically analyzed by individual users, by individual past events, and over time. The results of these analyses show that Twitter users referenced past events during Harvey for two main reasons: first, because the user has a personal connection to the event and second, because the past event is helping them to make sense of various aspects of the situation that is unfolding around them. Understanding what roles past events may play in a real-time crisis is useful to leaders and decision-makers, such as meteorologists, local politicians, and emergency managers, as it provides insight on the evolving needs and concerns of the public that they serve as they change and are modulated by various events that unfold throughout the overarching crisis.

ACKNOWLEDGMENTS

Pursuing my master's degree at Colorado State has been an incredible and challenging journey—one that would not have been possible without the support of many wonderful people.

I first want to thank my advisor, Dr. Russ Schumacher. I am extremely grateful that he gave me the opportunity to move out to Colorado to pursue this degree, and I am thankful for his guidance in my research over the past two years. I appreciate the time, patience, and encouragement he has given me, especially through the added (and unexpected) challenges that came with the COVID-19 pandemic. I also want to thank my committee member and mentor, Dr. Jen Henderson, who willingly let me participate in the social science research that she and others had already begun. She played a critical role in improving Part II of this thesis, and I am so thankful for her time and effort. I also thank my additional two committee members, Dr. Kristen Rasmussen and Dr. Ryan Morrison, for serving on my committee and offering their expertise for improving this manuscript. I would also like to thank Dr. Julie Demuth, Dr. Leysia Palen, Dr. Jennifer Spinney, and Holly Obermeier for their feedback on the social science portion of my research. Further, I want to express my appreciation to my undergraduate mentor, Dr. John Knox. He played a huge part in my initial decision to attend graduate school, and he always tried to help me see the potential in myself that I always struggled to find.

I would also like to thank the past and present members of the Schumacher research group who have been not only supportive colleagues but also friends; I am so grateful the feedback they have provided on my research over the past two years. I especially thank Dr. Erik Nielsen: it is his work that largely motivated this research, and I am very appreciative of his guidance throughout this process. I also thank other members of the Colorado State Atmospheric Science Department including professors, teaching assistants, and office staff. They have fostered my growth as a scientist in so many ways through their academic and administrative support. I additionally thank my family and friends, both in Colorado and afar. It is impossible to put into words the immense appreciation I have for them, but their love and kindness has carried me through so many challenges, whether they be academic or not. I am unbelievably grateful for their endless support.

Lastly, I'd like to express my appreciation for the funding I received during my education. This research was sponsored by an American Meteorological Society Graduate Research Fellowship (funded by the NOAA Climate Program Office) and NOAA VORTEX-SE grant NA18OAR4590308.

TABLE OF CONTENTS

LIST OF TABLES

LIST OF FIGURES

PROLOGUE

Tornadoes, flash floods, and landfalling tropical cyclones (LTCs) can all be deadly atmospheric hazards (Ashley 2007; Ashley and Ashley 2008; Rappaport 2014), but what happens when they all take place in the same location at the same time? Meteorologically, each of these phenomena are complex and nuanced on their own in several ways, including the ways in which they are understood physically and their ability to be predicted. Sociological perspectives introduce additional considerations for each hazard, such as in the ways in which they are communicated by experts, and how they are responded to by the public. Despite major strides in interdisciplinary research on each of these phenomena, there has been little to no reduction in loss of life related to these events in recent years (NOAA 2020). As challenges persist across multiple disciplines when it comes to understanding various aspects of tornado, flash flooding, and LTC events, it is reasonable to hypothesize that these issues could become amplified and complicated when multiple hazards are present. Furthermore, relative to the work that has been done on each phenomenon individually, less work has been dedicated to various pairings of these overlapping events (e.g., tornado/flash flood events, LTC/tornado events, etc.), and little to no research has sought to examine all three events in unison. These reasons motivate the need to study concurrent flash flooding and tornadoes in LTCs.

Thus, this work seeks to take a multidisciplinary approach to this gap in the literature by investigating both the physical and the human aspects of concurrent, co-located flash floods and tornadoes in the context of LTCs by focusing on two recent events: Hurricane Harvey (2017) and Tropical Storm Imelda (2019). Both systems impacted the western Gulf Coast region within approximately two years of each other, bringing overlapping hazards in the form of flooding, tornadoes, coastal surge, and destructive winds. In Part I of this thesis (Chapters 1-5), Tropical Storm Imelda is used to study the relationship between mesoscale to storm-scale meteorological features that can precede tornadoes and flash flooding. By analyzing these processes through observations, this work aims to investigate the occurrence and magnitude the relationship between the two mechanisms in an LTC environment. Part II of this work (Chapters 6-9) then explores a social science aspect of multiple hazards in LTCs. Namely, Twitter tweets collected from a group of users located in the western Gulf Coast who expressed awareness of the concurrent, co-located tornado and flash flooding that accompanied Hurricane Harvey, as well as referenced a past weather event related to LTCs and/or their hazards are studied. The goal of this analysis is to investigate the role that past experiences with weather events may play throughout a weather disaster (which is Harvey in this case) in real-time.

While the interconnectedness between the social and meteorological sides of overlapping flash flooding and tornadoes in LTCs will not be explored in detail in this manuscript, it is important to keep in mind that the two are related (e.g., forecast operations are informed by improved communication strategies and vice versa).

PART I: OBSERVATIONS OF EMBEDDED ROTATION AND EXTREME RAINFALL IN TROPICAL STORM IMELDA

In Part I of this thesis, the case of Tropical Storm Imelda is used to examine and quantify relationships between embedded rotation and heavy rainfall rates on very fine spatial and temporal scales in an LTC environment. Embedded rotation has already been shown to impact extreme rainfall in model simulations, but identifying whether this relationship holds true in the real-world observations is crucial. Further, if the relationship does exist, it is important to quantify the magnitude of it. Making sense of the strength of the connections that exist between these interacting physical phenomena can not only further understanding of the environments that produce tornadoes and flash flooding, but it can also add insight to short-term forecasting and nowcasting during forecasting operations when the threat of these overlapping hazards exists in LTCs.

Given this motivation, the study presented in Part I aims to address the following goals:

1) *to identify the multiscale processes that contributed to Imelda's excessive rainfall*

2) *to explore the spatiotemporal relationship between embedded mesoscale/storm-scale rotation and the extreme rain rates that occurred during Imelda using observations*

3) *to quantify the magnitude and identify the significance of the relationship between embedded rotation and rainfall rates based on these observations*

CHAPTER 1: INTRODUCTION AND MOTIVATION

This literature review broadly covers flash flooding and tornadoes in the context of landfalling tropical cyclone (LTC) environments, particularly in the contiguous United States (CONUS). First, the physical mechanisms associated with each hazard are discussed individually, both in LTC environments and continental convective systems. Then, previous work that has explored the relationships between tornadoes and flooding and their driving forces (in particular, mesoscale rotation and extreme rainfall rates) is considered. It is intended that this literature review will help demonstrate the need to examine heavy rainfall and embedded rotation in tropical cyclones (TCs). With this previous research considered, the motivation and research goals for this work are presented, followed by a brief outline for the remainder of Part I of this manuscript.

1.1 Basics of Flash Flood-Producing Rainfall

Before discussing flood-producing rainfall in the context of LTCs, it is first helpful to briefly review some of the basic mechanisms that drive excessive precipitation and resultant flooding in the first place. Flash flood events are caused almost exclusively as a result of heavy rainfall (as opposed to surface hydrology-related phenomena such as ice jams or dam failures) (Dougherty and Rasmussen 2019), which has long motivated their interconnectivity in the literature. While the source of flash flooding almost always originates with the atmosphere, hydrology[1] remains important, as it helps govern whether heavy rainfall becomes flash flood-producing heavy rainfall or not (e.g., Doswell et al.

[1] The importance of surface properties should not be minimized, though the focus of this literature review will focus on flash flooding in the context of heavy rainfall.

1996; Davis 2001; Schumacher 2017). This interplay between the atmosphere and the surface makes flash flood forecasting particularly challenging. Still, even by focusing on the heavy rainfall component alone, predictability is very complex (Sukovich et al. 2014). These challenges exist for several reasons, such as that atmospheric patterns can often appear benign or uninteresting ahead of flash flood events (Doswell et al. 1996) or that characteristics of the storms that produce flash flooding, such as their accumulations, rain rates, and relative frequency, can vary significantly by region (Dougherty and Rasmussen 2019).

One of the most straightforward approaches to flash flood forecasting that can be applied to any rainfall-producing system (regardless of location or convective mode) is the ingredients-based approach proposed by Doswell et al. (1996). In their method the accumulated precipitation (P) is defined as:

$$P = \bar{R}D \qquad \text{(Eq. 1.1)}$$

where $\bar{R}$ is the average rainfall rate and D is the duration over which the rain falls. At an instantaneous point in time, $\bar{R}$ becomes R, which is the instantaneous rain rate. For a given location, R is a function of precipitation efficiency (E) vertical ascent rate (w) and the ambient mixing ratio (q):

$$R = Ewq \qquad \text{(Eq. 1.2)}$$

Together, wq is defined as the vertical moisture flux. Thus, Eqs. 1.1-1.2 show that as precipitation efficiency—defined by Doswell et al. (1996) as the ratio of rainfall to water vapor influx—and vertical moisture flux increase, instantaneous rainfall rate also increases, which would subsequently increase $\bar{R}$ and ultimately P (all else being equal).

In addition to the factors that influence precipitation rate, the environments and patterns that lead to flash flood-producing rainfall are also important. One of the first attempts at classifying such environments was performed by Maddox et al. (1979), which found that common surface patterns associated with flash flood-producing systems include "frontal" (heavy rainfall in the cool sector ahead of a warm front), "mesohigh" (heavy rainfall along thunderstorm outflow), and "synoptic" (heavy rainfall in the warm sector of a warm front, ahead of a cold or stationary front) events. In all three of these archetypes, there is some kind of surface boundary present that serves as a lifting mechanism. In the mid-levels, shortwave troughs have been shown to be a common feature upstream of flash flood-producing systems, as they can provide synoptic-scale forcing for ascent (e.g., Maddox et al. 1979; Doswell et al. 1996; Davis 2001). High moisture content, particularly at the surface and throughout the lower troposphere, is also a key ingredient for flash flood-producing storms (e.g., Maddox et al. 1979; Doswell et al. 1996). This moisture can be enhanced or sustained when there is a low-level jet (LLJ) present, which serves as a transport mechanism for warm, moist air (e.g., Maddox et al. 1979; Davis 2001).

Mesoscale convective systems (MCSs) have been shown to be the system type that is responsible for the majority of heavy precipitation events in much of CONUS, particularly in the warm season (Schumacher and Johnson 2006). However, not all MCSs are capable of producing flash flooding, with the primary reason being that the translational speed can be fast (hence limiting the D component of the basic equation for flash flood-producing rainfall). A critical factor that governs how much rain a MCS will produce and how long it will last is the orientation of the precipitation shield relative to the direction of the system's motion (Doswell et al. 1996). For instance, if the major axis of the MCS is parallel to the system's motion, the duration of rainfall for a given location within the precipitation field would be greater than it would be if the major axis of the system was perpendicular to the system's direction of motion. This concept is illustrated in Fig. 1.1..

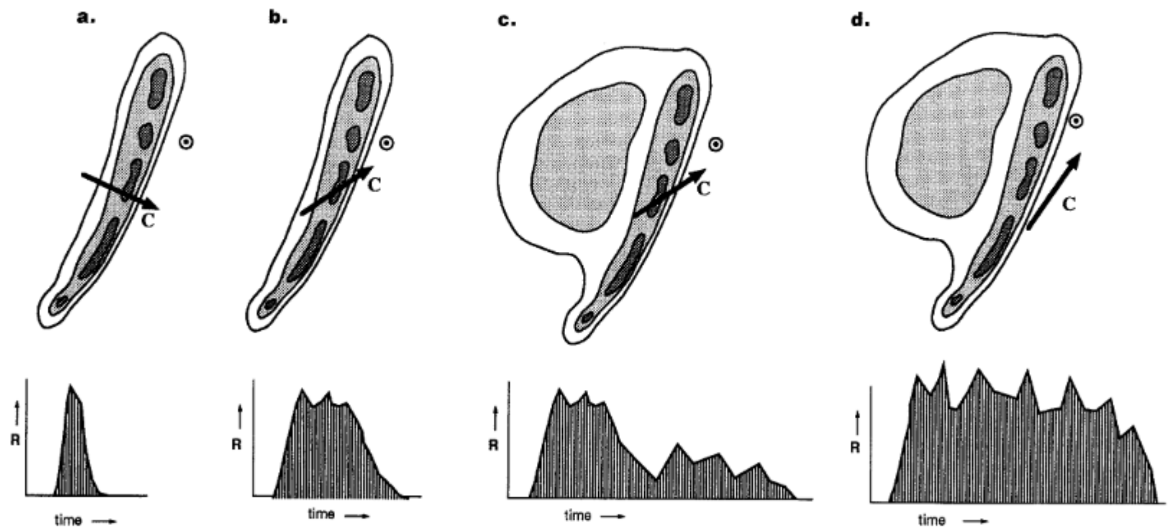

Figure 1.1: Schematic detailing the dependency of the rain rate (R) and duration of a convective system on the orientation of the system relative to the direction of system motion, from Fig. 3 in Doswell et al. (1996). The top row of plots show the convective systems (with darker shading representing higher reflectivity), the system's direction of travel (shown by the arrows labeled with "C"), and a given location that the system will impact (small circle). The bottom row of plots shows the idealized R over time that corresponds to the location being impacted by the system shown in the diagram above each respective plot.

In addition to the system motion of MCSs, the motion of the cells within the system relative to the development of new cells (i.e., the cell propagation) is also important to consider when discussing flash flood potential for a given system. Quasi-stationary motion can occur when there is near-cancellation of the cell motion and cell propagation vectors within a system (Fig. 1.2a) (Chappell 1986; Doswell et al. 1996; Schumacher and Johnson 2005). This nearly-stationary motion can cause rain to fall over the same locations for many hours, which can result in localized flash flooding. In MCSs, systems that have persistent upstream development of new convection relative to the cell motion vector are classified as "backbuilding" MCSs (Fig. 1.2b) (Schumacher and Johnson 2005).

Climatologically, backbuilding MCSs have been shown to be the second-most common type of system responsible for producing extreme rainfall (specifically, across the eastern 2/3 of CONUS) (Schumacher and Johnson 2006). One way that backbuilding convection has been shown to form is through the interaction of a LLJ impinging on a mid-level low, which can provide lift, and shear that can help sustain convection (Schumacher and Johnson 2009). Quasi-stationary surface boundaries, such as storm outflow or cold pools, have also been shown to be an important component in maintaining backbuilding convection, as it can help to lift and destabilize warm, moisture-rich air that collides with the boundary (e.g., Schumacher and Johnson 2005; Keene and Schumacher 2013). Though larger-scale aspects of the environments that have been shown to support backbuilding convection are consistent with other heavy rainfall-producing systems (e.g., moderate instability, moisture transport by a LLJ, presence of vertical wind shear), localized, storm-scale processes are regarded as being more important (e.g., Schumacher and Johnson 2005). These mechanisms have been studied almost exclusively in continental systems, though back-building convection has been documented within TCs as well (Wang et al. 2015).

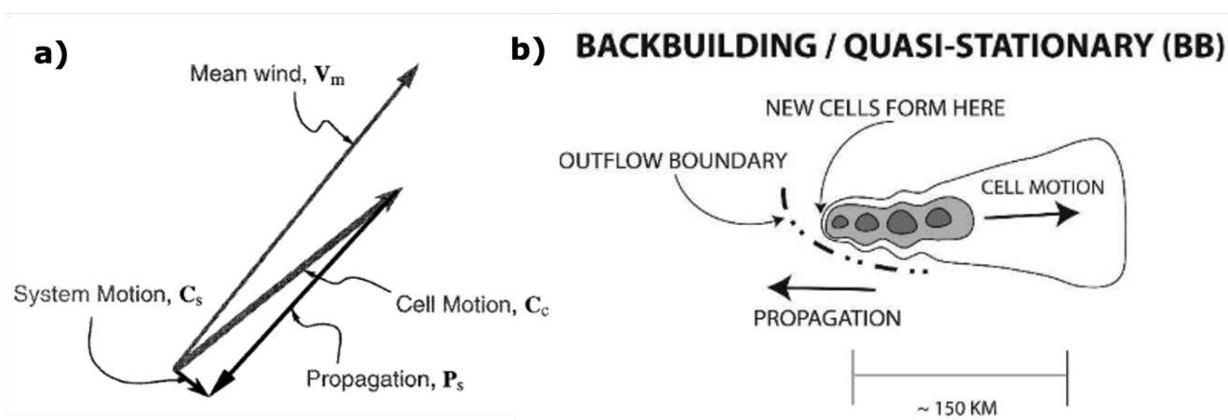

Figure 1.2: Schematics showing mean wind, cell propagation, and cell motion vectors that lead to nearly stationary storm motion from Fig. 4 in Doswell et al. (1996) (a) and back-building structure in mesoscale convective systems from Fig. 3 in Schumacher and Johnson (2005) (b).

1.2 Heavy Rainfall in Landfalling Tropical Cyclones

LTCs can bring extreme rainfall accumulations. They contribute significantly to yearly rainfall in CONUS, accounting for upwards of 15% of annual summer rainfall in some coastal locations (Larson et al. 2005). They also make a noticeable contribution to extreme rainfall events, and this contribution has been shown to be increasing over time in some areas (e.g., Knight and Davis 2009). To examine rainfall in LTCs, the simple formula for heavy rainfall provided by Doswell et al. (1996) (i.e., Eq. 1.1) will provide a framework for the discussion below.

Beginning first with duration (D), the time component of heavy rainfall has been at the center of LTC rainfall-related discussions in recent years, particularly in regard to observed changes in their translational speed (e.g., Kossin 2018; Hall and Kossin 2019) and the time it takes them to decay over land (Li and Chakraborty 2020). On a global scale, forward speed of TCs have generally decreased over the past several decades, with a particularly pronounced slowdown occurring inland over North America (Kossin 2018). Over a similar time frame, North Atlantic TCs have also demonstrated a greater propensity to stall near the coast, which is hypothesized to be a result of both reduced translational speed and an increased frequency of sudden changes in LTC direction (Hall and Kossin 2019). Once inland, LTCs have also been shown to be decaying at a slower rate, which is thought to be the result of warmer sea surface temperatures providing more moisture to LTCs before they move inland, which helps them maintain their intensity (Li and Chakraborty 2020). The obvious implication of reduced translational speeds and slower weakening of LTCs is that duration of LTC-related rainfall would increase both along the coast and inland, which would increase the threat for heavy rainfall (all else being equal). Furthermore, translational speed may even be one of the main governing factors in determining rainfall amounts, since LTCs that are the slowest-moving tend to produce the highest storm-total rainfall amounts (Galarneau and Zeng 2020). This slow system speed that leads to long duration events is also perhaps a reason why LTCs are associated with hybrid flooding (which consists of both flash and slow-rise flooding) (Dougherty and Rasmussen 2019).

In addition to duration, the second component of Eq. 1.1 (rain rate) is also an important factor in rainfall accumulations produced by LTCs. Moisture content is one factor that influences rain rate (i.e., it is a positive relationship), and it is an ingredient that is very abundant in LTCs, as evidenced by their high precipitable water values. In an extreme example, precipitable water values in Hurricane Harvey (2017)—the wettest storm on record to impact CONUS—were shown to be several standard deviations above the climatological mean for the area, which persisted for several days after it made landfall (e.g., Brauer et al. 2020; Galarneau and Zeng 2020). For a broader perspective, it appears that among precipitable water values associated with LTCs, many of the heaviest rainfall-producing systems (which were also often the slowest-moving) typically have area-mean values that remain above at least the 50th percentile for several days after landfall (Galarneau and Zeng 2020). In addition to high precipitable water, high precipitation efficiency also plays a role in enhancing rain rates (Eq. 1.2). In LTCs, strong horizontal moisture flux convergence as well as rich warm rain processes have been shown to increase precipitation efficiency (Brauer et al. 2020). The collocation of quasigeostrophic forcing for ascent with LTC environments has also been shown to further advance rainfall production (Galarneau and Zeng 2020) by providing additional lift that can support precipitation formation. In terms of the role that rainfall rate in LTCs may play in the future, there is new evidence that suggests that rainfall rates in northern hemisphere LTC rainbands are increasing, in part as a result of increasing precipitable water values in the systems (Guzman and Jiang 2021). This finding highlights that moisture availability and other factors influencing rainfall rates should perhaps be given the same attention as translational speeds and inland system longevity when examining LTC-related rainfall.

1.3 Tornadoes in Landfalling Tropical Cyclones

Tornadoes are a relatively frequent phenomenon that accompany LTCs, with 76 occurring on average each year (Edwards 2010, according to a 1995-2009 climatology). Several climatologies have sought to capture the various spatial, temporal, and intensity characteristics of LTC tornadoes, both in CONUS (e.g., Hill et al. 1966; Novlan and Gray 1974; McCaul 1991; Schultz and Cecil 2009; Edwards 2010; Moore and Dixon 2011; Edwards 2012; Moore et al. 2017) and internationally (e.g., Fujita et al. 1972; Bai et al. 2020). With regards to intensity, the vast majority of LTC-spawned tornadoes tend to be "weak" (i.e., rated F/EF0 or F/EF1) and short-lived (e.g., Schultz and Cecil 2009; Moore and Dixon 2011; Edwards 2012; Moore et al. 2017), with "strong" tornadoes (i.e., those rated F/EF2 or higher) making up a smaller percentage of LTC tornadoes compared to non-LTC tornadoes (Schultz and Cecil 2009). LTC tornadoes also tend to be smaller in diameter and have shorter path lengths relative to tornadoes not associated with LTCs (e.g., Moore and Dixon 2011; Edwards 2012), though LTC tornadoes that are stronger and have longer path lengths tend to occur disproportionately at locations that are at higher latitudes and further from coastlines (Moore et al. 2017). Indeed, LTC tornadoes can occur several hundred kilometers inland, though they most often occur within a couple hundred kilometers of the coast (e.g., Hill et al. 1966; Novlan and Gray 1974;

Schultz and Cecil 2009; Moore and Dixon 2011; Edwards 2012; Moore et al. 2017). There is very high consensus among these same studies that tornado activity tends to be concentrated in the northeast quadrant of the LTC from an earth-relative perspective and/or the front-right quadrant (FRQ) from the perspective of the LTC's translational motion. Many times, these quadrants are very closely co-located. However, in the storm-relative framework, elevated tornadic activity in the FRQ may be less likely in LTCs that experience abrupt or deviant motion (e.g., Edwards 2012). Temporally, the height of TC tornado activity takes place in the early afternoon to early evening hours and roughly within the first day of landfall (e.g., McCaul 1991; Schultz and Cecil 2009; Moore and Dixon 2011; Edwards 2012).

The number of tornadoes associated with LTCs is extremely variable, with some systems producing zero tornadoes and others producing over 100 (e.g., Schultz and Cecil 2009; Moore and Dixon 2011; Edwards 2012). Many studies have linked tornado productivity to features of the LTC itself, such as its intensity at landfall (e.g., Hill et al. 1966; Novlan and Gray 1974; Verbout et al. 2007; Moore and Dixon 2011). However, comprehension of the environmental characteristics that are favorable for LTC-spawned tornadoes is perhaps more useful from a predictability standpoint.

This review of tornadic LTC environments begins first with dynamic patterns in the mid- to upper-levels. Early research suggested that LTCs with a northeasterly trajectory tended to spawn more tornadoes, but the reason was not particularly clear as to why (Hill et al. 1966; Novlan and Gray 1974). With later research recognizing the importance of mid- and upper-level winds in steering TCs, especially for systems that are strong (e.g., Velden and Leslie 1991), patterns in troughs and ridges began to be investigated in more detail. At 500 hPa, one common large-scale pattern found for tornado-producing LTCs (specifically those making landfall along the Gulf Coast) is a trough located over the western CONUS (Verbout et al. 2007; Cohen 2010; Moore and Dixon 2015). As the trough begins to progress eastward, the Gulf Coast LTC can begin to interact with its ascending branch and the stronger winds associated it, which ultimately helps the system recurve towards the east (Verbout et al. 2007) and gives it the northeast trajectory that was noted by early scientists. For LTCs that become fully embedded in the midlatitude westerlies, tornado production can be even more prolific (Moore and Dixon 2015), particularly if the system is in a favorable region (i.e., right-entrance or left-exit) of an upper-level jet streak (Cohen 2010; Moore and Dixon 2013). This feature was present during Hurricane Harvey (Galarneau and Zeng 2020), which likely played some role in supporting the tornadic environment during that event. One reason that the ascending branch of the mid-level trough and the upper-level jet streak are thought to be important characteristics in fostering tornadic development in LTCs is because they support synoptic-scale rising motion (Verbout et al. 2007; Cohen 2010; Moore and Dixon 2013, 2015), which is an important feature that contributes to convective development.

Moisture, instability, and vertical wind shear are other factors that must be considered in any tornadic environment, including those associated with LTCs. It has long been acknowledged that strong wind shear, particularly in the low levels, is essential in LTC tornadogenesis because instability often suffers due to high moisture content and dense cloud cover in those environments (e.g., Novlan and Gray 1974; McCaul 1991). Indeed, compared to non-LTC tornadic environments, LTC tornadic environments tend to be characterized as having less instability, lower lapse rates, higher moisture content, and stronger low-level vertical wind shear (e.g., Edwards et al. 2012). Fig. 1.3 shows a statistical comparison of a few parameters that are pertinent to historical tornadic environments (i.e., mixed-layer convective available potential energy (MLCAPE), 0-1 km above ground level storm relative helicity (SRH), precipitable water, and mid-level lapse rates) in LTC and non-LTC cases. One

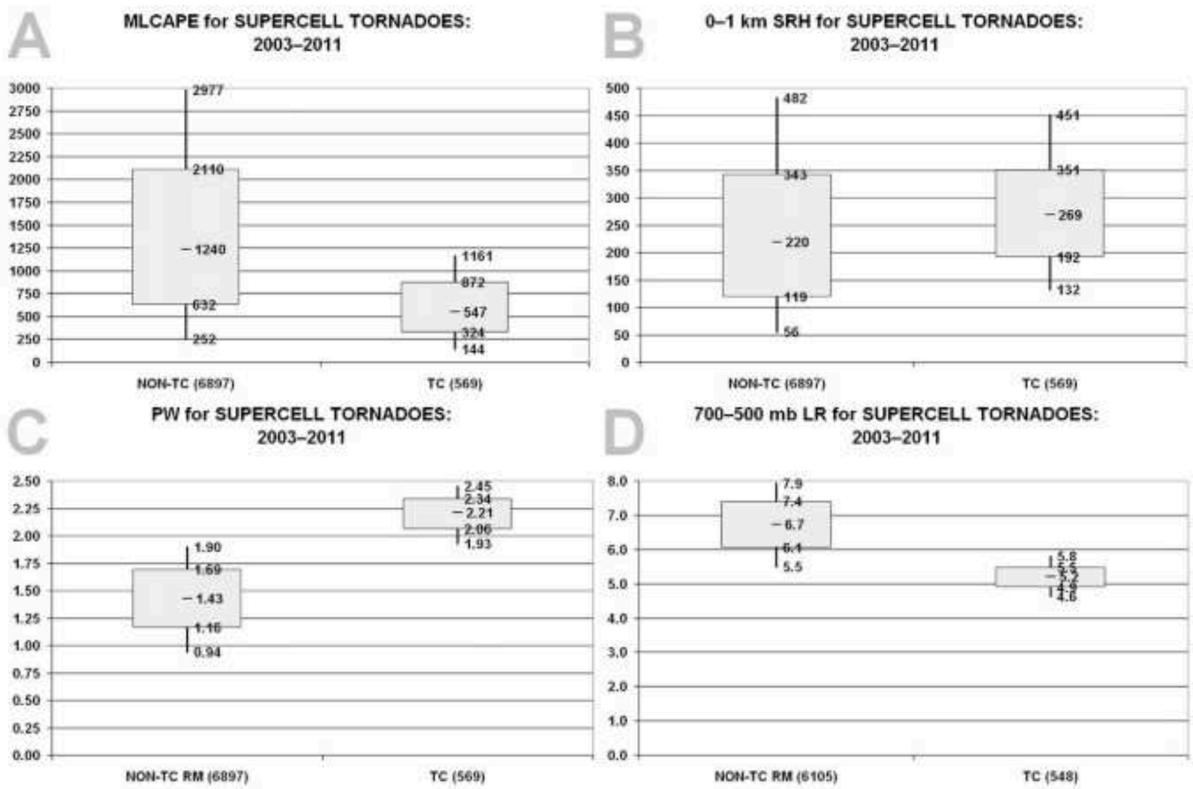

Figure 1.3: Statistical comparison of some environmental parameters for non-landfalling tropical cyclone supercellular tornadic (left boxplot in each subplot) environments and landfalling tropical cyclone supercellular tornadic environments (right boxplot in each subplot) from Fig. 8 in Edwards et al. (2012). The parameters being shown are mixed-layer convective available potential energy (J kg^{-1}) (a), 0-1 km above ground level storm relative helicity (m^2 s^{-2}) (b), precipitable water (inches) (c), and 700-500 hPa lapse rate (°C km^{-1}) (d). The ends of the whiskers and associated annotated values correspond to the 10th and 90th percentiles of the dataset, the edges of the boxes and annotated values correspond to the 25th and 75th percentiles, and the central value is the 50th percentile. Environmental classification type and sample sizes are included in parenthesis along the x-axes.

of the most obvious differences in this figure is moisture content, where the 10th percentile of precipitable water in LTC tornado environments is greater than even the 90th percentile of precipitable water in non-LTC tornado environments. The values of MLCAPE and 700-500 mb lapse rates in tornadic LTC environments are also noticeably low compared to the values in tornadic non-LTC environments, further demonstrating the limited instability and buoyancy that is present in tornado-producing LTCs. However, as stated previously, stronger low-level wind shear in tornadic TC environments compared to non-tornadic TC environments can help compensate for the lower instability. In addition the stronger low-level shear, enhanced deep-layer (i.e., 0-6 km) vertical wind shear on very localized scales in LTC environments also seems to play a role in determining which convective elements with velocity-derived storm-scale rotation (specifically, that is consistent with tornadogenesis) will ultimately produce a LTC tornado.

Two of the main components in tornadogenesis, vertical wind shear and instability, can be impacted as a result of interaction between broader synoptic-scale processes and LTCs. For example, deep-layer shear, which has been argued to be important for tornadogenesis in LTC environments since it promotes mesocyclogenesis, can be enhanced by the mid- to upper-level troughs that were discussed previously (e.g., Verbout et al. 2007; Moore and Dixon 2013, 2015). This pattern helps to foster veering vertical wind profiles that promote supercellular convection (e.g., McCaul 1991; Verbout et al. 2007; Moore and Dixon 2015). However, mesocyclones are generally weaker overall in LTC tornadic environments compared to non-LTC tornadic environments (e.g., Edwards et al. 2012), and the magnitude of the effect that the strength of the deep-layer shear has on the number of tornadoes produced in LTC tornadic environments has been found to range from neutral to positive (e.g., Verbout et al. 2007; Cohen 2010; Edwards 2012; Moore and Dixon 2015), which does bring into question its relative importance compared to low-level shear for tornadogenesis in LTCs. Shifting focus to synoptic-scale effects on thermodynamics, dry air entrainment can help counteract the lack of instability in LTC environments by helping to destabilize the atmosphere. Specifically, LTC environments that support tornadoes often show signs of dry air entrainment between 700 hPa and 500 hPa, which works to steepen mid-level lapse rates and decrease cloud cover (allowing for additional surface heating), both of which increase positive buoyancy (e.g., Curtis 2004; Cohen 2010; Moore and Dixon 2013). This dry air, typically seen as a horizontal moisture gradient, often exists to the north or northwest relative to the center of circulation of the LTC, where it can then be mixed in to the system (e.g., Curtis 2004; Cohen 2010).

1.4 Relationships Between Tornadoes and Flash Flooding

Though many studies have sought to understand tornado and flash flood-producing rainfall environments independently, fewer have considered where, when, and how they might occur together. Though most research on the meteorological aspects of the subject has occurred within the 21st century, concern related to the forecasting and communication of the combined threat of flash flooding and tornadoes has existed for many decades. As Maddox et al. (1979) writes in their early paper on flash flood forecasting: "if severe thunderstorms [storms that produce damaging winds, and/or hail and/or tornadoes] occur in association with the heavy precipitation event, forecaster concern for flash flood possibilities may become subordinate to that caused by other aspects of the storms" and that when they both occur, the "forecast office must contend simultaneously with both severe storm and flash flood problems" (p. 117-8). Doswell (1998) expresses similar sentiments in the context of supercell thunderstorms, articulating concern that forecasters may be more focused on their severe hazards rather than their flash flood potential. Recent work has suggested that these concerns are legitimate, as it has been shown that forecasters may unintentionally focus on the tornado risk over the flash flood risk during warning operations when they occur simultaneously (Henderson et al. 2020).

Several studies have discussed the concurrence and/or co-location of tornadoes and flash flooding broadly using relatively loose definitions (e.g., Schumacher and Johnson 2006) or have highlighted their coexistence in specific events (e.g., Rogash and Smith 2000; Smith et al. 2001; Bluestein et al. 2015). Other work, however, has offered more explicit definitions. For example, Rogash and Racy (2002) selected their cases by requiring at least one F3+ or two F2 tornadoes to occur within 250 km and +- 3 hours of "significant flash flood reports". Later, Nielsen et al. (2015) coined the term "TORFFs" to describe the overlapping existence of tornadoes and flash flooding and provided two definitions of them using specific spatial and temporal constraints. The first definition identifies a TORFF event by the spatial overlap in a storm-based tornado and storm-based flash flood warning that occurs within a relatively small time frame (≤ 30 minutes) (Nielsen et al. 2015). This definition has been applied in other recent studies in the context of forecasting practices (e.g., Henderson et al. 2020) and TC environments (Burow et al. 2021). The second method for TORFF identification classifies a TORFF event by the co-location of a confirmed tornado path and a flash flood observation within a short amount of time (3 hours) (Nielsen et al. 2015). As Nielsen et al. (2015) notes, the former of these methods inherently overcounts TORFF occurrences (i.e., every tornado warning and flash flood warning will not produce a verified event), while the latter method undercounts TORFF events by requiring that the tornado path and flash flood observation overlap perfectly (i.e., cases where the phenomena occur very near each other but do not overlap are excluded).

In order to forecast potential TORFF events, understanding how and why TORFFs occur are crucial steps that must be taken. Climatologically, TORFF events have been shown to occur with several types of convective systems, including MCSs, LTCs, discrete cells, and synoptic-scale frontal systems (Rogash and Racy 2002; Nielsen et al. 2015). Rogash and Racy (2002) found that TORFF environments (see previous paragraph for their definition of TORFF events) shared similar features at the surface and in the mid-levels with flash flood-producing environments, and their study even modeled their environmental classification scheme after the one proposed for flash flooding by Maddox et al. (1979) (i.e. synoptic, frontal, and mesohigh). One difference that their study did find, however, is that environments that produced tornadoes and flash flooding tended to have a deep mid-tropospheric trough to the west of where the phenomena took place, whereas a weaker upstream trough can be sufficient in many flash flood-only environments, as detailed by Maddox et al. (1979). TORFF environments also have been shown to resemble tornadic environments in terms of ingredients (e.g., low-level vertical wind shear, instability), though the magnitudes of the ingredients tend to differ: that is, TORFF environments tend to have more moisture in the lower troposphere, greater forcing on the synoptic scale, and stronger vertical wind shear compared to tornadic environments (Nielsen et al. 2015). While these differences should be noted, TORFF environments remain complex and difficult to distinguish from tornado-only or flash flood-only environments. Further, these studies predominately explicate these features in continental convective systems, so questions remain as to what these characteristics may look like in LTC environments.

Additional insights on TORFF events can be gathered at the storm-scale. Early discussions surrounding this topic have begun with supercell thunderstorms—a convective mode frequently associated with tornadogenesis or other severe hazards, though considered far less often for their flash flood potential (e.g., Doswell 1998). This notion that supercells do not produce heavy rainfall is not necessarily incorrect, as supercells tend to have fast translational speeds (e.g., Doswell 1998; Smith et al. 2001) and small precipitation footprints (specifically when in the form of discrete cells, rather than when embedded within a larger convective system). Despite these typical characteristics, supercells are capable of producing short-term heavy rainfall (e.g., Doswell 1998; Smith et al. 2001; Hitchens and Brooks 2013; Bluestein et al. 2015). This is especially true when the storm is a high precipitation (HP) supercell, which are characterized as having a mesocyclone located directly above the precipitation shield rather than above a non-precipitating or low-precipitating part of the cell (a feature that occurs in a "classic" supercell) (Moller et al. 1994). In general, supercells have been shown to be more likely than non-supercellular thunderstorms to produce short-term heavy to extreme rainfall rates (Hitchens and Brooks 2013), and they can have high precipitation efficiencies (Brauer et al. 2020). From an impacts standpoint, it has been shown that both flash flooding and tornadoes can occur not only within the same storm systems (e.g. Rogash and Smith 2000; Smith et al. 2001), but even within the same supercell (e.g. Bluestein et al. 2015),which further illustrates that these dual-hazards can exist in close proximity to each other (in both a spatial and temporal sense).

Knowing that supercells can generate extreme rainfall, more recent studies have begun to examine storm-scale dynamics in an effort to understand interconnected factors that might be precursors to flash flooding and tornadogenesis. Eq. 1.2 shows that vertical motion is positively correlated with increased rain rates (Doswell et al. 1996), and this ingredient is also a key component of tornado-producing convection. Nielsen and Schumacher (2018) demonstrated through model simulations that vertical wind shear-driven low-level rotation can act to increase rainfall production by enhancing upward vertical velocity. More specifically, their study showed that low-level, meso-γ scale rotation increases with increasing vertical wind shear, which enhances upward vertical accelerations, effectively lifting parcels to saturation that would have been otherwise stable. This relationship between small-scale rotation and heavy rainfall has also been examined in observations. Nielsen and Schumacher (2020a) showed that in continental convective systems, more rain tended to fall when there was rotation present in the precipitating system. In tropical systems, storm-scale rotation occurring in embedded supercells has been shown to be co-located with locally-heavy rainfall accumulations (Brauer et al. 2020), further suggesting a positive association between meso- to storm-scale rotation and rain rates.

TORFF events are challenging to predict and communicate (given the conflicting recommended protective actions that are associated with them) but understanding them is important given how often they occur. From a storm-based warnings perspective, Nielsen et al. (2015) found that TORFF events occur on average over 400 times per year across all modes of convective systems in CONUS. Fig. 1.4 (from Nielsen et al. 2015) illustrates the nearly 3000 TORFF events that were documented over a 6-year period. The graphic in Fig. 1.4 shows that TORFF events are relatively common for almost any location east of the Rockies, indicating that this type of overlapping hazard is pertinent to a large number of individuals. In LTCs specifically, TORFF events are also not unusual. Burow et al. (2021) notes, however, that the spread in number of TORFF events is large for a given LTC, ranging from over 200 events to zero. While their study does offer some basic spatial characteristics of TORFF events in LTCs (e.g., they occur in the rear-right quadrant of LTCs relative to their translational direction of motion), their work does not discuss environmental characteristics that may favor their development in LTCs.

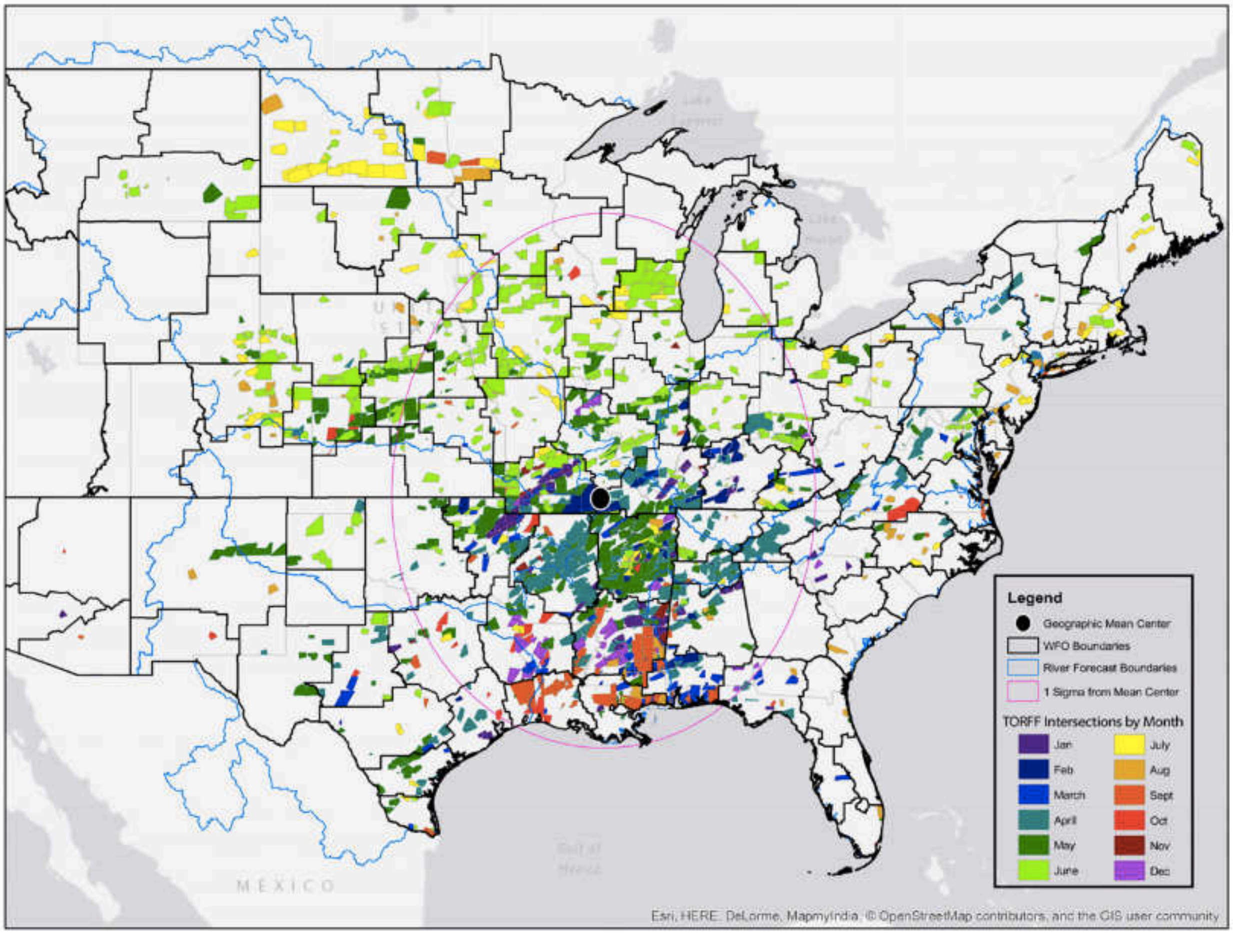

Figure 1.4: Co-located, concurrent tornado and flash flood warnings (TORFFs) colored by month for 2008-2014 from Fig. 6 in Nielsen et al. (2015). The black dot represents the mean center of the warning overlaps, with the pink ellipse representing one standard deviation from the mean center.

1.5 Motivation

This literature review demonstrates that there has been extensive research done to examine the environmental characteristics and physical mechanisms that contribute to flash flood-producing rainfall and tornadoes *individually* in LTCs. A few studies have investigated the environments and meteorological mechanisms that may precede the development of these concurrent, co-located hazards in non-TC cases. However, much less work has been done to investigate overlapping tornado and flash flooding events in LTCs specifically. This study aims to improve the understanding of the relationship between these two hazards in LTCs by examining the connection between embedded meso- to storm-scale rotation and extreme rainfall rates in LTCs. In order to support this goal, this study provides a close examination of several observational datasets in the case of Tropical Storm Imelda. Using several different methods, this work aims to 1) examine the multiscale processes that contributed to Imelda's excessive rainfall, 2) explore the spatiotemporal relationship between embedded mesoscale/storm-scale rotation and the extreme rain rates that occurred during Imelda using observations, 3) identify the magnitude and significance of this relationship. Broadly, these goals will help further the understanding of the relationship between meso- to storm-scale rotation and heavy rainfall, specifically in LTC environments.

The remainder of Part I proceeds as follows. Chapter 2 provides a synoptic and mesoscale analysis of Tropical Storm Imelda and offers motivation for its use in studying the relationship between heavy rainfall rates and embedded mesoscale rotation in Chapters 3 and 4. A subjective and statistical analysis of radar and rain gauge observations is presented in Chapter 3, followed by an assessment of pertinent Multi-Radar Multi-Sensor products in Chapter 4. Chapter 5 includes the conclusion and limitations as well as offers potential next steps.

CHAPTER 2: SYNOPTIC AND MESOSCALE ANALYSIS OF TROPICAL STORM IMELDA (2019)

Chapter 2 provides a synoptic and mesoscale analysis of Tropical Storm Imelda (2019). A variety of datasets are used to describe the evolution of the event and its impacts, including the excessive rainfall it produced and the embedded rotating features that were present in its remnants. This analysis provides a broad overview of the event and offers the motivation behind using this particular event in the analyses that examine rotation and rainfall rates in Chapters 3 and 4.

2.1 Introduction and Datasets

TS Imelda impacted the western Gulf Coast for several days in September 2019. Despite being a named TC for only a short time, the slow-moving system brought several days of flood-producing heavy rain and a couple of tornadoes to Southeast Texas and Southern Louisiana (Fig. 2.1). During the time leading up to its landfall and the day or so after, Imelda displayed characteristics similar to most weak TCs, such as spiraling rainbands with locally heavy precipitation and an isolated tornado risk in the right-front quadrant. However, as Imelda's structure deteriorated over land, the remnants of the system transformed into a quasi-stationary back-building convective line with embedded rotation that brought extreme rainfall rates in excess of 100 mm h^{-1} to some already saturated areas, which led to flooding. This interesting transformation provided motivation for the case study.

In this analysis, synoptic and mesoscale characteristics of the system, from its genesis to its dissipation, are assessed using radar, satellite, upper-air, and reanalysis data. First, the synoptic-scale evolution and large-scale dynamics are presented from the time that Imelda began developing to its dissipation (i.e., 9 September to 20 September). Then, moisture and thermodynamic properties that contributed to the heavy rainfall and embedded rotating features are examined on the mesoscale, with the primary focus being on the latter part of the period (i.e., beginning 18 September). The impacts of Imelda are detailed in the final section, where the motivation for its use in the other chapters of this thesis are detailed.

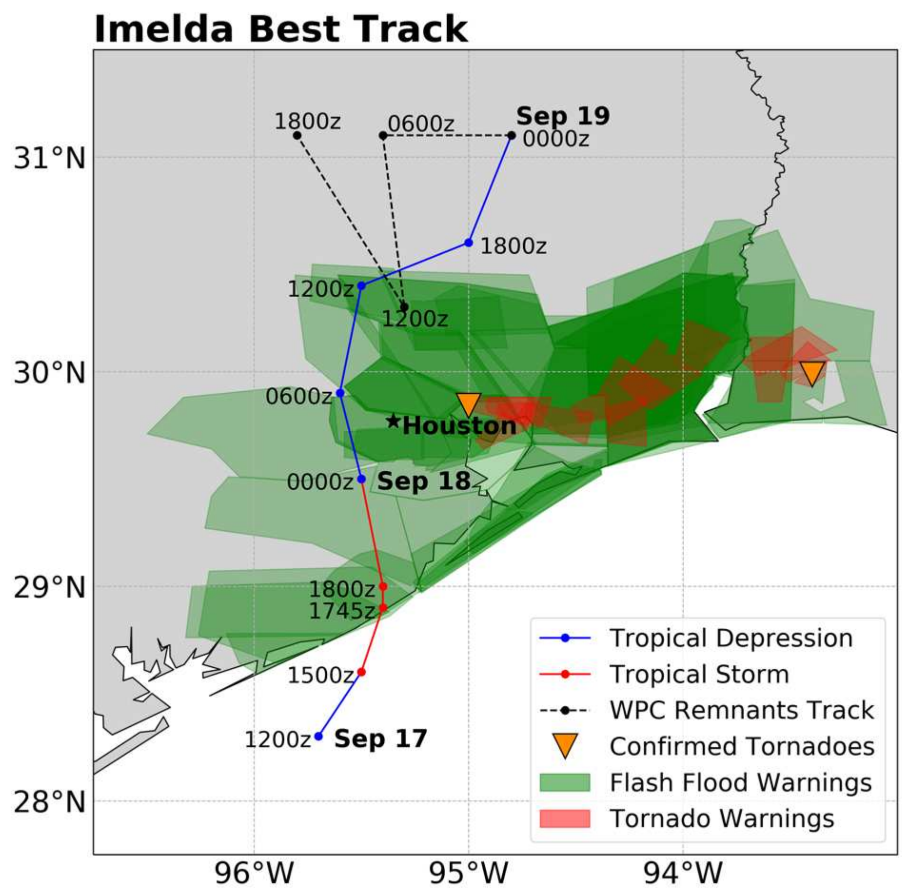

Figure 2.1: Tropical Storm Imelda track from the time at which it became a named tropical storm to its dissipation using National Hurricane Center HURDAT2 best track data (1800 UTC 23 August to 1200 UTC 2 September) (Landsea and Franklin 2013) and Weather Prediction Center surface analysis data (0000 UTC-1800 UTC 19 September). Dates and times are also annotated. Green polygons indicate Imelda-related storm-based flash flood warnings and red polygons indicate Imelda-related storm-based tornado warnings (archived warnings courtesy of Iowa Environmental Mesonet). Confirmed tornadoes are shown as orange triangular markers based on data from the National Centers for Environmental Information Storm Events Database.

For the analysis, the National Hurricane Center HURDAT2 database (Landsea and Franklin 2013) and Weather Prediction Center archived surface analysis (https://www.wpc.ncep.noaa.gov/html/sfc-zoom.php) were used to track the location of the center of circulation of the TC and the remnant low. The National Centers for Environmental Information (NCEI) Storm Events Database (https://www.ncdc.noaa.gov/stormevents/) was used for identifying confirmed tornadoes. Upper air sounding data from Lake Charles, Louisiana (KLCH) were collected from the University of Wyoming archives (http://weather.uwyo.edu/upperair/sounding.html). Rapid Refresh (RAP) 13 km reanalysis data (https://rapidrefresh.noaa.gov/; Benjamin et al. 2016) were also used for analyzing various meteorological fields. Software from MetPy (May et al. 2021) was used to help visualize 13 km RAP reanalysis data and upper air soundings in Python. 4 km enhanced infrared satellite images were collected from the Cooperative Institute for Research in the Atmosphere Regional and Mesoscale Meteorology Branch (CIRA RAMMB) tropical cyclone imagery archive (https://rammb-data.cira.colostate.edu/tc_realtime/). Radar data was collected from NCEI (https://www.ncei.noaa.gov/products/radar) and visualized in Python using the Py-ART library (Helmus and Collis 2016). Quantitative precipitation estimate (QPE) products come from the Multi-Radar Multi-Sensor (MRMS) system (Smith et al. 2016; Zhang et al. 2016). Flash flood guidance and storm-based warning data available from the Iowa Environmental Mesonet (https://mesonet.agron.iastate.edu/) were used to assess areas at high risk of flooding over time. Finally, WPC Excessive Rainfall Outlooks (EROs) (https://www.wpc.ncep.noaa.gov/archives/web_pages/ero/ero.shtml) and Storm Prediction Center Convective Outlooks (https://www.spc.noaa.gov/archive/) were used to emphasize the overlapping threat for heavy rainfall and tornadoes respectively.

2.2 Event Overview

2.2.1 Dynamics and System Evolution

13-km Rapid Refresh (RAP) analysis beginning 9 September 2017 shows an upper-level ridge centered over the northern high plains, with accompanying troughs to its east and west (Fig. 2.2a). Off the coast of the southeastern United States, a weak area of cyclonic rotation separate from the stronger flow to its north can be seen both in the 250 hPa wind fields and at 500 hPa (Fig. 2.3a) as an area of positive relative vorticity. As the upper-level trough amplified over the western U.S., the cyclonic

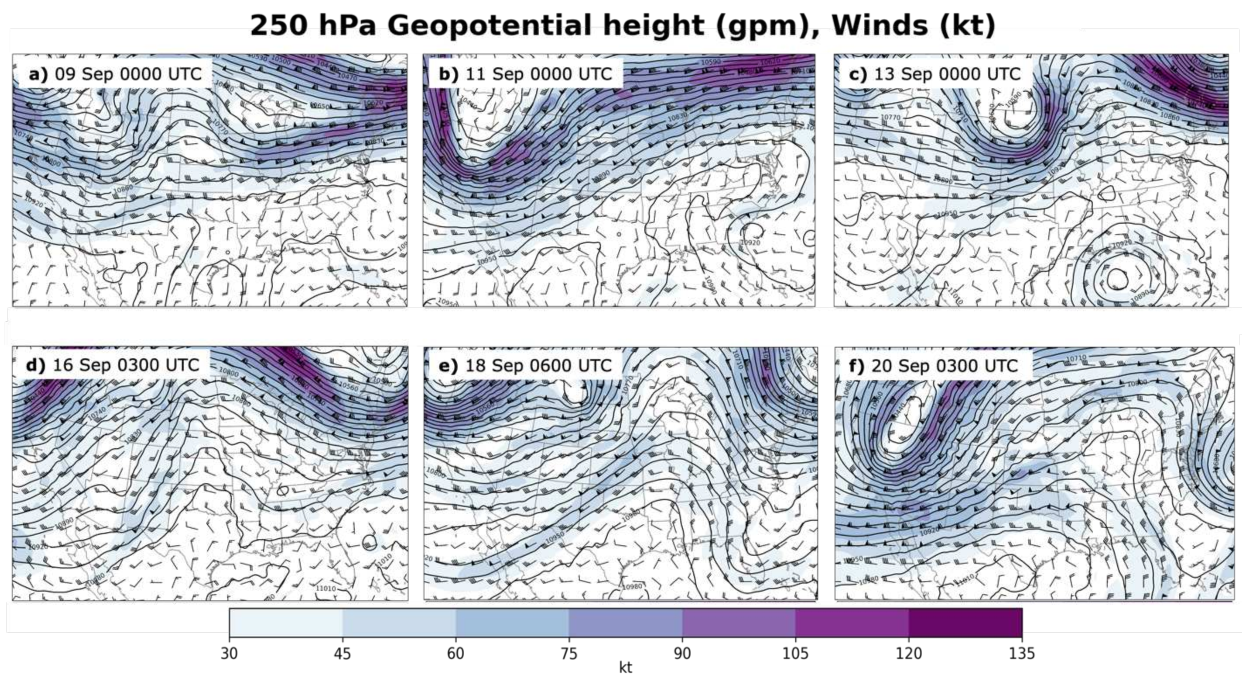

Figure 2.2: 13-km Rapid Refresh (RAP) analysis 250 hPa maps showing geopotential height (contour) and winds (barbs and filled contour for speeds ≥ 30 kt) at 9 September 0000 UTC (a), 11 September 0000 UTC (b), 13 September 0000 UTC (c), 16 September 0300 UTC (d), 16 September 0600 UTC (e), and 20 September 0300 UTC (f).

feature began to be absorbed by a weaker trough-like feature to the east, though by 0000 UTC 11 September, a new upper-level cyclonic circulation can be seen developing near the Georgia/South Carolina border (Fig. 2.2b). The upper-level low became cutoff over the next 36 hours and drifted southwestward across the northern Florida peninsula and into the eastern Gulf of Mexico (Fig. 2.2c).

A closed cyclonic circulation and associated positive relative vorticity can also be seen at 500 hPa, just west of the upper-level low (Fig. 2.3b), though this circulation was not yet evident in the lower levels.

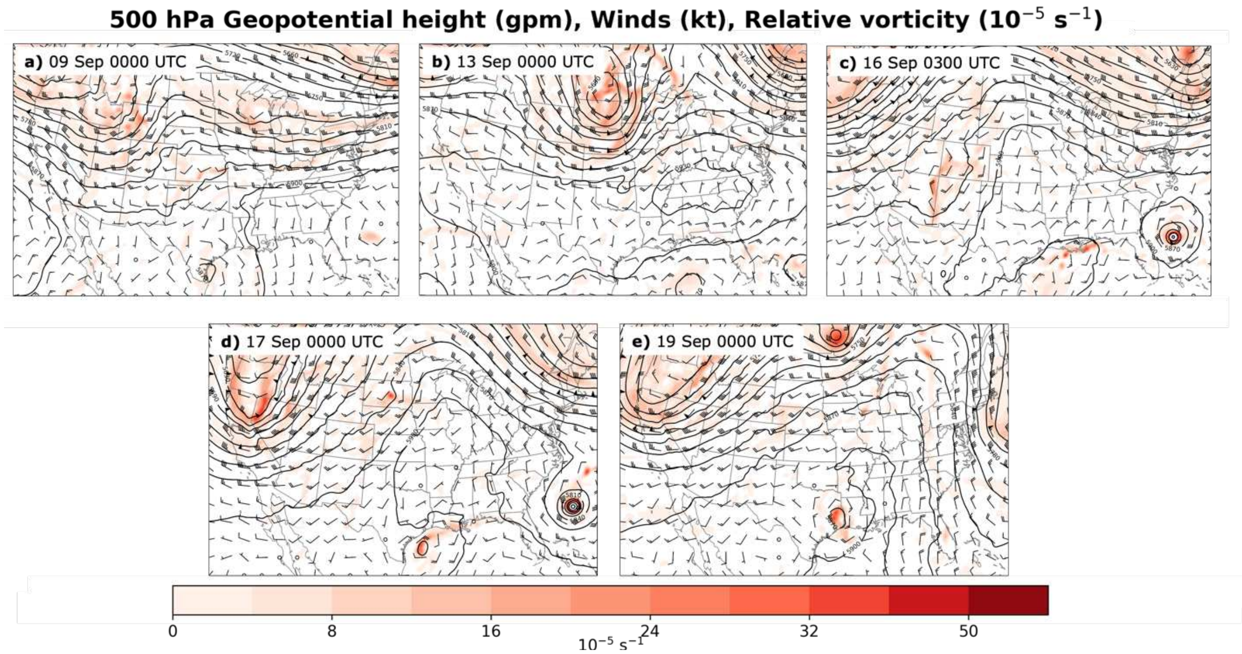

Figure 2.3: 13-km Rapid Refresh (RAP) analysis 500 hPa maps showing geopotential height (contour) and winds (barbs) and positive relative vorticity (shaded) at 9 September 0000 UTC (a), 13 September 0000 UTC (b), 16 September 0300 UTC (c), 17 September 0000 UTC (d), and 19 September 0000 UTC (e).

Embedded in this weak flow, the cyclonic feature continued drifting westward for the next several days, though the circulation in the mid and upper-levels weakened nearly to the point of unrecognition (Figs. 2.2d; 2.3c). Meanwhile, a much stronger TC, Hurricane Humberto, can be seen spinning off the southeast U.S. coast. Despite the weak circulation in the mid- to upper-levels, buoy data indicated the development of a weak surface low by 1200 UTC 16 September southeast of the Texas coast (Fig. 2.4a). Disorganized showers and storms associated with this developing low remained mostly offshore, other than a loosely-organized band of convection that moved onshore between 1900 UTC and 2100 UTC (Fig. 2.5a). By 0000 UTC 17 September, stacked cyclonic circulation became tighter and more well-defined as the surface low drifted slowly southwestward (Figs. 2.3d; 2.4b).

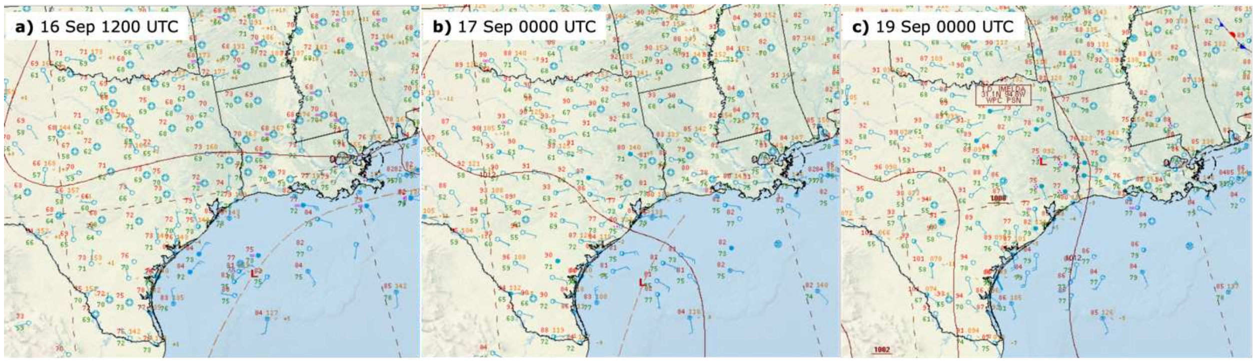

Figure 2.4: Surface analyses (courtesy of The Weather Prediction Center) for 16 September 1200 UTC (a), 17 September 0000 UTC (b), and 19 September 0000 UTC (c). Contours show surface sea level pressure.

After the offshore precipitation briefly weakened during the late hours of 16 September, the convection gradually reinvigorated throughout the early hours of 17 September as the surface low drifted slowly back northward. By 1200 UTC, the system organized further and was named Tropical Depression Eleven while TC-like rainbands began to spiral inland along the Texas coastline (Fig. 2.5b). Imelda became a named tropical storm around 1500 UTC, less than three hours before it made landfall around 1745 UTC (Fig. 2.5c) at its peak intensity (40 kt maximum sustained winds, 1003 hPa surface pressure) near Freeport, Texas (Fig. 2.1). Thunderstorm activity gradually became more widespread over inland areas during the latter part of 17 September, with the most intense convection focused close to the center of circulation (Figs. 2.5d; 2.6a).

Imelda weakened to a tropical depression by 0000 UTC 18 September. The system continued to slowly meander northward as a shortwave acted to tilt the ridge positively, which continued to leave the western Gulf Coast in a region with weak flow aloft (Fig. 2.2e). During the overnight hours of 18 September, most of the convective activity had become focused close to the center of circulation, with the most intense convection concentrated on the south side of the system along the southeast Texas coast (Fig. 2.6b). By 0800 UTC, areal rainfall coverage gradually increased, particularly southeast of

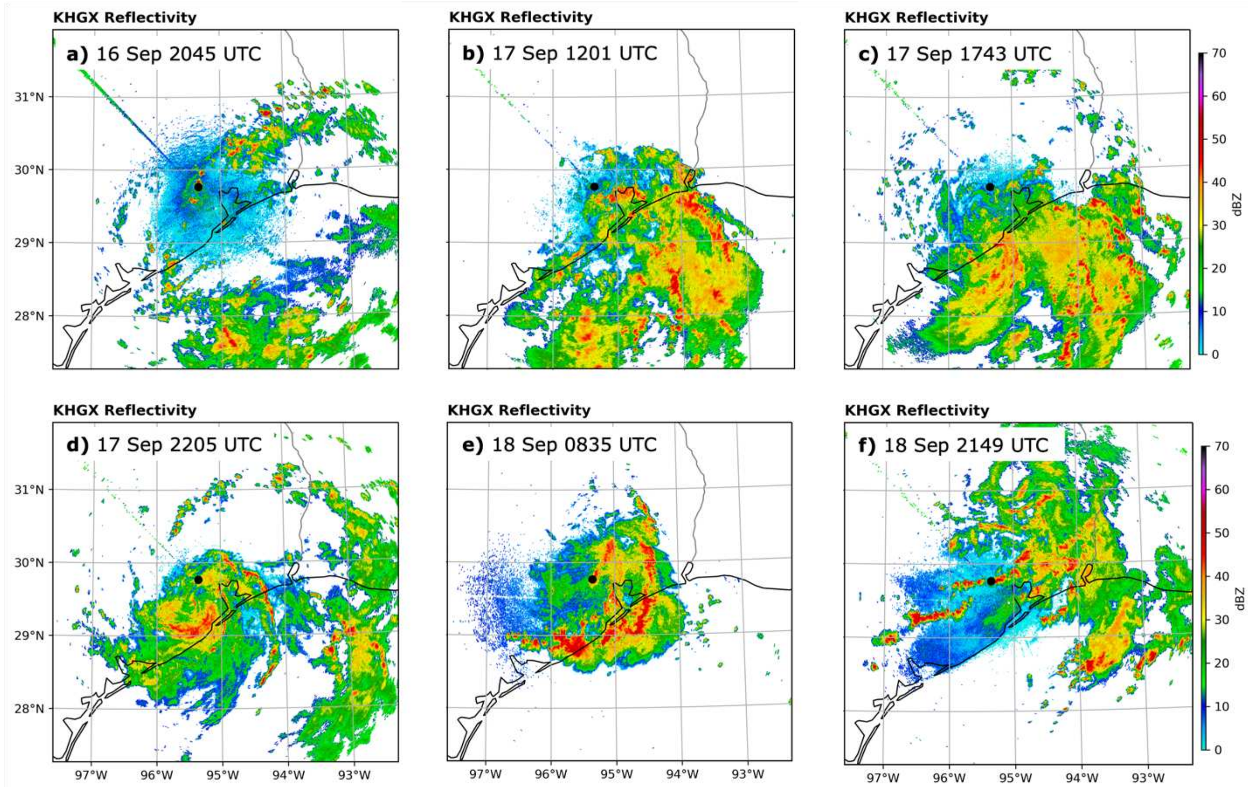

Figure: 2.5 Radar reflectivity from the Houston-Galveston radar in League City, Texas (KHGX) at 2045 UTC 16 September (a), 1201 UTC 17 September (b), 1743 UTC 17 September (c), 2205 UTC 17 September (d), 0835 UTC 18 September (e), and 2149 UTC 18 September (f). The black dot indicates the approximate location of downtown Houston, Texas.

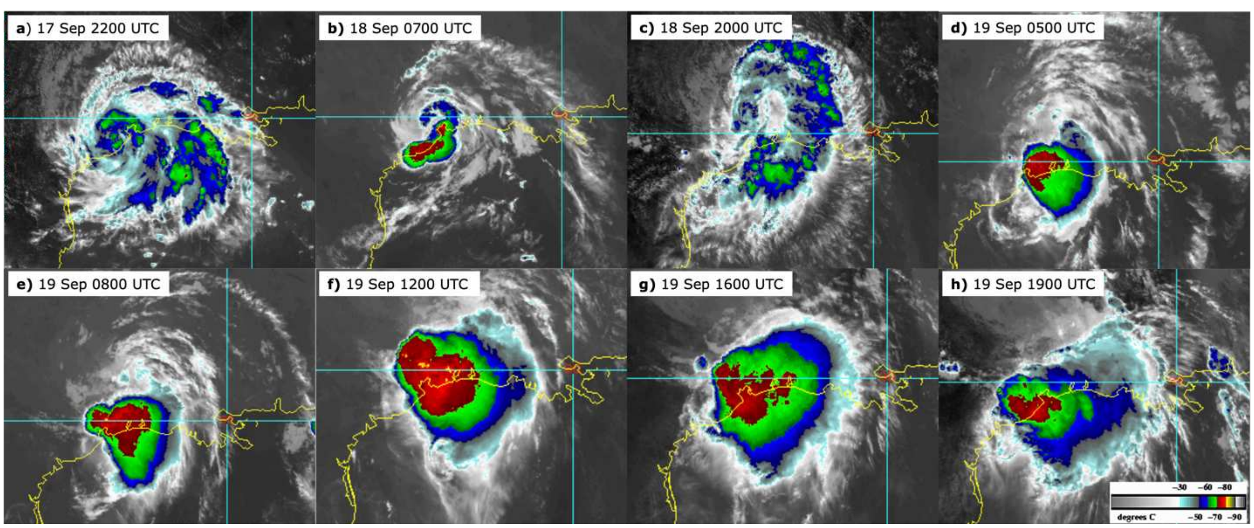

Figure 2.6: 4 km enhanced infrared images of Imelda (courtesy of CIRA RAMMB; Mueller et al. 2006). Images are shown for 17 September at 2200 UTC (a); 18 September at 0700 UTC (b) and 2000 UTC (c); and 19 September at 0500 UTC (d), 0800 UTC (e), 1200 UTC (f), 1600 UTC (g), and 1900 UTC (h). The colorbar in the bottom right of (h) represents cloud top temperatures for all images.

the center of circulation (Fig. 2.5e). The convection near the coast (southeast of Houston) was backbuilding for a few hours during this time, which led to saturated surfaces in the area as indicated by decreased flash flood guidance (Fig. 2.7a). Areal coverage of precipitation increased during the late morning and early afternoon, with the bulk of the inland convection shifting northeastward (Fig. 2.6c). Within the system, a few convective bands with embedded supercells developed (Fig. 2.5f), which prompted several tornado warnings.

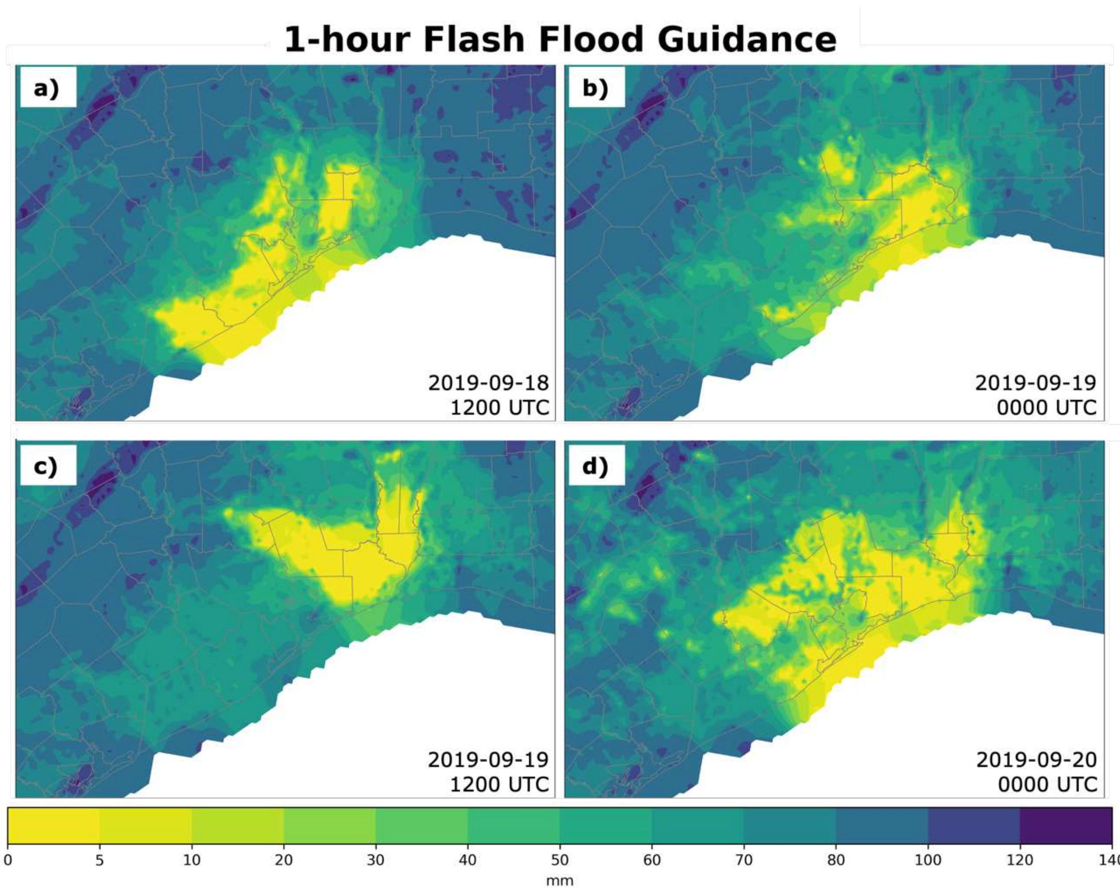

Figure 2.7: One-hour flash flood guidance for 1200 UTC 18 September (a), 0000 UTC 19 September (b), 1200 UTC 19 September (c), and 0000 UTC 20 September (d). The one-hour flash flood guidance product incorporates antecedent stream flow and soil moisture conditions to describe the approximate amount of rainfall that must fall over a particular area within one hour in order for flash flooding to occur in small streams.

By 0000 UTC 19 September, the system had lost much of its TC-like structure, though the most intense rain had yet to fall. According to estimates from the Multi-Radar Multi-Sensor (MRMS) system, widespread totals in excess of a few hundred millimeters had already occurred across the western Gulf Coast region over the previous several days (Fig. 2.8a), which led to saturated soils in many areas, as evidenced by flash flood guidance (Fig. 2.7b). In the early part of 19 September, a region of cooling cloud tops stretching from the coastal Texas/Louisiana border to the eastern suburbs of Houston (Fig. 2.6d) began to develop south of the center of Imelda's surface circulation (Fig. 2.4c), which remained fairly well stacked with the cyclonic circulation in the mid-levels (Fig. 2.3e). Fig. 2.3e shows that there were still high values of positive relative vorticity in the mid-levels (with the maximum being just north of the developing precipitation complex). Northeasterly winds on the western side of the mid-level circulation likely helped to advect this area of positive vorticity southwestward towards the developing system, creating a localized area of positive vorticity advection.

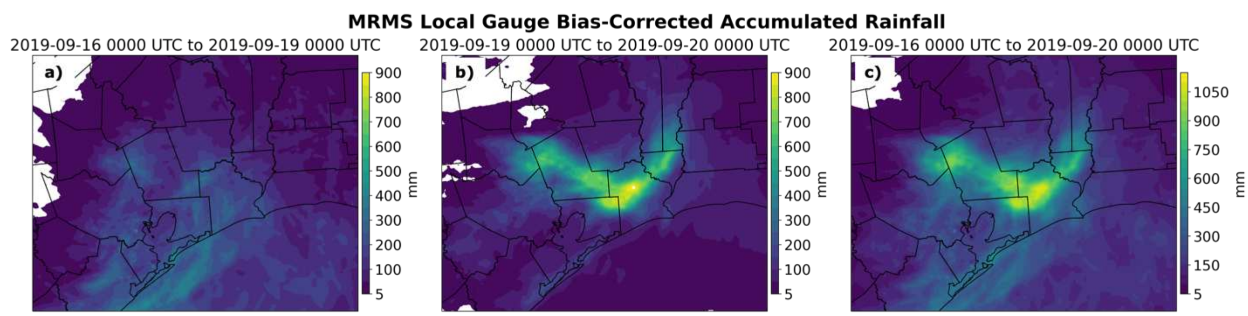

Fig. 2.8: Multi-Radar Multi-Sensor (MRMS) local gauge bias-corrected quantitative precipitation estimate (QPE) for 0000 UTC 16 September to 0000 UTC 19 September (a), 0000 UTC 19 September to 0000 UTC 20 September (b), and 0000 UTC 16 September 0000 UTC 20 September (c).

The original precipitating structure began as a north-south oriented bowing convective line just west of the Texas/Louisiana border (Fig. 2.9a). By 0330 UTC, small convective cells began to develop just west of the main convective line and propagate eastward in a linear fashion as new cells continued to form upstream of the cell propagation (Fig. 2.9b). This WNW-ESE oriented convective line consisting of merging and backbuilding cells intensified over the next few hours, as evidenced by

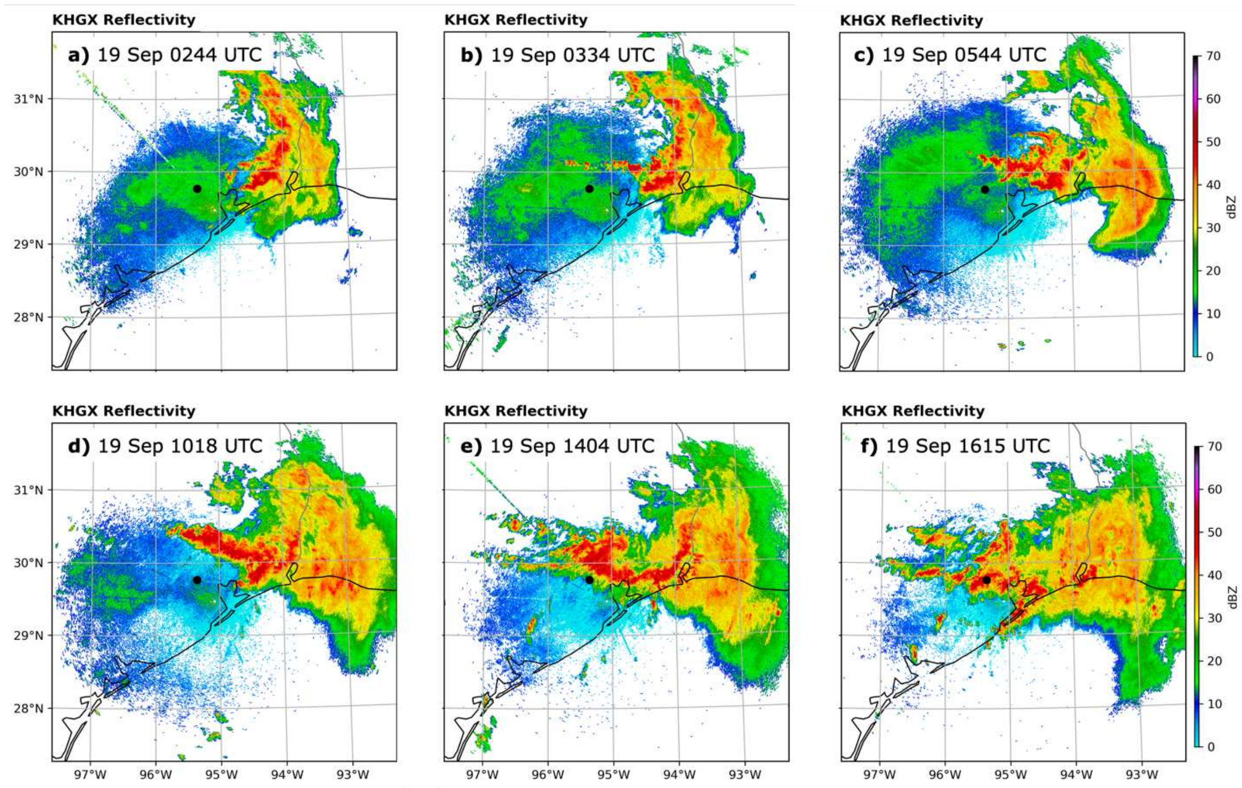

Figure 2.9: As in Fig. 2.5, but for 19 September at 0244 UTC (a), 0334 UTC (b), 0544 UTC (c), 1018 UTC (d), 1404 UTC (e), and 1615 UTC (f).

cooling cloud tops (Fig. 2.6d) and increasing radar reflectivity (both in terms of magnitude and extent) (Fig. 2.9c). Meanwhile, the north-south bowing feature that had been the dominant feature in the earlier part of the period decayed somewhat, though the reflectivity values imply that heavy rainfall was still persisting in that area. This “t-shaped” pattern with a backbuilding east-west oriented line with a north-south oriented band of heavier convection is very similar to the structure found with Typhoon Morakot (2009) over Taiwan by Wang et al. (2015) (their Figs. 3b; 4), though the north-south oriented convective line in that event was shown to be terrain-induced, which was not the case here. The shield of cooling cloud tops would continue to grow in extent for at least another 6 hours (Figs. 2.6e-f) as the quasi-stationary backbuilding convective line continued to intensify (Fig. 2.9d). Over this period, several persistent embedded rotating features could be seen within the convective line (see Figs. 4.10; 4.11 in Chapter 4). The nearly-stationary motion of the intense nocturnal MCS decreased flash flood guidance to essentially zero in the local area by 1200 UTC (Fig. 2.7c).

Radar imagery around 1400 UTC shows that the convective line had begun to bow southward, as well as progress slightly towards the southwest over the past couple hours (Fig. 2.9e). This trend would continue over the next several hours, as the system would begin to affect the greater Houston area. During this time, the area of cold cloud tops gradually decreased in extent (Fig. 2.6g) and the quasi-linear MCS started to fracture (Fig. 2.9f). As the most intense convection continued moving towards the southwest, this disorganization and weakening trend continued (Fig. 2.6h). The system devolved into scattered thunderstorms by 2200 UTC. However, the lingering effects of the extreme rainfall from earlier in the day persisted, as evidenced by the flash flood guidance at 0000 UTC 20 September (Fig. 2.7d). Other than some light stratiform precipitation near the southern Texas/Louisiana border throughout 20 September, Imelda's rainfall had largely concluded in the study area. However, the system did bring some heavy rainfall to areas further north such as southeast Oklahoma (Latto and Berg 2020), which was likely supported by upper-level divergence from the deepening trough over the western CONUS (Fig. 2.2f) before it finally dissipated.

Over the 24-hour period ending on 0000 UTC 20 September, areas affected by the back-building convective line experienced at least as much rainfall as they had over the previous three days combined, if not more (cf. Figs. 2.8a-b). As a result, some locations saw storm total rainfall estimates in excess of 1000 mm over a period of just 4 days (Fig. 2.8c). The next section investigates the time period when the most extreme rainfall fell more closely by examining the moisture, thermodynamics and mesoscale dynamics that were in place at the time.

2.2.2 Mesoscale Dynamics, Moisture, and Thermodynamics

Soundings from KLCH (located in southwestern Louisiana) show low-level moisture below approximately 500 hPa with drier air aloft before Imelda's landfall (Fig. 2.10a). Soon after the LTC made landfall, this dry air began to be eroded away as the low to mid-levels continued to become more

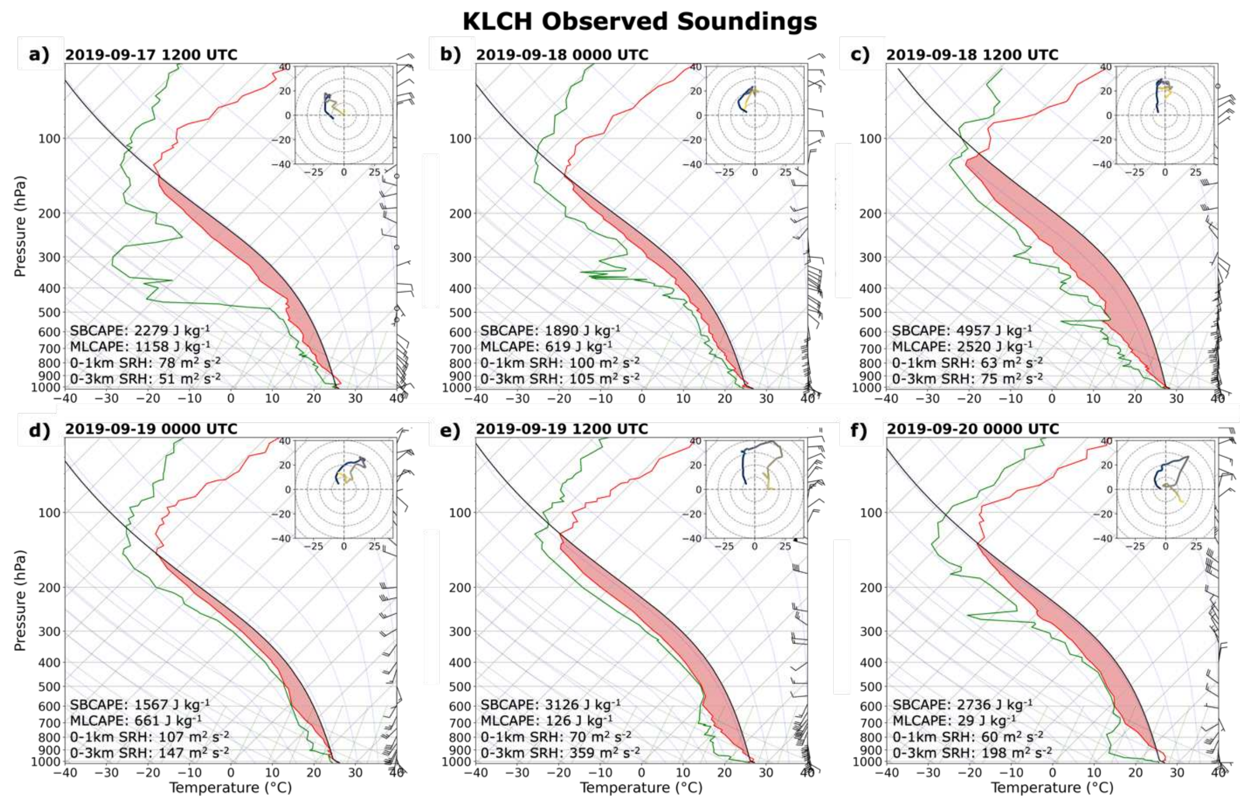

Figure 2.10: Observed upper-air soundings and hodographs from Lake Charles, LA (KLCH) for 1200 UTC 17 September (a), 0000 UTC 18 September (b), 1200 UTC 18 September (c), 0000 UTC 19 September (d), 1200 UTC 19 September (e), 0000 UTC 20 September (f). Parcel trajectories (black line) shown are for surface-based parcels, surface-based convective available potential energy (SBCAPE) shaded is in red, and temperature and dewpoint profiles are shown as red and green lines, respectively. SBCAPE, mixed-layer CAPE (MLCAPE), 0-1km storm-relative helicity (SRH), and 0-3km SRH are annotated. Wind barbs and hodographs are shown in units of knots. Sounding data is courtesy of the University of Wyoming sounding archive and is plotted using software from MetPy (May et al. 2021).

saturated (Fig. 2.10b). The atmosphere remained relatively unstable during this period, with surface-based convective available potential energy (SBCAPE), showing values in excess of 1800 J kg^{-1}. Low-level shear values remained low in terms of tornado potential (as evidenced by the 0-1 km and 0-3 km storm relative helicity, or SRH, values), which likely limited tornadogenesis within Imelda's rainbands soon after the system made landfall. The soundings in Fig. 2.10a; b also show a SBCAPE profile that is "skinny" as opposed to "fat", and the warm cloud depth (based on the 0°C isotherm) extends vertically up to at least 600 hPa—both features that tend to be favorable for heavy precipitation due to the slower, deeper ascent that promotes warm rain processes. These features were accompanied by plenty of moisture availability, according to the column-integrated precipitable water (PWAT) values (Fig. 2.11a).

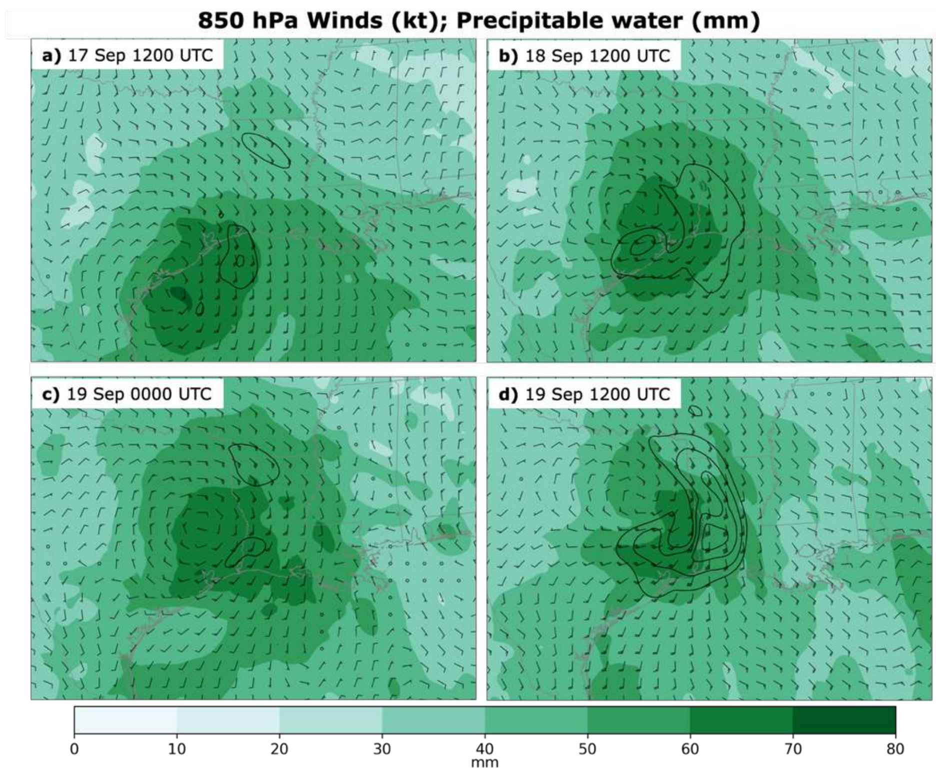

Figure 2.11: 13-km Rapid Refresh (RAP) analysis 850 hPa winds (barbs; contoured every 5 kt starting at 25 kt) and column-integrated precipitable water (fill, mm) at 1200 UTC 17 September (a), 1200 UTC 18 September (b), 0000 UTC 19 September (c), and 1200 UTC 19 September (d).

As Imelda continued its slow northward progression after landfall, instability, moisture availability, and warm rain processes continued to be favorable for heavy rainfall throughout 18 September (Figs. 2.10c-d; 2.11b). Despite the weak low-level shear values, SBCAPE and mixed-layer (MLCAPE) remained very high, and the lifted condensation level (LCL) heights were very close to the surface. These ingredients tend to be favorable for tornadogenesis, and even though shear values were very low, several tornado warnings were issued throughout the day, with a confirmed tornado occurring around 2200 UTC in an east Houston suburb (Fig. 2.1).

As heavy rainfall continued to track near the southeastern Texas and southwestern Louisiana border (Fig. 2.5f) during the afternoon and evening hours of 18 September, a north-south oriented surface temperature gradient can be seen developing (Figs. 2.12a-b) as a result of differential heating occurring between the precipitating and cloud-free areas. Meanwhile, according to the 10 m winds, Imelda's surface circulation can be seen slowly degenerating as the evening progressed (cf. Figs. 2.12a-b).

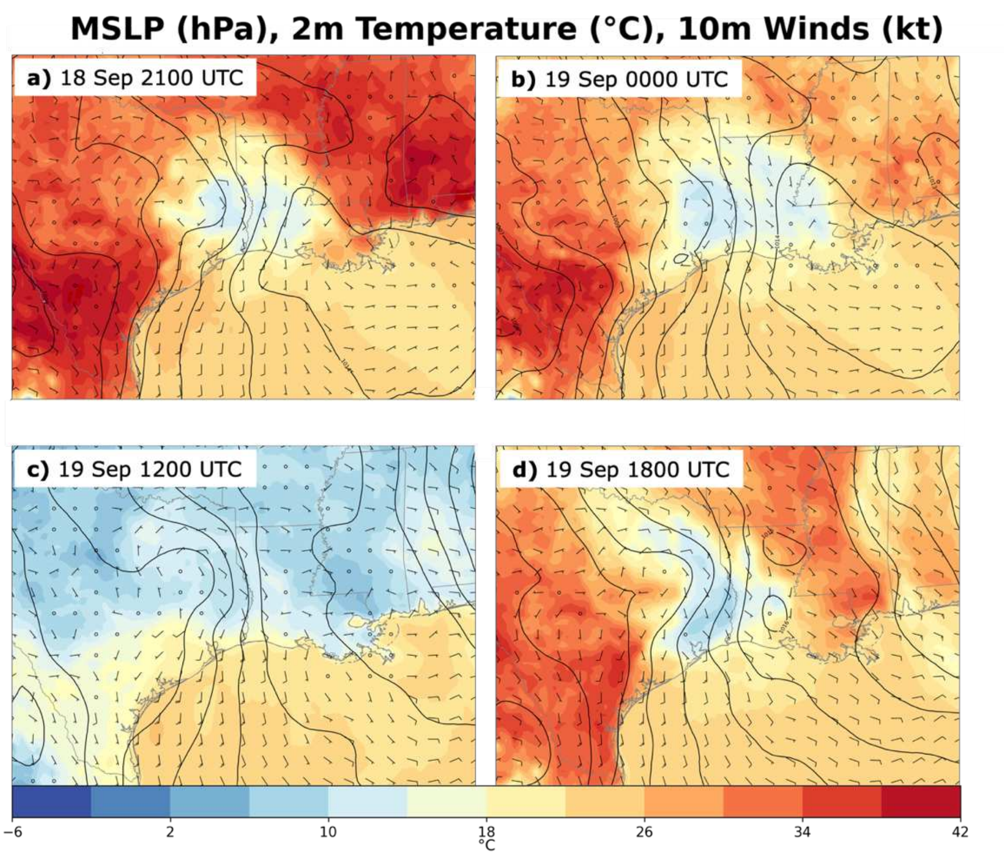

Figure 2.12: 13-km Rapid Refresh (RAP) analysis surface maps showing mean sea level pressure (MSLP) (contoured every 1 hPa), 2 m temperature (fill), and 10 m winds (barbs) for 2100 UTC 18 September (a), 0000 UTC 19 September (b), 1200 UTC 19 September (c), and 1800 UTC 19 September (d).

Beginning around 0000 UTC 19 September, which marked the approximate start of the MCS development, many ingredients began to come together to support the t-shaped convection, which featured a backbuilding line and weak bow echo, that would emerge over the next several hours. Though instability had relaxed some compared to earlier in the day according to the KLCH sounding (Fig. 2.10d), there was persistent equivalent potential temperature (θ_e) advection over a localized area near the southern Texas/Louisiana border, suggesting increasing potential instability (from SPC mesoanalysis archive, not shown). Additionally, 0-1 km and 0-3 km SRH began to increase, and a veering wind profile (often associated with warm air advection) began to become apparent (Fig. 2.10d). In the low-levels, mean 925 hPa to 700 hPa winds show convergence over far southeast Texas, with southwesterly flow offshore and northwesterly winds driven by the remnant low-level circulation that had shifted northward (Fig. 2.13a). The converging low-level wind field impinged on the warm side of the north-south oriented temperature gradient (Fig. 2.12b) at a nearly perpendicular angle, which promoted forcing for ascent and likely helped trigger the initial convection that developed west of and perpendicular to the existing convective complex (Fig. 2.9b). This wind pattern relative to the preexisting convection and precipitation-driven temperature gradient resembles that of "bow and arrow" convection that has been found in MCSs (Keene and Schumacher 2013). A very sharp SBCAPE gradient can also be seen developing along the coastal counties, with areas near the coast showing very high stability (> 3000 J kg^{-1}) and areas further inland having significantly less (< 500 J kg^{-1}). The low-level winds can be seen converging on the area where the SBCAPE gradient was the sharpest (Fig. 2.13a). Meanwhile, moisture availability continued to be plentiful, with maximum PWAT values remaining very similar to what they had been over the past few days (Fig. 2.11c).

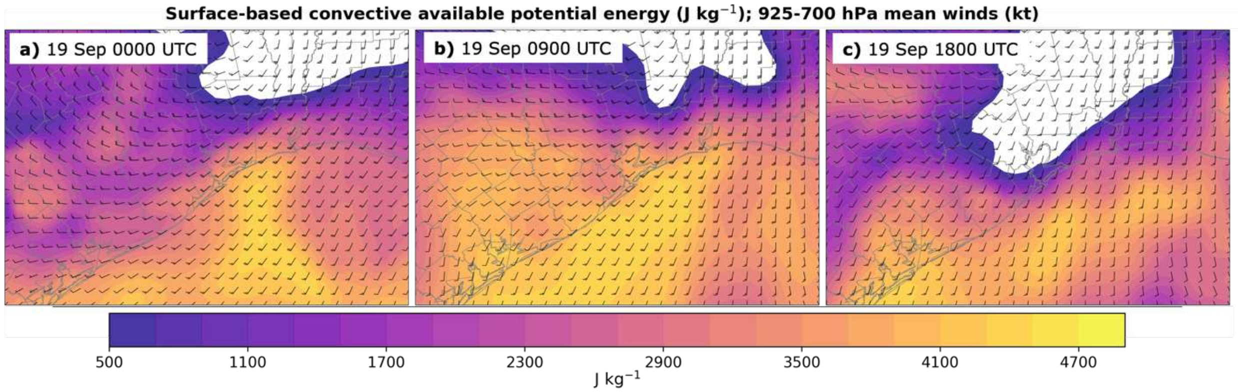

Figure 2.13: 13-km Rapid Refresh (RAP) analysis showing surface-based convective available potential energy (SBCAPE) (shade) and 925 hPa mean winds on 19 September at 0000 UTC (a), 0900 UTC (b), and 1800 UTC (c).

Low-level wind convergence continued as 19 September progressed, with the northwesterly winds that were feeding into the zone of convergence becoming more westerly (Fig. 2.13b). Soundings from KLCH also suggest that low-level winds feeding in from the southwest (or south, given the location of the sounding site) became slightly stronger as nocturnal cooling set in, suggesting evidence of a LLJ (cf. Figs. 2.10d-e). Despite nocturnal cooling, instability continued to increase, particularly west of the convective line (2.13b). Storm-relative helicity also continued to increase (Fig. 2.14a), with the highest values being co-located near the area of maximized low-level convergence and the sharpest SBCAPE gradient. Comparing Figs. 2.13b and 2.9d, the orientation of the convective line appears to set up parallel to the SBCAPE gradient, and the low-level winds seem to intersect the gradient at an approximately 45° angle. 0-3 km SRH increased to values in excess of 300 m^2s^{-2} at their peak around 1200 UTC to 1300 UTC (Fig. 2.14b), which is sufficient to support rotating updrafts. Coincidentally, this is also the time when the southerly LLJ was the strongest, as evidenced by the localized corridor of enhanced southerly flow at 850 hPa over western Louisiana (Fig. 2.11d). The 850 hPa westerly flow (resulting from the converging wind field in the low-levels) to the west of the LLJ were also near its peak at this time as the winds intersected the southerly LLJ at a nearly 90° angle. Meanwhile, sounding data from KLCH reflected the increasing SBCAPE that had also occurred overnight, with 1200 UTC values nearly doubling from the 0000 UTC sounding (Fig. 2.10e). The 1200 UTC hodograph also indicates very strong, deep shear—demonstrating a "hairpin" shape that has been previously shown to support backbuilding convection due to the strong reversal in winds with height (Schumacher and Johnson 2009). PWAT values continued to remain high as well (Fig. 2.11d). At the surface, nocturnal cooling made the surface temperature gradient less apparent (Fig. 2.12c).

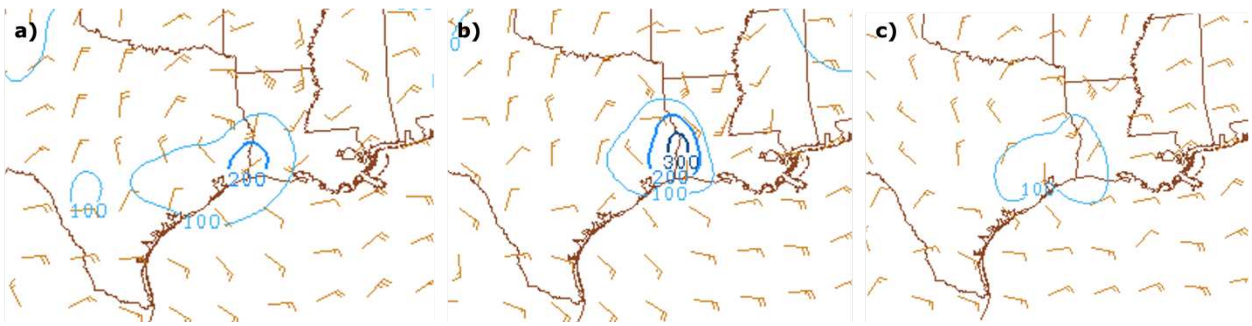

Figure 2.14: 0-3 km storm relative helicity (SRH) ($m^2\ s^{-2}$) for 19 September at 0700 UTC (a), 1300 UTC (b), and 2000 UTC (c). Courtesy of the Storm Prediction Center Mesoanalysis Archive.

As diurnal heating began, conditions became less favorable for the backbuilding convective line. As the MCS progressed southward by approximately 1400 UTC (Fig. 2.9e), the low-level cyclonic circulation began to shift north. While the low-level convergence remained, the area of maximized convergence also shifted north as the relatively high inland SBCAPE values had eroded due to the hours of intense convection that had persisted over the same area (Fig. 2.13c). These two changes meant that the convergent low-level winds were no longer co-located with an area of elevated instability. Thus, while there was still plenty of moisture (Fig. 2.11d), a re-developing temperature gradient driven by the ongoing convection and daytime heating (Fig. 2.12d), and ongoing convergence in the low-level wind field (Fig. 2.13c)—the latter two of which could serve as a lifting mechanism—the lack of instability due to the hours of convection that had worked-over the atmosphere was the limiting factor in perpetuating the MCS. Furthermore, weakening 0-3 km SRH also largely hindered the ability for embedded rotating updrafts to form within the system (Fig. 2.14c). Low-level shear and SBCAPE remained somewhat more favorable further east (e.g., southern Louisiana) even into the evening hours according to the KLCH soundings (Fig. 2.10f). These ingredients likely helped to make the environment in that region more favorable for tornadic development compared to areas further west—and there was a brief EF-0 tornado around 1600 UTC south of Lake Charles, LA (Fig. 2.1).

To summarize, several ingredients were in place that promoted an extreme rainfall event to take place in southeast Texas, the worst of which occurred on 19 September 2019. First, there was plenty of moisture availability in place with Tropical Storm Imelda's remnants, and while the system had been inland for several days, the column-integrated moisture had not changed much. There was plenty of surface-based instability (though mixed-layer instability was more limited) and observed radiosonde profiles showed persistent, deep warm cloud depths and skinny SBCAPE profiles—both of which provided favorable conditions for warm rain processes. Ongoing precipitation created a localized north-south oriented temperature gradient. Low-level winds from the northwest and southwest impinged on the warm side of this temperature gradient to create a localized zone of enhanced westerly winds, serving as a source of forcing for ascent. A southerly LLJ also developed to the east of the converging wind field, which enhanced low-level shear and moisture convergence on the eastern side of the system. Moderate SBCAPE values suggested favorable instability, and relatively high 0-3 km SRH values, indicating the potential for rotating updrafts (as was evident in several locations within the convective system based on storm-relative velocity data). Additionally, referring back to the previous section, mid-level cyclonic rotation and associated positive relative vorticity from the remnant LTC was located just north of the convective system (Fig. 2.3e). This feature likely provided a somewhat larger scale source of positive vorticity advection into the region where the backbuilding line became organized. As the developing cells moved westward with the ambient winds, persistent forcing from the converging winds along the edge of the temperature gradient provided upward forcing to allow convection to continue developing on the back side of the system. Storm-scale cold pools from the downwind convection likely locally enhanced this lift even further. The system began to degrade when the instability and forcing were no longer co-located.

Features of Imelda on 19 September were consistent with findings from previous literature on backbuilding MCSs. The presence of a southerly LLJ impinging on a decaying mid-level cyclonic circulation (which was the remnants of Imelda in this case) accompanied by high-θ_e air to the south and west (that was also positively advecting into the region where the MCS developed) strongly resembled the environmental setup described in Schumacher and Johnson (2009)'s study on quasi-stationary/backbuilding convection (Fig. 2.15a). One notable difference that was found with Imelda was the zone of enhanced low-level westerlies resulting from converging northwesterly and southwesterly winds, which was a feature that their results did not show. However, this feature was present in Keene and Schumacher (2013)'s study on "bow and arrow" convection (Fig. 2.15b). Additional features from their study were also found with Imelda's remnants, particularly in the earlier hours of 19 September. These similarities include 1) a bowing MCS (the "bow") that preceded the upstream development of the "arrow", 2) a surface cold pool, created by the cool outflow from the "bow", 3) enhanced westerly winds that impinged on the warm side of the cold pool and provided forcing for ascent, and 4) the subsequent development of the "arrow"—a linear convective feature that developed along the cold outflow approximately parallel to the “bow”. However, there were slight differences in the role of the LLJ between their study and this one. Specifically, the LLJ seemed to

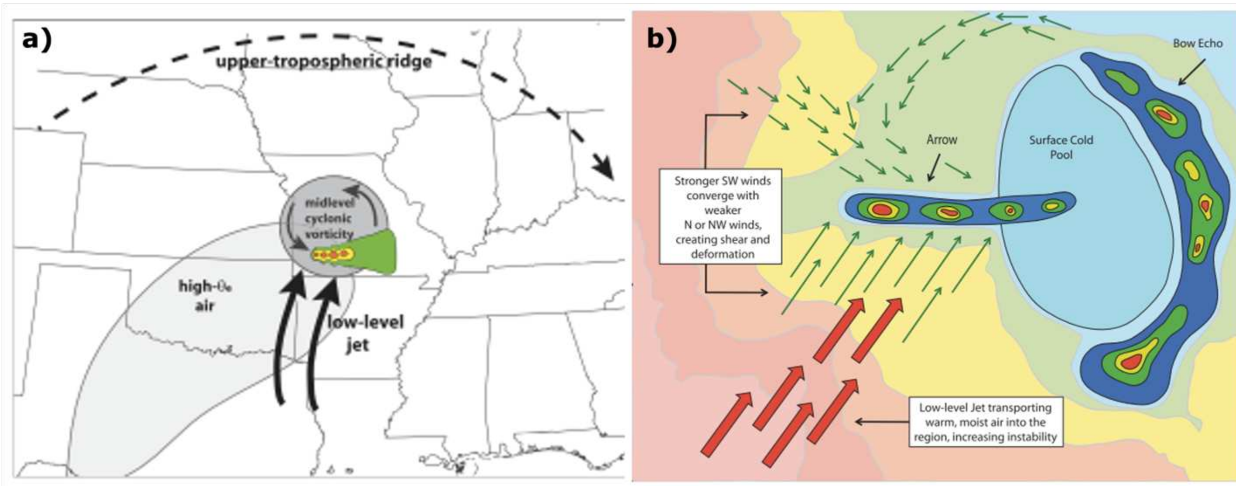

Figure 2.15: The schematic on the left shows the interaction of a midlevel cyclonic vortex and low-level jet to produce a backbuilding mesoscale convective system (MCS), from Fig. 13 in Schumacher and Johnson (2009) (a). The low-level jet (LLJ) is represented by thick black arrows, the flow around a upper-level ridge is shown as a dashed black arrow, and the thinner black arrows represent the mid-level cyclonic circulation and associated vorticity (shaded in dark gray). The region of high-θ_e lower tropospheric air is shaded light gray. The schematic on the right shows the development of “bow and arrow” convection, from Fig. 25 in Keene and Schumacher (2013) (b). Green arrows represent wind speed and direction at all pressure levels, the red arrows symbolize the LLJ, and the shaded contours in the background of the figure represent temperature (with warmest colors in red and coolest colors in blue). The bow echo, linear “arrow”, and cold pool are all labeled.

supply the southwesterly flow into the converging low-level wind field in Keene and Schumacher (2013), whereas this feature was not evident in Imelda—rather, the LLJ was more southerly and co-located with the “bow” and seemed to be predominately supporting ongoing convection along the eastern side of the system. A third study that aspects of Imelda resembled on 19 September were some of the findings by Wang et al. (2015). Their study showed the development of an east-west oriented backbuilding MCS embedded within the rainbands on the south side of a typhoon and formed perpendicular to a terrain-induced north-south oriented convective line, creating a “t-shaped” zone of convection. Their study showed that converging northwesterly and southwesterly winds were co-located with a westerly LLJ, which contributed to the development of the quasi-stationary backbuilding convective line by providing strong shear. The radar imagery shown in their study (their Fig. 3b, not shown) strongly resembled the t-shaped reflectivity patterns seen during some periods in Imelda (e.g., Fig. 2.9d). While it is worth considering similarities between their study and Imelda (e.g., the interaction with the low-level jet, the orientation of the convection), there are some notable differences—particularly with respect to terrain effects, which played a significant role in their study but were irrelevant in Imelda. Therefore, it appears most likely that the quasi-stationary convective complex associated with Imelda's remnants developed as a result of a combination of the environmental characteristics described by Schumacher and Johnson (2009) and Keene and Schumacher (2013).

2.3 Impacts and Motivation for Use in this Study

The intense flash flood-producing rainfall was the primary driver for the damage that resulted from Imelda in southeast Texas. Based on the maximum rainfall that fell with Imelda (approximately 1125 mm), the LTC became the fifth wettest on record[2] to impact CONUS (Weather Prediction Center), surpassing rain totals from other notorious heavy rain-producing systems such as Tropical Storm Allison (2001) and Hurricane Florence (2018). While Imelda's rain totals were lower and covered less area compared to Hurricane Harvey in 2017 (Fig. 2.16), many of the same areas were impacted. The flood-producing rainfall associated with Tropical Storm Imelda ultimately led to 5 deaths, several high water rescues, and damage to thousands of homes (Latto and Berg 2020). In addition to the flooding caused by Imelda, there was a marginal tornado threat that verified: some

[2] Based on maximum accumulated rainfall that was recorded.

additional damage was caused by two brief tornadoes (one rated EF-0 and on rated EF-1). Though the tornado-related impacts were far less extensive relative to the flooding (NOAA National Centers for Environmental Information 2021a), the tornado threat was taking place in the same locations that were also at risk of flash flooding (Fig. 2.1). Economically, Tropical Storm Imelda was classified as a billion-dollar disaster, with the damage estimates exceeding $5 billion dollars (NOAA National Centers for Environmental Information 2021b).

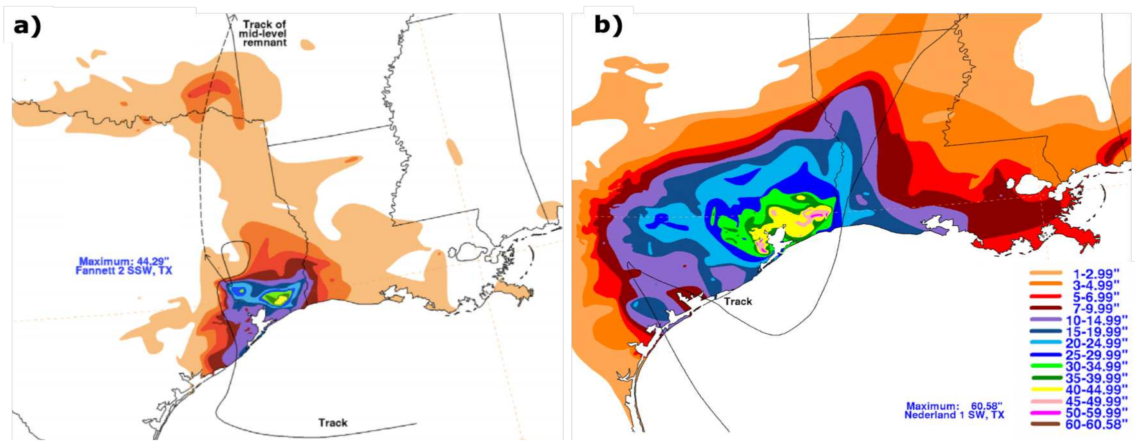

Figure 2.16: Storm total rainfall (in inches) for Tropical Storm Imelda (a) and Hurricane Harvey (2017) (b), courtesy of the Weather Prediction Center.

This overview of Tropical Storm Imelda on the synoptic and mesoscales provides motivation to investigate the LTC on even smaller scales—specifically, one that focuses on the relationship between heavy rainfall and embedded rotation. First, the extreme rain rates were accompanied by multiple persistent embedded mesovorticies for many hours, which provides a relatively long period of time to examine their relationship in the local observations. Second, from a forecast operations and human impacts standpoint, there existed a co-located, concurrent threat for tornadoes and flash flooding (Figs. 2.17; 2.18). According to the storm-based warnings (Fig. 2.1), the dual threat did materialize, with 12 spatiotemporal TORFF warning overlaps occurring. This point is relevant because it indicates that there was a legitimate risk that overlapping hazards could emerge as a consequence of these two meteorological processes, and it highlights its relevancy to the overarching goal of better understanding the interconnectedness of the two phenomena. Lastly, the area was well-covered by a variety of relevant observational platforms (e.g., rain gauges, radar), which makes it a good location to examine embedded rotation and rainfall on the storm- to mesoscales. It is these reasons that Tropical Storm Imelda will be used in Chapters 3 and 4 to study the co-location of extreme rainfall rates and embedded rotation through observations.

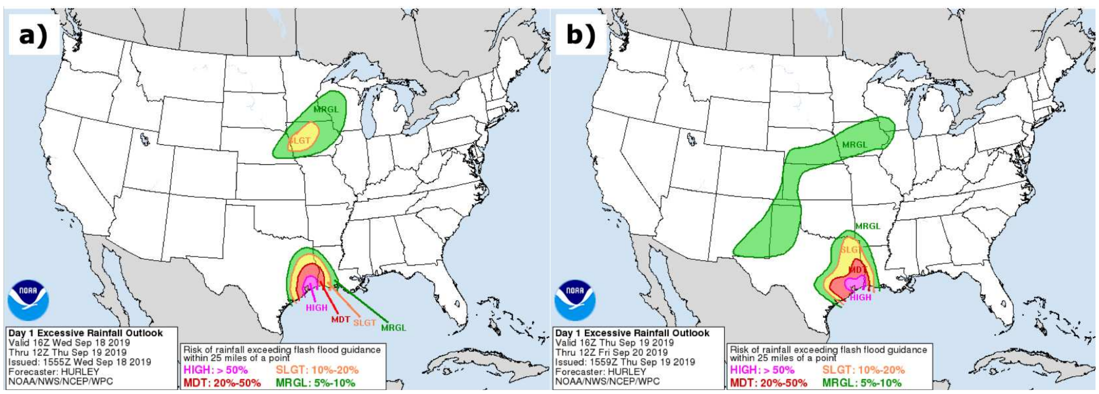

Figure 2.17: Day 1 Excessive Rainfall Outlook (ERO) products from the Weather Prediction Center (WPC) for 1600 UTC 18 September to 1200 UTC 19 September 2019 (a) and 1600 UTC 19 September to 1200 UTC 20 September 2019 (b).

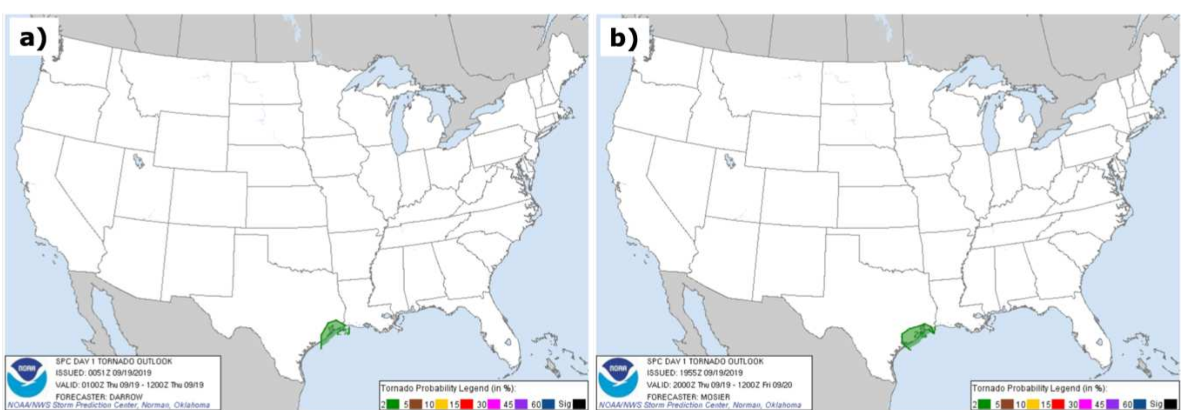

Figure 2.18: Day 1 Tornado Outlooks from the Storm Prediction Center (SPC) for 0100 UTC to 1200 UTC 19 September 2017 (a) and 2000 UTC 19 September to 1200 UTC 20 September 2019 (b).

CHAPTER 3: RADAR AND RAIN GAUGE ANALYSIS

This chapter provides the methods, results, and discussion for the radar and rain gauge analysis for Tropical Storm Imelda. In essence, radar images that have been subjectively analyzed for embedded rotation within convection are spatially and temporally matched with five-minute surface rain gauge observations during a period when extreme precipitation rates occurred. Statistical comparisons are made between the gauge observations that follow radar-indicated rotation and the gauge-recorded rainfall observations that follow radar images that do not contain embedded rotation. The statistical significance of these results is examined using a Wilcoxon Signed-rank test. The purpose of this analysis is to examine the relationship between observed embedded mesoscale/storm-scale rotation and surface rainfall in an LTC environment on very fine spatial and temporal scales. It also aims to quantify the difference in short-term rainfall accumulations when there is rotation present versus when there is not, as well as examine how these differences may compound over longer periods of time. The statistical test in this chapter will also illustrate whether the differences in rain rates under the presence of rotation or no rotation is significant.

3.1 Methods: Gauge Selection and Subjective Radar Analysis

Two dense networks of rain gauge sites, one in Jefferson County, Texas (which includes the city of Beaumont) and one in Harris County, Texas (which includes the city of Houston), offer a unique opportunity to explore precipitation rates during Tropical Storm Imelda at very fine spatial and temporal resolutions (Fig. 3.1). Once filtered for erroneous data, the two networks provided five-minute precipitation data from nearly 250 gauges. Real-time data from the two precipitation observing networks are freely available online (Harris County: https://www.harriscountyfws.org/; Jefferson County: https://dd6.onerain.com/).

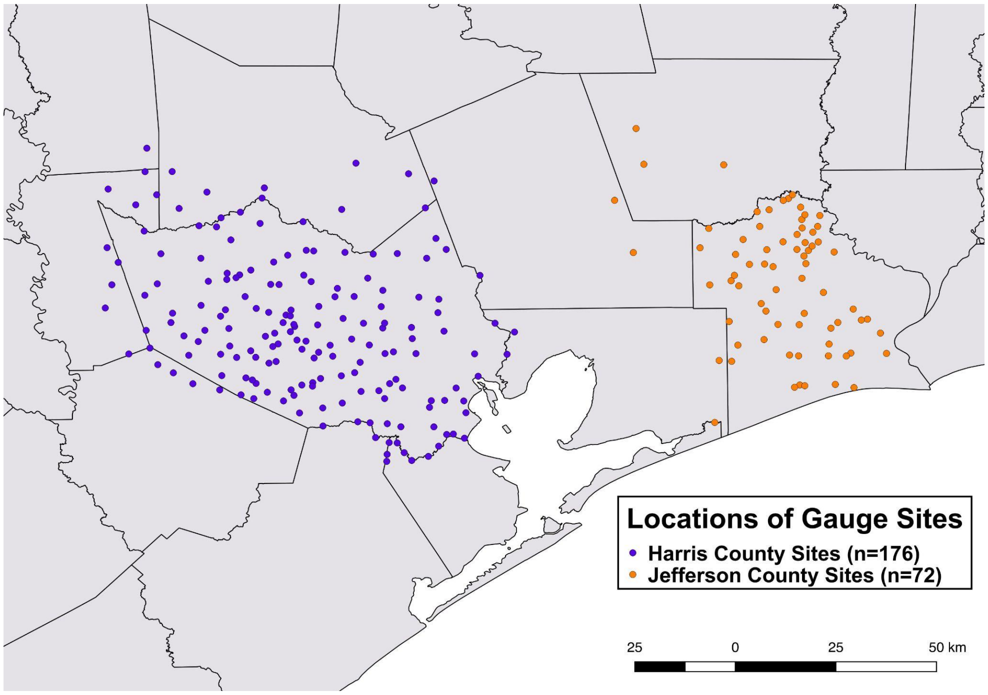

Figure 3.1: Locations of rain gauge sites for the Harris County (purple) and Jefferson County (orange) networks.

Hourly data from the gauges were initially analyzed in order to identify periods during which the heaviest precipitation fell over the time that Imelda was impacting southeast Texas (i.e., approximately 16-20 September 2019). Based on the gauge observations, it was determined that the most extreme precipitation rates took place during much of 19 September. More specifically, the Jefferson County sites received the most extreme precipitation from 0000 UTC to 1400 UTC, while the Harris County sites saw the greatest rainfall rates generally between 1000 UTC to 1800 UTC as the system progressed towards the west-southwest. Fig. 3.2 illustrates these temporal patterns, specifically for gauges that reported an hourly rainfall rate[3] in excess of 100 mm. This time series

[3] Hourly rainfall rates are defined as observations beginning at the top of an hour and ending at the bottom of an hour (e.g., 0000 UTC to 0100 UTC).

reveals that the Jefferson County sites received a much longer duration of heavy rainfall than the Harris County sites due to the slow-moving nature of the system earlier in the period. Additionally,

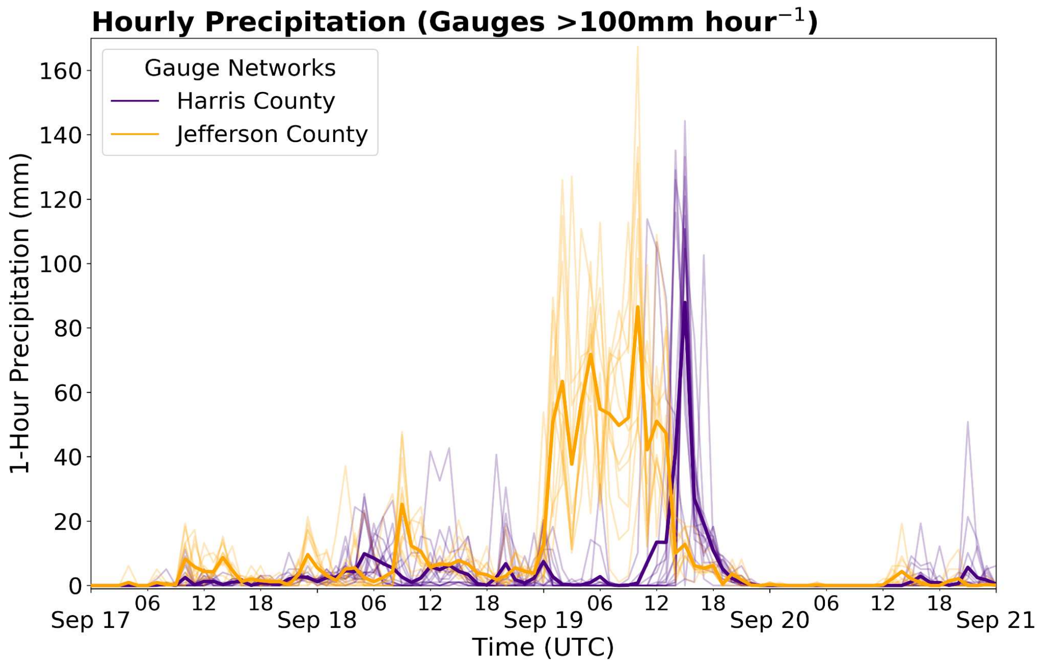

Figure 3.2: Hourly precipitation for gauges receiving over 100 mm h^{-1} during at least one hourly period in the Harris County gauge network (purple) and Jefferson County gauge network (orange) from 0000 UTC 17 September to 0000 UTC 21 September 2019. Note that only 60-minute periods that begin at the top of an hour and end at the bottom of an hour (e.g. 0500 UTC to 0600 UTC) are considered. Hourly data from individual gauges are shown as thin lines, and hourly mean data among the individual sites are shown in bold.

according to Fig. 3.3, the 17 gauges in Harris County that reported an hourly observation that was greater than or equal to 100 mm h^{-1} generally only saw a single, short-lived period with extreme rainfall rates, while heavy rainfall rates were recorded over several separate hours in Jefferson County. These differences are also evident in the footprint of the accumulated rainfall[4] (Figs. 3.4a-b). Further, the magnitude and spatial extent of the hourly rainfall rates by the system are generally lower in the latter part of the 0000 UTC-1800 UTC period as well (i.e., when the Harris County gauges recorded their

[4] According to the Multi-Radar Multi-Sensor (MRMS) local gauge bias-corrected quantitative precipitation estimate. This dataset will be discussed further in Chapter 4.

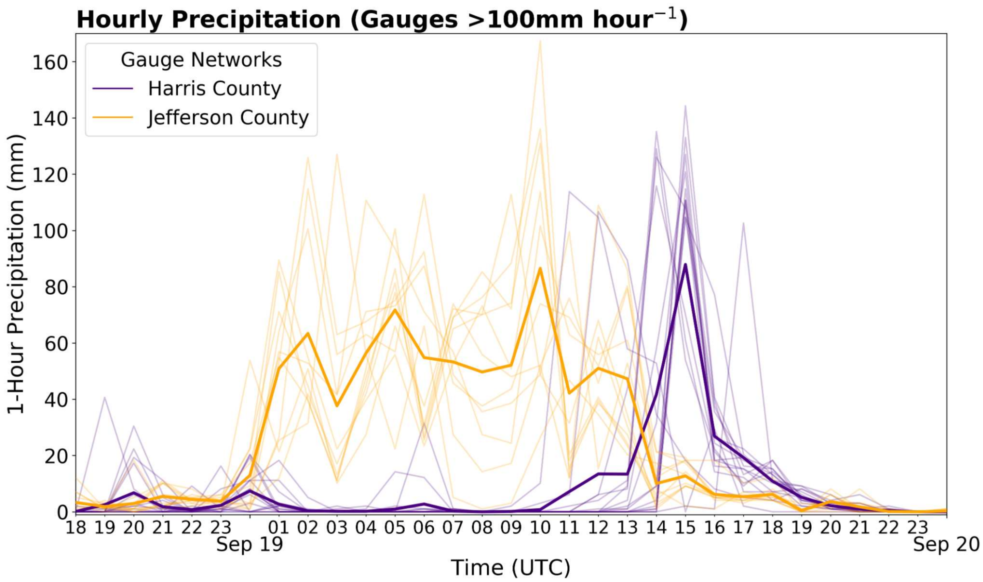

Figure 3.3: As in Fig. 3.2, but zoomed in to 1800 UTC 19 September to 0000 UTC 20 September.

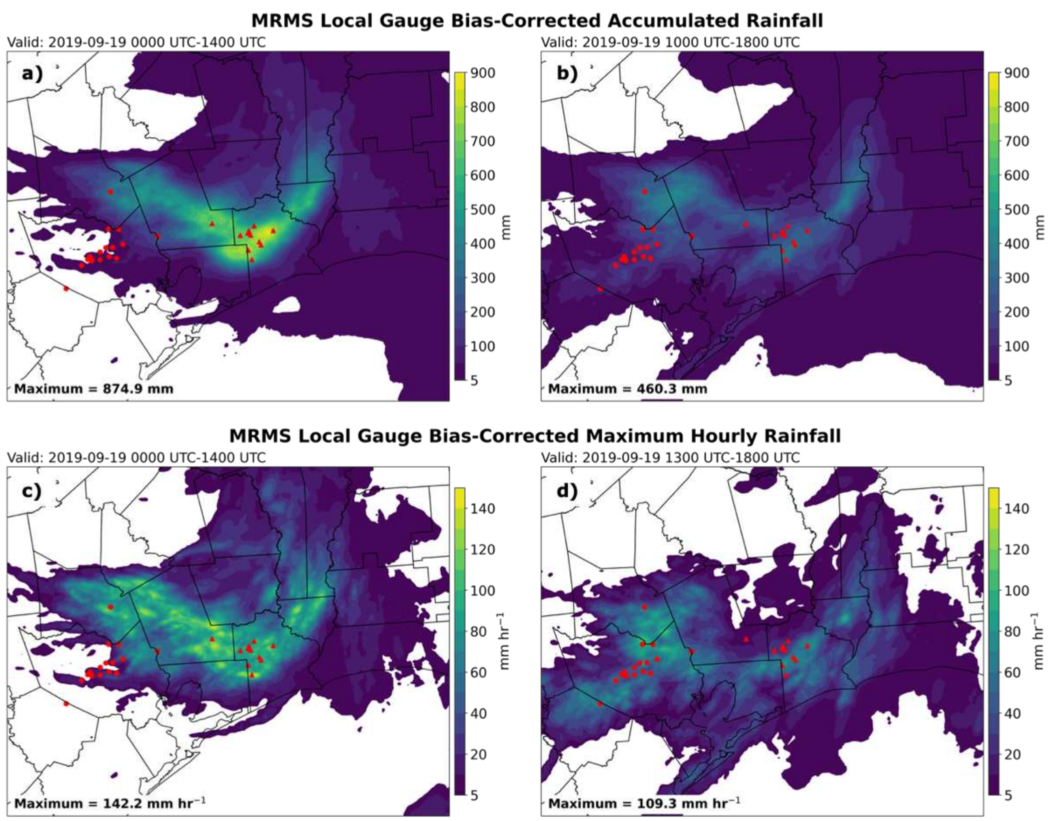

Figure 3.4: Multi-Radar Multi-Sensor (MRMS) local gauge bias-corrected quantitative precipitation estimate (QPE) for 0000 UTC -1400 UTC 19 September 2019 (a) and 1000 UTC -1800 UTC 19 September 2019 (b). Also shown is maximum MRMS one-hour (beginning at the top of the hour and ending at the bottom of the hour, e.g. 0300 UTC -0400 UTC) QPE over the 0000 UTC -1400 UTC 19 September (c) and 1300 UTC -1800 UTC 19 September (d) periods. The circular (triangular) markers represent the Harris (Jefferson) County gauge sites that received ≥ 100 mm h^{-1} of rainfall (using the definition described in Fig. 3.2). Note the difference in time periods between (b) and (d), as the rain rates ≥ 100 mm h^{-1} occurred over most of the plotted Harris County gauge sites after 1300 UTC.

highest hourly values) (Figs. 3.4c-d). For these reasons, only the Jefferson County sites were focused on for this part of the analysis. Specifically, the 11 gauges from the Jefferson County gauge network that recorded hourly rainfall rates in excess of 100 mm h^{-1} were included. Though this threshold is relatively high, the Jefferson County gauge network is very spatially dense compared to typical gauge networks, so this benchmark coincides with thresholds in previous work that have studied observed rotation alongside high-resolution precipitation datasets (e.g., NCEP Stage IV gridded precipitation, which was used in Nielsen and Schumacher (2020a).

With the five-minute precipitation data collected and the period of heaviest rainfall identified, Level II reflectivity and storm-relative velocity from the Houston-Galveston NEXRAD WSR-88D radar (KHGX) were then used to subjectively determine rotation within convection. Each gauge was centered within its own unique domain of size +/-0.15° latitude and +/-0.17° longitude relative to its coordinates, which equated to an area of approximately 33 km x 33 km. This size domain proved to be best suited for monitoring storm-scale rotation after several rounds of trial and error. KHGX radar data was then overlaid with each Jefferson County gauge site of interest over the period when the most extreme rainfall rates were reported by the gauges (i.e.,0000 UTC to 1400 UTC on 19 September) (Fig. 3.3). This process yielded a total of 1067 images over the 14-hour period for the 11 gauge sites.

Next, the radar frames centered over each of the 11 gauges were paired with gauge observations for each radar timestamp. Because the time steps between the two types of observations were available at different time intervals (i.e., archived radar imagery was available every 8-9 minutes and gauge data was available every 5 minutes), the pairings are irregular in time. Thus, each radar frame was paired with the gauge observation that most closely followed the radar timestamp (e.g., if the radar image showed data for 1018 UTC, the gauge observation taken at 1020 UTC would be matched with that particular image). With this method, the time difference between the radar image and the gauge observation could vary anywhere between one and five minutes. Note that if the radar image and gauge observation were to occur at the same time, the gauge reading that occurred 5 minutes after the radar timestamp was used (rather than the gauge observation that occurred at the same time as the radar image). The purpose of taking this measure is to account for time lag between the rotational behavior aloft and the surface precipitation.

Once the radar timestamps were paired with the surface observations, the subjective analysis for each radar image was conducted. Each image was classified into one of two categories, "rotation images" or "non-rotation images", based on the appearance of the KHGX Level II reflectivity and velocity data within each ~33x33 km domain. Rotation was permitted to occur anywhere within the domains and did not necessarily have to be directly located over the gauge site in the image.

Given that the subjective nature of this portion of the analysis allows room for human error, each image was carefully assessed three different times, with the criteria becoming stricter for each round of analysis. This was to ensure that only images containing relatively strong, well-defined, storm-scale rotation were classified as rotation images. During the first pass of the images, images containing embedded storm-scale rotation of any magnitude were classified as "having rotation". In the second round of analysis, the rotation images were further refined by ensuring that the rotation occurred in an area of high reflectivity (i.e., approximately 40 dBZ or higher). This step was done in order to remove cases where rotation was detected in a stratiform precipitation or precipitation-free region. The remaining rotation images were reviewed a final time to filter out images that showed particularly weak and/or disorganized rotating convection, as well as to remove images where the rotation was located on the cusp of the gauge-centered domains and was therefore barely located within the domain. An example of a rotation image versus a non-rotation image is shown in Fig. 3.5.

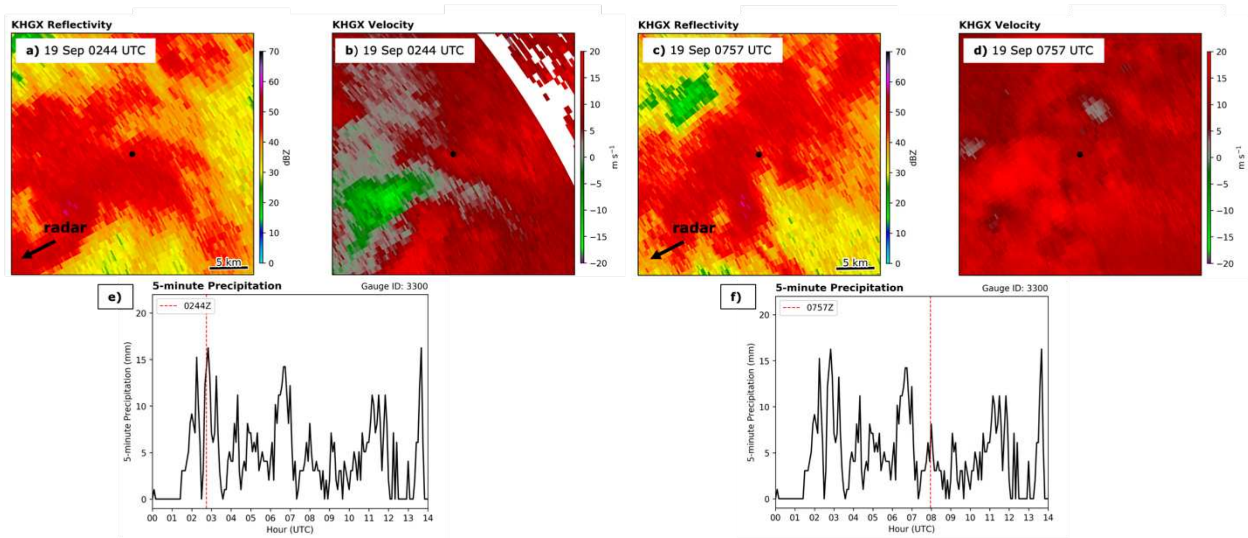

Fig. 3.5: Example of a rotation image showing embedded rotation within convective precipitation based on reflectivity (a) and storm-relative velocity (b) from the Houston-Galveston radar (KHGX) at gauge site 3300 in the Jefferson County gauge network on 19 September 0244 UTC. This is contrasted with KHGX reflectivity (c) and storm-relative velocity (d) for a non-rotation image at the same gauge site. The black dot in the center of (a)-(d) is the gauge site, and the location of the radar relative to the gauge site is shown in (a) and (c). The 5-minute precipitation observations from the gauge site are shown in (e) and (f) (black line) with the time of the radar images corresponding to (a-b) and (c-d) annotated in (e) and (f) respectively as a red dashed line.

Distributions of the rainfall following rotation images versus rainfall following non-rotation images are assessed statistically. These data are separated into two categories for analysis: one set that contains the rainfall observations following all of the radar images collected (n=1067) for all 11 gauges, and a second, smaller set that removes the zero precipitation observations that follow the sample of rotation and non-rotation images (n=859). These sets of rainfall observations will hereafter be referred to as “all_data” and “no0_data” respectively. The two datasets are assessed for statistical significance using a method described in the next subsection.

3.2 Methods: Wilcoxon Signed-rank Test

To assess the significance of the results of the radar and rain gauge analysis, a Wilcoxon signed-rank test is conducted between the five-minute rainfall observations that correspond to the radar images with rotation and the rainfall observations corresponding to the radar images without rotation. This test is used because it is applicable for comparing the distributions of non-parametric data that are not independent (Wilcoxon 1946; King and Eckersley 2019). The appropriateness of these assumptions in this study is discussed in the results. The test is performed twice: once for all_data, and once for no0_data. The aim of this test is to evaluate the significance of the differences in the rainfall observations following rotation and non-rotation images by examining the sums of the ranks of these differences.

SciPy (Virtanen et al. 2020) has a built-in function that computes the Wilcoxon signed-rank test statistics and associated p-values, and its methods closely follow those found in the literature (e.g., King and Eckersley 2019). In essence, the differences between paired observations are calculated and ranked in order of the absolute value of their magnitude, and then the ranks are summed in two groups: one for the ranks belonging to positive differences, and one for the ranks belonging to negative differences. Note that the method chosen here discards all zero differences in the ranking process (which yielded very similar results to other methods that handle zero differences in other ways, not shown). Though the literature is consistent on using the smaller of the positive or negative ranked sum for a two-tailed test (e.g., Wilcoxon 1946; King and Eckersley 2019), there is more debate on which should be used in one-tailed tests. The SciPy function uses the sum of the positive ranks to calculate the test statistic when a one-tailed test (which will be used in this study) is performed. Thus, the default setting using the sum of the positive ranks is used to calculate the test statistics, but the results are briefly compared to the test statistics computed with the sum of the negative ranks. Once the sum of the positive ranks is determined, the test statistic and associated p-value can be calculated. The test statistic is computed with the following equation:

$$z = \frac{w - \frac{N(N+1)}{4}}{\sqrt{\frac{N(N+1)(2N+1)}{24}} - t} = \frac{w - \mu}{\sigma - t} \qquad \text{(Eq. 3.1)}$$

where z is the test statistic, w is the sum of the positive ranks, N is the number of pairs with a non-zero difference, μ is the mean, σ is the standard error, and t is a correction factor for tied ranks.

In this study, because the number of images containing rotation is greater than the number of images that do not contain rotation in both all_data and no0_data, an adjustment must be made so that there are an equal number of observations that can be evenly paired, which is a requirement for the Wilcoxon signed-rank test. Therefore, a random sample equal to the length of the precipitation observations following the non-rotation images is selected from the set of precipitation observations that follow the rotation images. The rainfall observations associated with no rotation can then be paired with the randomly chosen rainfall observations associated with rotation, and the test statistic and p-value can be calculated. This process is repeated with randomly selected pairs 100,000 times each for all_data and no0_data, and the mean rank sum, mean test statistic, and mean p-value are computed for both datasets. Thus, the variables described in Eq. 3.1 will all be mean values hereafter. 100,000 iterations were performed because the mean statistics were approximately the same when multiple trials were run using this number of iterations.

A one-sided test for significance is conducted for both all_data and no0_data using a significance level of α=0.01. The one-sided test is used over the two-sided test because it is anticipated that the images containing rotation will tend to have higher rainfall than the images that do not contain rotation, so the test is being conducted a priori. The null hypothesis is that the median of the differences between the precipitation observations following the rotation and those following non-rotation images is less than zero. In other words, the difference in the distributions of the rainfall following rotation images minus the rainfall following non-rotation images will be negative, suggesting that more rain would have tended to follow non-rotation images. Therefore, the alternative hypothesis is that the median of these paired signed differences in observations is greater than zero. That is, the calculated median of the signed differences (when non-rotation precipitation is subtracted from rotation precipitation) is greater than zero, suggesting that more rainfall tended to fall after rotation images compared to non-rotation images.

3.3 Results and Discussion

3.3.1 Basic Statistics

When all 1067 analyzed images (all_data) are considered, 616 radar images (57.73%) were found to have rotation while 451 (42.27%) were determined to have no rotation present (Table 3.1). Of these 1067 images, approximately 20% (208) of the five-minute rainfall observations associated with them showed records of zero precipitation (Table 3.1), 91 (117) of which were associated with rotation (non-rotation) images. Therefore, to construct no0_data, approximately one in four rainfall observations following non-rotation images were removed while about 15% of the rainfall observations following rotation images were removed. In virtually all radar images that were analyzed, there was some hydrometeor-related reflectivity values present within the domain around the gauge site, meaning that the zero observations that were recorded were almost never a result of precipitation simply not being present within the domain surrounding the gauge site. Instead, zero observations were recorded as a result of either the high reflectivity values (and embedded rotation, if applicable) being located within the domain but not directly over the gauge site, or they occurred as a result of the temporally irregular pairings of the radar images and gauge observations. That is, the non-zero 5-minute rainfall associated with high radar reflectivity (and also co-located rotation in some cases) that was present over or very close to the gauge site may have occurred in the observation period just before or after the one that was paired with the radar image. Nonetheless, removing the images paired with 5-minute rainfall observations of zero left 525 (334) rotation (non-rotation) images and rainfall observations in no0_data, which represented 61.12% and 38.88% of the dataset respectively (Table 3.1).

Table 3.1: Cross-tabulation of 5-minute rainfall observations following non-zero precipitation images (no0_data), zero precipitation images, and all images (all_data) based on whether or not the image contained subjectively-identified rotation. Row-wise and column-wise percentages are also computed against the total number of images.

	Non-zero Images	Zero Images	All Images
Rotation Images (row %) (column %)	525 (85.23%) (61.12%)	91 (14.77%) (43.75%)	616 (100%) (57.73%)
Non-rotation Images (row %) (column %)	334 (74.06%) (38.88%)	117 (25.94%) (56.25%)	451 (100%) (42.27%)
Total Images (row %) (column %)	859 (80.51%) (100%)	208 (19.49%) (100%)	1067 (100%) (100%)

Examining the five-minute rainfall observations for all_data shows that the mean (median) precipitation observed after rotation images is 5.08 mm (4.06 mm). These values are approximately 1 to 1.5 mm higher than the rainfall following non-rotation images in all_data (Table 3.2). Removing the zero precipitation observations raises all these measures of central tendencies by approximately 1 mm each (Table 3.2). The spread of the distributions (measured by the standard deviation) is very similar among the non-rotation and rotation images across both all_data and no0_data, though the observations following rotation images tended to have a slightly higher degree of spread compared to the observations associated with non-rotation images.

Table 3.2: Summary statistics for the 5-minute rainfall following the rotation images and non-rotation images when examining all images (all_data) and non-zero images only (no0_data).

	Mean 5-min Rainfall (mm)	Median 5-min Rainfall (mm)	Standard Deviation of 5-min Rainfall (mm)	Total 5-min Rainfall (mm)
All Rotation Images (n=616)	5.08	4.06	0.16	3131.13
All Non-Rotation Images (n=451)	3.39	3.05	0.14	1530.60
Non-zero Rotation Images (n=525)	5.96	5.08	0.15	3131.13
Non-zero Non-rotation Images (n=334)	4.58	4.06	0.13	1530.60

When all images (all_data) are examined, the distributions are strongly skewed right for the rainfall observations following rotation images (Fig. 3.6a) as well as the rainfall observations following non-rotation images (Fig. 3.6b). This finding demonstrates that a majority of the five-minute precipitation observations in the dataset are small, while the more extreme readings are rarer. Boxplots confirm this observation, showing that 75% of the observations fall at or below approximately 8 mm

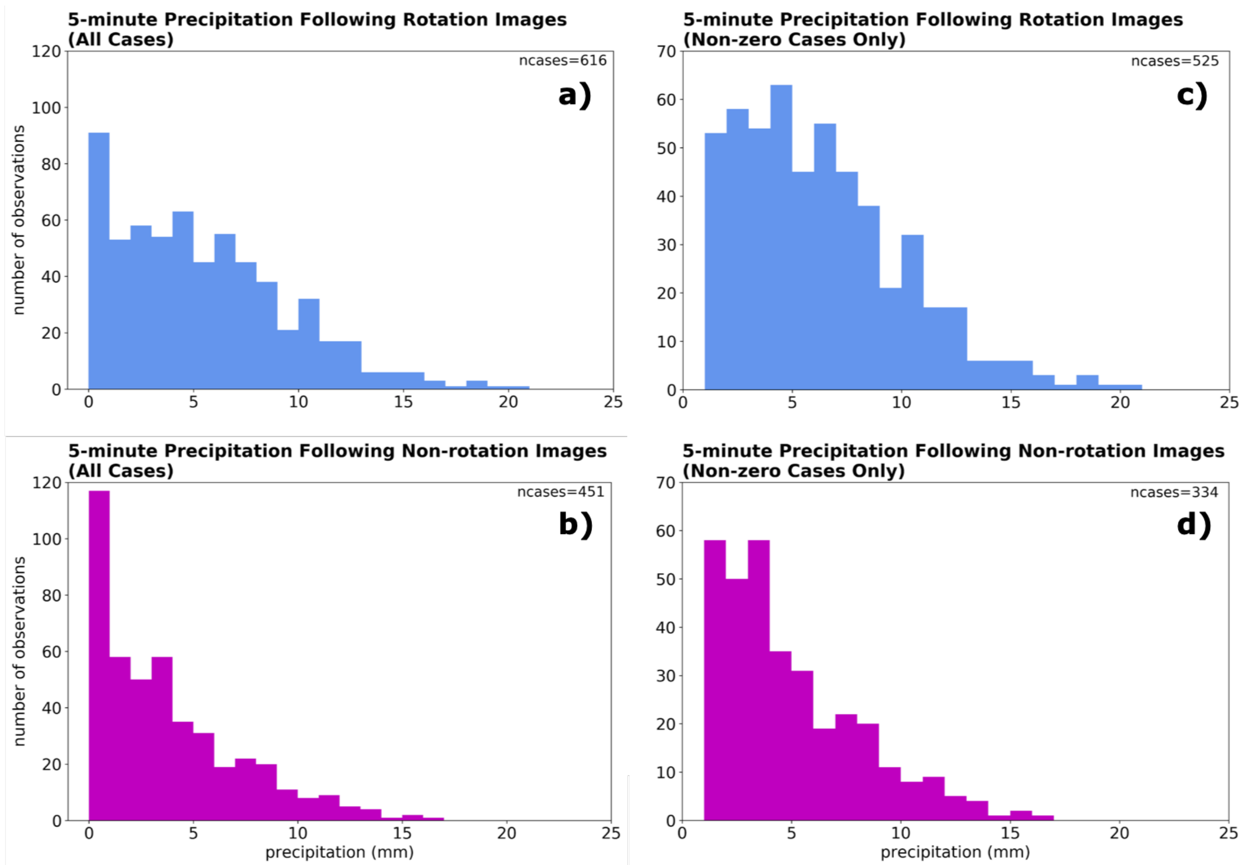

Figure 3.6: Histograms showing the distribution of 5-minute precipitation values from 11 Jefferson County, Texas gauge sites in the minutes following radar images that contain storm-relative rotation (a), (c) or do not contain storm-relative rotation (b), (d) in close proximity to the gauge sites. (a) and (b) correspond to the dataset containing all images (all_data), and (c) and (d) correspond to the dataset containing only non-zero observations (no0_data). The analysis period of the data ranges from 0000 UTC to 1400 UTC 19 September 2019. The number of images is annotated in the upper right corner of each plot. Note the differences in scale on the y-axes.

for the rotation images (Fig. 3.7a) and approximately 5 mm for the non-rotation images (Fig. 3.7b). Fig. 3.7b illustrates that the distribution of the observations following non-rotation images is heavily weighted by the zero observations, demonstrated by the 25th percentile value of 0 mm. It is also evident that many of the more extreme precipitation values follow rotation images rather than non-

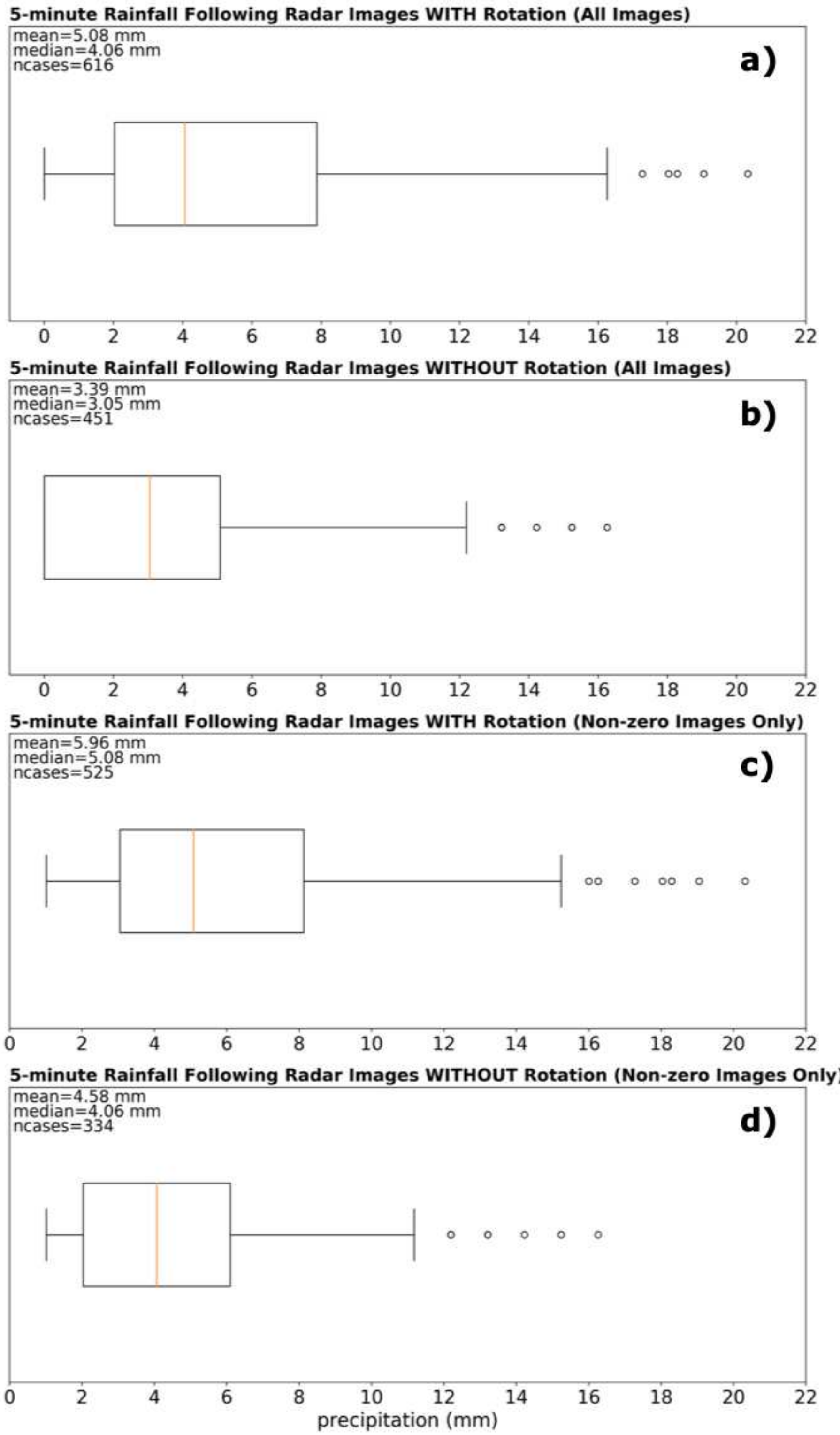

Figure 3.7: Boxplots showing the distribution of 5-minute precipitation values from 11 Jefferson County, Texas gauge sites in the minutes following radar images that contain storm-relative rotation (a), (c) or do not contain storm-relative rotation (b), (d) in close proximity to the gauge sites. (a) and (b) correspond to the dataset containing all images (all_data), and (c) and (d) correspond to the dataset containing only non-zero observations (no0_data). The analysis period of the data is 0000 UTC to 1400 UTC 19 September 2019.

rotation images. In fact, all of the observations following non-rotation images that are considered outliers would fall within the 90th percentile of observations following rotation images (which is approximately 16 mm).

The right-skewness is also obvious in the distributions of rainfall observations following rotation and non-rotation images from no0_data (Figs. 3.6c-d). The histogram of observations following rotation images and the histogram of observations following non-rotation images are identical to their counterparts in all_data, except for the first bin, which is now much smaller due to the removal of the zero-rainfall observations. However, there are several additional differences that can be seen in the boxplots with no0_data (Figs. 3.7c-d) compared to those associated with all_data. Removing non-zero images reduces the standard deviation slightly (Table 3.2) for the observations following rotation and non-rotation images. This is also evident in the shrinking of the interquartile ranges, which results from the 25th percentile increasing and the 75th percentile decreasing. Further, more of the 5-minute rainfall observations on the upper side of the distributions become outliers as the upper maximums decrease.

Though the magnitude of the differences in the observations following rotation images and the observations following non-rotation images may appear small, these differences become much more important when they are compounded over time. Over the 14-hour period, the five-minute rainfall accumulations that were analyzed alongside the radar images totaled approximately 4,662 mm across the 11 gauges. Of this total precipitation, 3131.13 mm of it fell in the minutes after embedded rotation occurred (Table 3.2). In other words, over two-thirds of the rainfall that was included in the analysis fell when rotation was identified in close proximity to the gauge. Scaling by the number of observations to account for the differences in the number of observations, the total precipitation following rotation images is 1913.67 mm, compared to 595.13 mm for the total rainfall following non-rotation images, which further emphasizes the excess rainfall that fell when rotation was present. This finding suggests that while 5-minute rainfall observations do not generally differ much when compared on an individual basis between when rotation is present or not, the small differences can accumulate quickly over time, illustrating that rotation may play a significant role in enhancing surface rainfall.

3.3.2 Statistical Significance

Before assessing the significance of these results, it is important to perform a final verification to ensure that the Wilcoxon signed-rank test is appropriate for the datasets. In addition to the data being non-parametric (which was shown in Figs. 3.6; 3.7), the signed paired differences must also be approximately normal and therefore not highly-skewed (King and Eckersley 2019). This final requirement was stated as an assumption in the methods section because the sample size is large, but it is worthwhile to check this assumption alongside the results. Fig. 3.8 shows the paired signed differences of rainfall (observations following rotation minus observations following non-rotation) for 100,000 random pairings from all_data (turquoise) and no0_data (beige). Indeed, both histograms appear approximately normal and not highly skewed, so the Wilcoxon signed-rank test is valid.

The results of the Wilcoxon signed-rank test show that the null hypothesis can be rejected in both all_data and no0_data. That is, there is significant evidence in both datasets to support the claim that the median of the differences between the rainfall following the rotation images and the rainfall following the non-rotation images is not negative. The mean of the positive rank sums (w) calculated from the 100,000 random pairs are approximately 56900 and 30500 for all_data and no0_data respectively. These values are used to calculate the mean test statistics (z) using Eq. 3.1 after the means of means (μ), and mean standard errors (σ) are calculated from the mean number of non-zero paired differences (N) and made into distributions (using a normal approximation) for all_data and no0_data.

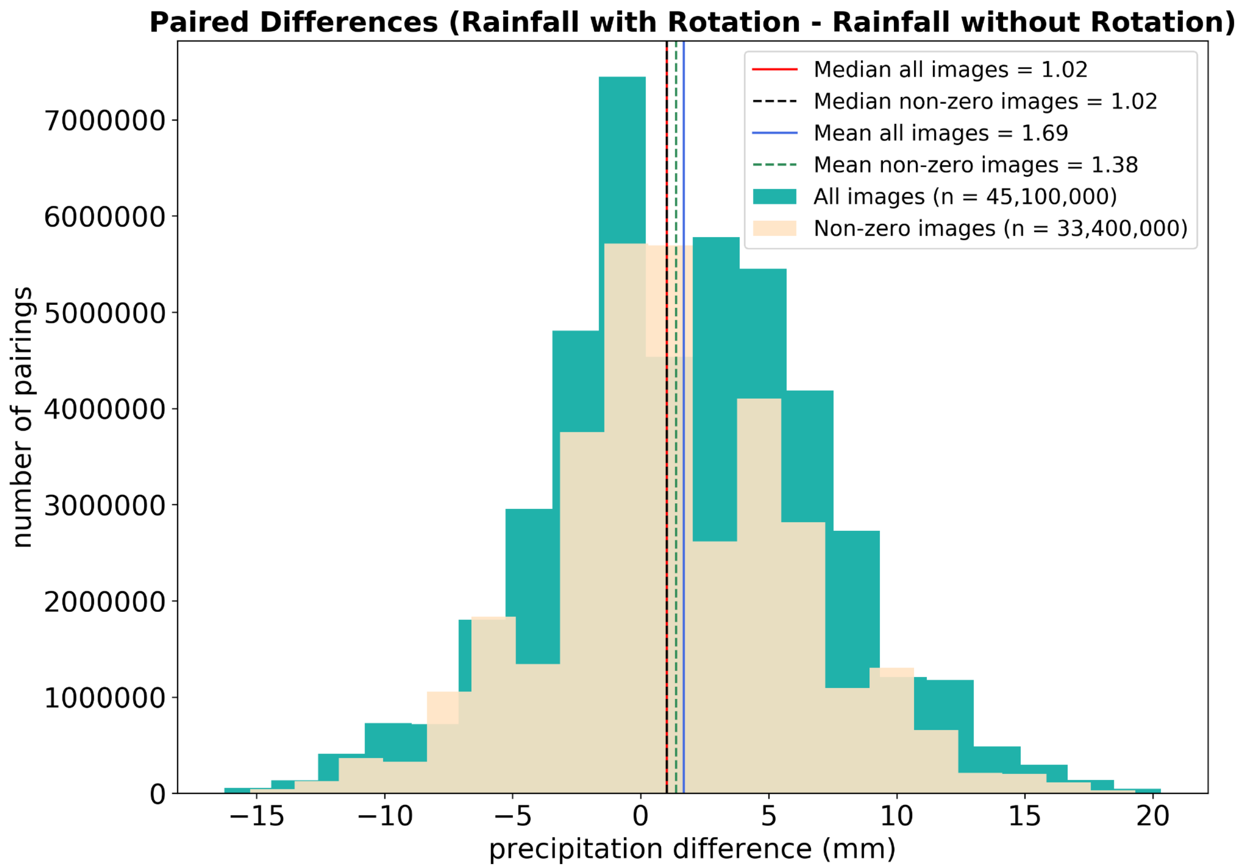

Figure 3.8: Histograms of 100,000 random sets of paired 5-minute rainfall differences for all images (all_data, turquoise) and non-zero images only (no0_data, tan). In both sets of data, the paired differences are found by subtracting the rainfall following an image without rotation from the rainfall following an image with rotation. The medians of the two datasets (which are equal) are shown by the solid red and black dashed line. The mean of the paired rainfall differences for all images is shown as the solid blue line, and the mean of the paired rainfall differences for non-zero images only is shown as the dashed green line.

This test of significance places the means of the positive ranks at approximately 6.4σ (for all_data) and 4.8σ (for no0_data) above μ in the distributions of rank sums (Fig. 3.9), which

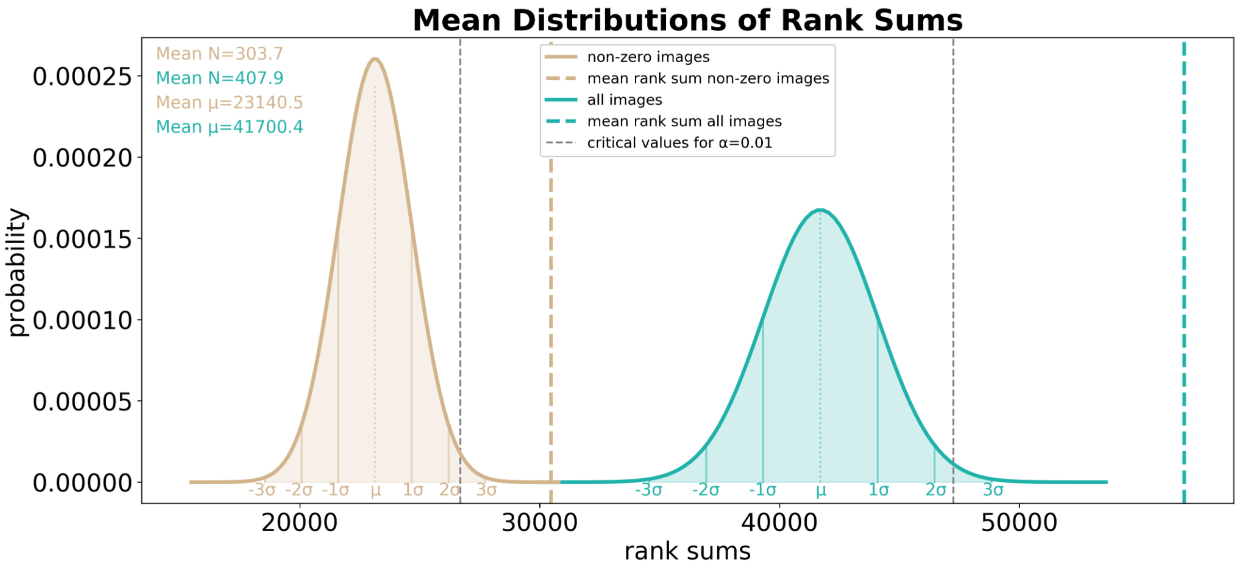

Figure 3.9: Mean probability distributions of the positive rank sums using a normal approximation based on the mean of means and mean of standard deviations from the 100,000 randomly-paired rainfall observations for the rotation and non-rotation images for all images (all_data, turquoise) and non-zero images only (no0_data, tan). Distributions are shown for +-5 mean standard errors (σ), with +-3σ shaded and labeled. The mean of means, μ, are also noted as dotted lines and annotated in the upper left corner with the mean number of non-zero pairs (N) determined through the 100,000 random pairs that were analyzed. The critical rank sum values corresponding to a significance of α=0.01 are shown as grey dashed lines. The mean rank sum values corresponding to the mean test statistics from the 100,000 random pairs are shown as tan and turquoise dashed lines for no0_data and all_data respectively. Note μ and σ are calculated using Equation 1.

corresponds to p-values of approximately $6*10^{-6}$ and $1*10^{-9}$ for no0_data and all_data (respectively) (Table 3.3). These p-values are much smaller than the critical value of 0.01, which leads to the rejection of the null hypothesis. Comparing this result to the mean sums of the negative ranks (Table 3.3) reveals that the means of the negative ranked sums were similarly distant from the mean (except on the left side of the bell curves, rather than the right side). Taking the absolute value of the test statistics calculated from the mean negative ranked sums (King and Eckersley 2019) leads to very similar mean p-values as those calculated using the mean positive ranked sums, which provides additional confidence in these results. Therefore, the results of the Wilcoxon signed-rank test are consistent with the alternative hypothesis, which is that the median of the signed paired differences is not less than zero, but rather, is greater than zero. This conclusion suggests that there is a significant positive difference in the rainfall amounts that follow rotation versus the rainfall amounts that follow no rotation, regardless of whether zero precipitation values are included or not.

Table 3.3: Mean values of the sum of the signed ranks (rounded to the nearest 100), mean test statistics (calculated from the mean sum of positive signed ranks), and corresponding mean p-values resulting from the 100,000 random pairs of rainfall observations following rotation images and non-rotation images when all images (all_data) and only non-zero images are analyzed (no0_data).

	Mean Sum of Positive Signed Ranks (w)	Mean (Abs. Value) Sum of Negative Signed Ranks	Mean Wilcoxon Signed-rank Test Statistic (z)	Mean P-value
All Images	56900	26500	6.4	$1 * 10^{-9}$
Non-zero Images Only	30500	15800	4.8	$6 * 10^{-6}$

One final caveat of this analysis that needs to be addressed alongside the results is the assumption that the data are not independent, particularly because the matched pairs are randomized during the calculation of the test statistic. To check this assumption, the Mann-Whitney U-test is conducted. This test is very similar to the Wilcoxon signed-rank test in that it works for non-parametric data and involves assigning ranks to two sets of data (i.e., rainfall following rotation and rainfall following no rotation), but it assumes independence and can only describe the significance of the difference in medians between two groups of data (King and Eckersley 2019). Calculating the test statistic using this method and the subsequent p-values show very similar results to the p-value calculated with the Wilcoxon signed-rank method (for no0_data) or a p-value that is several orders of magnitude smaller (for all_data). In other words, the Wilcoxon signed-rank method is at least as strict or stricter than the Mann-Whitney U-test for all_data and no0_data, so the assumption of non-independence appears to be not only reasonable but also conservative.

3.4 Summary

In this section, remote data (from radar) are paired with in-situ observations (from rain gauges) to evaluate the relationship between embedded rotation in convective precipitation within the atmosphere with surface rainfall observations during Tropical Storm Imelda. 11 gauge sites located in Jefferson County, Texas reported extreme precipitation rates in excess of 100 mm h^{-1} over a 14-hour period on 19 September 2019. 5-minute observations from the gauge sites were spatially and temporally paired with radar reflectivity and storm-relative velocity fields from the Houston-Galveston WSR-88D radar site (KHGX). The radar fields were used to subjectively identify embedded rotation occurring within convective precipitation near the 11 gauge sites. 5-minute rainfall observations that followed radar images identified as having embedded rotation were compared to 5-minute rainfall observations that followed radar images that did not show embedded rotation.

Of the 1067 radar images that were subjectively analyzed near the 11 gauge sites from 0000 UTC to 1400 UTC on 19 September, approximately 58% of the images contained embedded rotation. This is slightly higher than the percentage of heavy rainfall events that had accompanied rotation in the climatological study of continental convective systems by Nielsen and Schumacher (2020a), though it is difficult to draw comparisons between these two studies given the differences in spatial and temporal scales. Median 5-minute rainfall accumulations for observations following rotation images was 4.06 mm compared to 3.05 mm for gauge observations following the non-rotation images. When images that preceded 5-minute observations that recorded zero precipitation were removed (leaving 859 images), 61% of the images contained subjectively-identified rotation. With these observations removed, the median of the 5-minute rainfall observations following rotation images was 5.08 mm, while the median of the 5-minute rainfall observations following images without rotation was 4.06 mm. All distributions were skewed right, with the majority of the most extreme 5-minute rainfall observations tending to be associated with observations following rotation images. Though these differences may appear small in magnitude, they compound greatly over time, with the total observations associated with rotation images being over twice as large compared to those that followed non-rotation images. This evidence from these observations supports previous work in modelling studies, which have shown that mesoscale rotation can locally increase rainfall rates through dynamic processes (e.g., (Nielsen and Schumacher 2018, 2020b).

The differences in the rainfall observations following radar-identified rotation images and the non-rotation images for the dataset containing all of the observations ("all_data") and the dataset containing only the non-zero rainfall observations ("no0_data") were compared and tested for significance using a one-sided Wilcoxon signed-rank test. To perform the test, observations following non-rotation images and observations following the rotation images were randomly paired 100,000 times for all_data and no0_data. For each iteration, the difference between each pair of rainfall observations was calculated, ranked in order of the absolute value of its magnitude, and given a sign based on whether the difference was positive or negative. Positive ranks were summed, and a test of significance was performed by comparing the sum of the ranks relative to a normal distribution of summed ranks for the given number of non-zero paired differences. When the mean of these 100,000 iterations were calculated for all_data and no0_data, the calculated p-values were $1*10^{-9}$ and $6*10^{-6}$

respectively. These values were much less than the critical value of p=0.01, which supported the alternative hypothesis that the median of the difference between 5-minute rainfall observations following rotation minus 5-minute rainfall observations following non-rotation images was greater than zero, suggesting that the observations following rotation images were statistically significantly greater than those that followed non-rotation images.

CHAPTER 4: MRMS QPE AND ROTATION TRACK ANALYSIS

In this chapter, the spatial and temporal relationship between rainfall and embedded rotation is explored further using Multi-Radar Multi-Sensor (MRMS) data. First, background on the two MRMS products used in this study, one for quantitative precipitation estimate (QPE) and one for rotation tracks, is provided, and their utility in this study is described. Then, once again using the case of Tropical Storm Imelda, the QPE data is overlaid with rotation data over hourly time steps during an 18-hour period of extreme rainfall, then analyzed using three methods—two of which focus on comparing the magnitudes of the two phenomena spatially and one that attempts to examine the co-location of the observations over time. The methods and results of these three analyses are presented in this chapter. Similar to the motivations of Chapter 3, this analysis also seeks to examine and quantify the relationship between embedded rotation and heavy rainfall rates in an LTC environment. However, by incorporating gridded data, the relationship between these two mechanisms can be studied across a continuous area (rather than discrete gauge sites), and embedded rotation is calculated via an algorithm, which removes the subjectivity of the feature identification approach used in Chapter 3.

4.1 Overview of MRMS QPE and Rotation Track Products

The MRMS product suite ingests data from models, radar, satellites, surface observing networks, and more (Smith et al. 2016; Zhang et al. 2016). This study uses two MRMS products to explore the relationship between rainfall and mesoscale/storm-scale rotation in Tropical Storm Imelda. The local gauge bias-corrected one-hour quantitative precipitation estimate (QPE) product is used for accumulated rainfall, and the accumulated 60-minute 0-2 km rotation track product is used to diagnose low-level rotation. Both products ingest new data on a two-minute temporal frequency. New rotation track products are released with each of these updates (i.e., a new rotation track product is available every two minutes with aggregated data over the prior 60 minutes). The hourly QPE product is generated every hour. These QPE and rotation track data sets have horizontal resolutions of approximately 0.01°x0.01° (~1x1 km) and 0.005°x0.005° (~0.5x0.5 km) respectively. The development of these two products, as well as their use and appropriateness for this particular study are described in this section.

4.1.1 Local Gauge Bias-corrected Radar Precipitation Accumulation

MRMS has several QPE products that blend a variety of data sets and are available across several time scales. For this study, the local gauge bias-corrected radar precipitation one-hour accumulation product is used and will therefore be highlighted here. The development of this product relies on data from radars, gauges, and model inputs (Zhang et al. 2016). A summary flowchart for the creation of this product can be found in Fig. 4.1.

The origins of the radar-based QPE component of the MRMS gauge bias-corrected QPE product can be traced back to single-radar reflectivity. First, reflectivity data from all available tilts that is quality-controlled through a neural network (Lakshmanan et al. 2014) is converted from polar to cartesian coordinates (Smith et al. 2016). The cleaned reflectivity data from the lowest available elevation angle is then taken for each radar, and gaps due to beam blockage are filled in with data from adjacent azimuths or higher elevation scans (depending on the size of the gap) (Zhang et al. 2016). If applicable, an adjustment (known as the apparent vertical profile of reflectivity, or AVPR, correction)

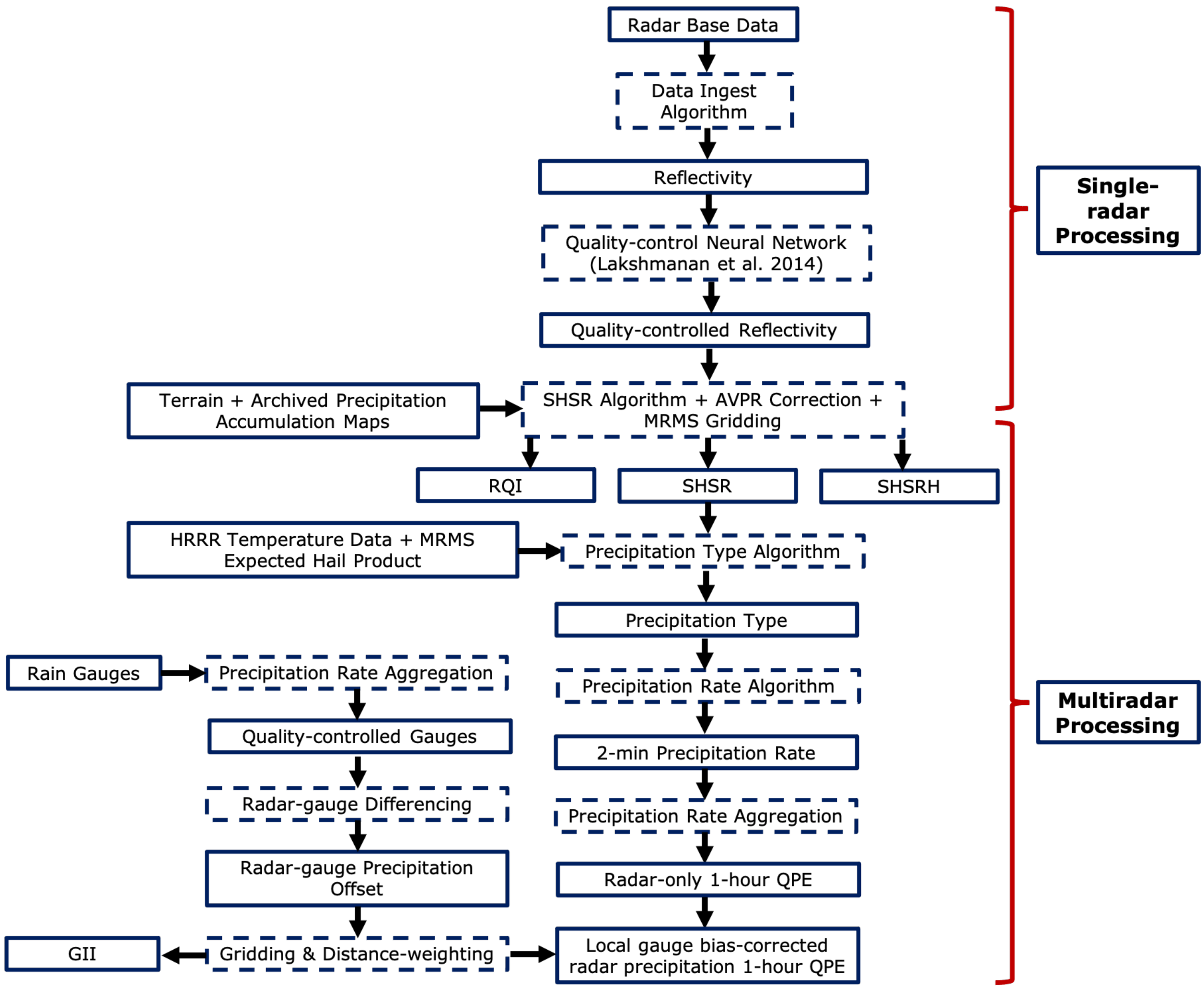

Figure 4.1: Flowchart illustrating the development of the Multi-Radar Multi-Sensor (MRMS) local gauge bias-corrected radar precipitation 1-hour quantitative precipitation estimate (QPE) product as described in Smith et al. (2016) and Zhang et al. (2016). Algorithms are located in the dashed-line boxes, and products are located within the solid-line boxes.

MRMS grid (Zhang et al. 2016). This field, known as the MRMS seamless hybrid scan reflectivity (SHSR), is the base product that is used to create subsequent MRMS precipitation fields, including QPE.

Before a QPE product can be generated, the MRMS precipitation type product is created from the SHSR product (along with temperature information from the High-Resolution Rapid Refresh model (HRRR) and an MRMS hail product) (Zhang et al. 2016). This data, along with the SHSR product is used to calculate precipitation rates. At the time of Imelda, MRMS utilized formulas that relied only on reflectivity data (from SHSR) to calculate precipitation rates, which are permitted to change depending on the MRMS-derived precipitation type (stratiform rain, convective rain and hail, tropical-stratiform mixed rain, or snow) (Zhang et al. 2016). Newer updates to the MRMS system have since introduced more complex formulas for rain rate and QPE products by incorporating several dual-pol variables to the algorithm, which have made the radar-based rainfall estimates more accurate (Zhang et al. 2020), though those updates are not relevant to this particular study (since the upgrade occurred after this event). The precipitation rate calculation is made at a high temporal resolution (every two minutes) and the values are provided in units of mm h^{-1}. The two-minute precipitation rates are totaled over each hour, which yields the MRMS one-hour radar-only QPE product (Zhang et al. 2016).

Incorporating gauge data into precipitation products, such as those in the MRMS suite, adds ground-based, in-situ measurements that remote methods (e.g., radar and satellite) lack. However, surface observations are still prone to errors, so quality control remains a crucial step. The gauge data incorporated into MRMS QPE products is monitored for several error types. The system uses an algorithm that rejects data when the recorded precipitation is too high or low relative to the radar-based QPE, with extra scrutiny applied to gauges located in areas with poor radar coverage (Zhang et al. 2016). Data is also removed by the algorithm when either the gauge or the radar reports non-zero rainfall while the other reports zero rainfall, as well as when the wet-bulb temperature is below 0°C at the gauge site (Zhang et al. 2016). The latter of these controls is implemented because gauges typically underestimate frozen precipitation, particularly as a result of wind-driven undercatch (Goodison et al. 1998; Rasmussen et al. 2012).

For gauges that do pass the validation process, the differences are calculated between the hourly gauge QPE and the hourly radar-based QPE at each site, and the differences are interpolated to the MRMS grid with a distance-related weighting function, and the radar-only MRMS QPE dataset is adjusted based on the gauge bias (Zhang et al. 2016). The aggregated effects of the bias from all gauges on the MRMS gridded QPE products are shown in the hourly-updating MRMS gauge influence index (GII) product (Zhang et al. 2016). GII is relatively high in the region of study given the dense networks of gauges in the area (Fig. 4.2a). However, recalling the gauge datasets used in Chapter 2, it is worth noting that while the Harris County gauges are included in the MRMS product, the Jefferson County gauges are not. Once the gauge data is assimilated and the adjustments are made, the local gauge bias-corrected radar precipitation one-hour QPE product is complete.

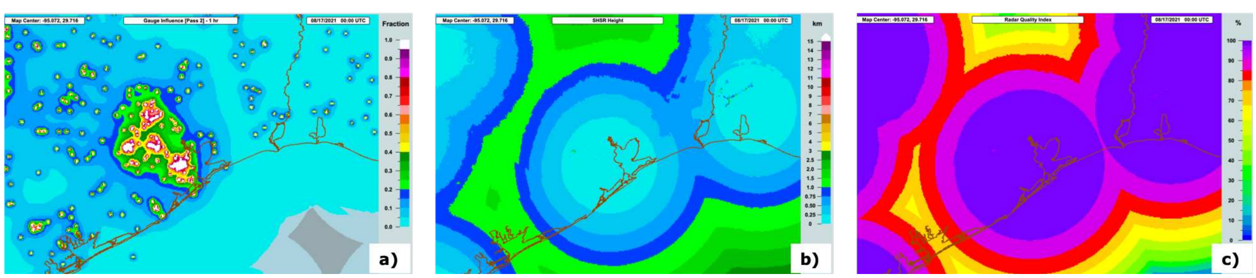

Figure 4.2: Examples of the Multi-Radar Multi-Sensor (MRMS) 1-hour Gauge Influence Index (GII) (a), MRMS seamless hybrid scan reflectivity height (SHSRH) (b), and MRMS radar quality index (RQI) (c) products in southeast Texas during a rainfall event that caused isolated flooding in Houston. Data are shown for 0000 UTC 17 August 2021.

4.1.2 Accumulated 60-minute 0-2 km Rotation Tracks

The MRMS product suite also offers several accumulated rotation-track products (Miller et al. 2013; Smith et al. 2016) that show low- and mid-level rotation (see Fig. 4.3 for a summary graphic of the product development). To generate these products, base radar from individual sites is ingested and

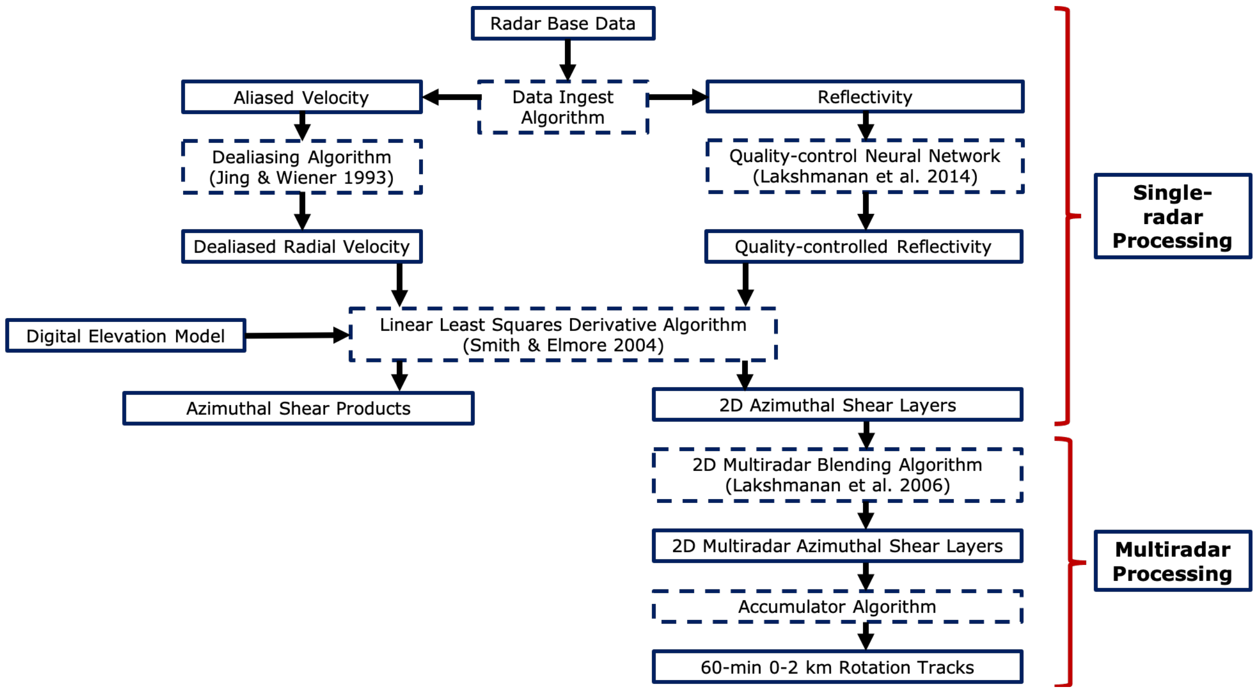

Figure 4.3: Flowchart adapted from Smith et al. (2016) (Figures 1 and 2) and Miller et al. (2013) (Figure 4) summarizing the development of the Multi-Radar Multi-Sensor (MRMS) 60-minute aggregated (2-minute updating) 0-2 km rotation track product. Algorithms are located in the dashed-line boxes, and products are located within the solid-line boxes.

processed, producing radar products such as reflectivity and aliased velocity. The aliased velocity is then dealiased using an algorithm (Jing and Wierner 1993; Miller et al. 2013), and the reflectivity data is quality controlled (Lakshmanan et al. 2014). The dealiased radial velocity data are then ingested into an algorithm that uses a linear least squares derivative method, otherwise known as LLSD (Smith and Elmore 2004). A full derivation of the LLSD method, including the equations used specifically for MRMS data, can be found in Mahalik et al. (2019). In essence, this algorithm computes the partial derivatives of the 2D radial velocity data, which yields a rotational and divergent component (Smith and Elmore 2004). The rotational component, known as the azimuthal shear, is approximately equal to 50% of the vertical vorticity at a given pixel if a symmetric wind field is assumed (Smith and Elmore 2004), which allows it to serve as a good proxy for rotation.

Once the maximum azimuthal shear is calculated along each radial at every vertical tilt of the radar that the radar has, the quality-controlled reflectivity data is incorporated, so that azimuthal shear values that are more than 5 km away from a 20 dBZ pixel are removed (Smith et al. 2016). Two products can be generated from this algorithm. The azimuthal shear product, which shows the azimuthal shear maxima for a given tilt, and the two-dimensional azimuthal shear layer products, which are produced by ingesting terrain data from a digital elevation model (to calculate height above ground level, or AGL) and identifying the maximum azimuthal shear within a vertical layer of interest (Miller et al. 2013). The latter of these two products is implemented in the MRMS system. Specifically, the maximum layer-wise azimuthal shear values are calculated for two vertical layers, 0-2 km AGL and 3-6 km AGL, on a two-minute temporal resolution (Smith et al. 2016). This process is done for every radar site that is incorporated into the MRMS system.

After the single-radar data processing is complete, the data from 173 radars across the United States and Canada are blended using a multi-radar algorithm (Lakshmanan et al. 2006), which leads to the multi-radar, two-dimensional maximum azimuthal shear fields (for 0-2 km AGL and 3-6 km AGL). In the final step, an accumulation algorithm ingests the azimuthal shear data for a given layer and identifies the maximum value for a given location over a two minute time period (Miller et al. 2013; Smith et al. 2016). When the maximum azimuthal shear values over the aggregated time period are plotted, this represents the two-dimensional rotation track product. The maximum values are accumulated over different time intervals (Smith et al. 2016), though this study uses those that are accumulated over a 60-minute time period within the 0-2 km AGL layer. Using this particular product will allow for rotation to be analyzed in the lowest levels (i.e., close to the surface), which is the relevant regime to study its relationship with precipitation at the surface.

4.1.3 Quality of MRMS Data in Southeast Texas

To ensure that MRMS QPE and rotation data is appropriate to use in Southeast Texas, it is important to assess the quality of the radar data being assimilated into the products for that particular region. Fortunately, MRMS provides radar quality index (RQI) products and a SHSR height (SHSRH) product that can help provide insight on the quality of the observations. The SHSRH product shows the AGL elevation at which the SHSR data is coming from (Zhang et al. 2016). Logically-speaking, SHSR data coming from lower elevations will be more representative of what is taking place at the surface compared to data sourced from higher elevations. And because SHSR is used to calculate precipitation rate (and subsequently QPE), better precipitation estimates are produced when data from lower scans are available. RQI, which factors in the radar beam elevation and beam blockage (Zhang et al. 2012), also provides insight on the quality of the radar data being assimilated into the products.

Examining the SHSRH and RQI products during a heavy rainfall event[5] on 16-17 August 2021 that caused isolated flooding in Houston suggest that the quality of the radar data over the Southeast Texas and southern Louisiana region is relatively high. According to the SHSRH product (Fig. 4.2b), reflectivity data for the SHSR product comes from elevations that are less than 1 km for most of the region. This indicates that most of the reflectivity data that is assimilated into the system,

---

[5] Archived SHSRH, RQI, and GII fields were not able to be accessed for dates prior to October 2020, so fields are shown for a recent heavy rainfall event in an effort to draw a close comparison to Imelda.

both for the QPE and rotation products, is sourced from a relatively low elevation. Therefore, it is expected that the radar is likely providing data that is close to what is true near the surface, which is beneficial for both the QPE and the rotation track products. The RQI also suggests that the data quality is relatively good over the region, with most areas showing at least 85% accuracy (Fig. 4.2c). The RQI does degrade slightly in the context of one-hour QPE estimates (not shown), which emphasizes the benefits of using a dataset that incorporates the multitude of gauges in the region (Fig. 4.2a) that can add ground truth. This assessment aligns well with findings by Gao et al. (2021), which showed that MRMS QPE performed reasonably well during several heavy rainfall events across southeast Texas, including Hurricane Harvey (2017) and the Memorial and Tax Day floods (2015 and 2016, respectively), with primarily only small dry biases being the error that was observed.

4.2 Methods

The three methods for analyzing the spatial and temporal relationship between the hourly MRMS local gauge bias-corrected radar QPE (referred to simply as MRMS QPE hereafter) and the MRMS one-hour accumulated 0-2 km rotation tracks (referred to as MRMS rotation tracks hereafter) are described here. All three analyses were conducted over the same 18-hour period of Tropical Storm Imelda: 0000 UTC to 1800 UTC 19 September (using one hour time steps). As has been described previously, this time period was selected because it is when the most extreme rainfall rates occurred during the event, and there were also several persistent embedded rotating features that were present in the convective complex at that time. These features, associated with a back-building convective line, were well-maintained throughout the period based on radar and rain gauge data (see Chapter 3), which provided a reasonably long period to examine rotation and rainfall.

Because the back-building convective line remained nearly stationary for at least 12 hours during the period, the domains for the area of study are relatively small for the analyses. For the first method, the domain bounds are 29° N to 31° N and 93° W to 96° W (red box in Fig. 4.4). For the second two methods, the domain extends from 28° N to 33.5° N and 92° W to 97° W (blue box in Fig. 4.4).

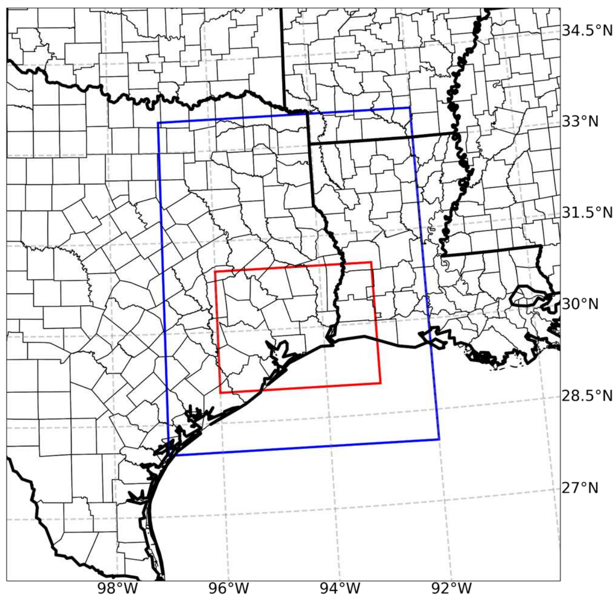

Figure 4.4: The domain for analysis for MRMS Method 1 and MRMS Method 2 (blue) and the domain over which the Hovmöller diagram spatial averaging is performed (red).

In all three methods, the MRMS QPE and the MRMS rotation tracks are overlaid for each time step. However, the relationships between the two datasets will not be assessed pixel by pixel on their native geospatial grids because as is demonstrated in Fig. 4.5, the MRMS datasets, particularly the rotation tracks, can be very noisy. This noise makes it difficult to compare the two datasets grid cell by grid cell. Additionally, the spatial overlap between what is occurring in the atmosphere (even in the low levels) may not perfectly align with the surface. For these reasons, different spatial averaging methods are applied in the subsequent three subsections.

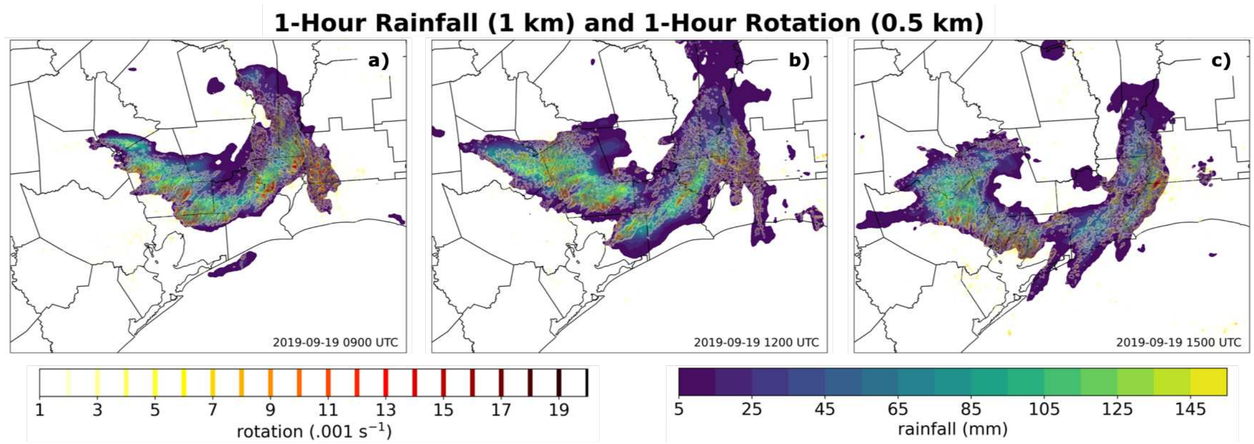

Figure 4.5: Overlaid Multi-Radar Multi-Sensor (MRMS) local gauge bias-corrected one-hour radar quantitative precipitation estimate (QPE) (fill) and MRMS one-hour accumulated 0-2 km rotation tracks (contour) at 0900 UTC (a), 1200 UTC (b), and 1500 UTC (c) on 19 September 2019.

4.2.1 Hovmöller Diagrams

First, in order to provide an overview on the spatiotemporal relationship between the MRMS rotation tracks and the MRMS QPE, Hovmöller diagrams are composed. In essence, the diagrams are constructed by averaging the MRMS rotation data and the MRMS QPE data either across a given latitude range or across a given longitude range for each available time step. Then, these spatially-averaged data are plotted over all time steps.

To construct the diagrams, the MRMS gauge bias-corrected QPE and accumulated 0-2 km rotation tracks are overlaid for each time step before the spatial averaging is performed. Because of the stationary motion of the system, the spatial averaging is done two separate times: once latitudinally and once longitudinally. Each of the spatially-averaged datasets are then plotted separately over time, resulting in two Hovmöller diagrams. The longitude-wise averaging is done between 93° W and 96° W, and the east-west averaged data are shown for latitudes between 29° N and 31° N over the 18-hour period. Conversely, the latitude-wise averaging is done between 29° N and 31° N, with the north-south averaged data shown for longitudes between 93° W and 96° W during the same study period. This approach offers two different perspectives of the embedded rotating features and precipitation over time. Radar images are included and referenced alongside the Hovmöller diagrams during the analysis in order to provide additional context on the structure and motion of the system.

4.2.2 MRMS Method 1

Motivated by the spatiotemporal analysis that stems from the Hovmöller diagrams, these next two methods attempt to quantify the spatial relationship between the MRMS QPE and the MRMS rotation. This analysis is done by applying two different spatial averaging techniques (over two dimensions rather than one, as was done with the Hovmöller diagrams) to the two datasets and comparing their averaged values to each other.

Beginning with a method that will be referred to as MRMS Method 1 hereafter (see Fig. 4.6 for a schematic), the first step in the method is to identify QPE grid points that exceed a certain threshold. Specifically, for each one-hour timestamp, all QPE grid points that exceed 32 mm h^{-1} are selected. For each QPE grid point that meets this criterion, a small box is "drawn" around the individual point. In this analysis, four different sized boxes are tested. The approximate spatial resolutions for each sized box are as follows: 11 km x 12 km, 22 km x 21 km, 33 km x 33 km, and 44 km x 45 km. The spatial resolutions are approximate due to the geographic gridding of the products, which is based on latitude and longitude rather than cartesian distance. The threshold of 32 mm h^{-1} was chosen for two reasons. First, it limited the potential for selecting precipitation that was occurring outside of the main core of the system (where many of the surrounding grid points would be zero, which would make the spatial averages very small). Further, it was the smallest (even-numbered) threshold that could be chosen without causing domain errors when the largest of the boxes (i.e., 44 km x 45 km) were drawn.

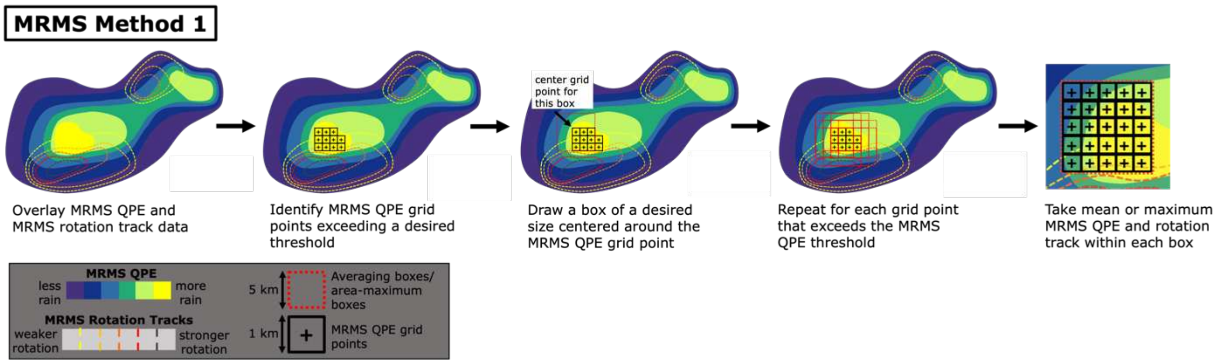

Figure 4.6: Idealized schematic demonstrating Multi-Radar Multi-Sensor (MRMS) Method 1 as described in the text. MRMS local gauge bias-corrected quantitative precipitation estimate (QPE) is shown as the filled contours, and MRMS one-hour accumulated 0-2 km rotation tracks are shown as dashed contours. Magnitudes of the QPE and rotation are shown in the legend. MRMS local gauge bias-corrected quantitative precipitation estimate grid points (1 km spatial resolution) are indicated by black boxes with crosses, and averaging/area-maximum boxes (shown here for a spatial resolution of approximately 5 km) are indicated by red dotted boxes.

Once the boxes are “drawn” for each of the MRMS QPE grid points, the mean of all the MRMS QPE grid points that fall within each of the drawn boxes is taken, as is the mean of the MRMS rotation track grid points that fall within the same box. Note that within each of these boxes, there will be twice as many grid points for the rotation track data than the QPE data since the native spatial resolutions of these products are 0.5 km and 1 km respectively. The area-averaged value of the MRMS QPE box remains paired with the area-averaged magnitude of the MRMS rotation tracks over that same box. For each of the four averaging box sizes that were tested, these paired values are compared to the paired values for other boxes that were drawn based on the 32 mm h^{-1} threshold, and this step is repeated across all 18 hourly time steps.

For an additional perspective, the maximum values, rather than the area-averaged values, within each box drawn around MRMS QPE grid points ≥ 32 mm h^{-1} are also calculated among the

MRMS QPE and MRMS rotation grid points that fall within each box. Then, the paired area-maximum QPE and area-maximum rotation for all boxes are compared against those found within other boxes for each of the four box sizes.

4.2.3 MRMS Method 2

Though methodological limitations will be discussed in further detail in Chapter 5, the motivation for introducing an additional method for assessing the spatial relationship between the hourly MRMS QPE and hourly-accumulated MRMS rotation tracks was due to concerns surrounding oversampling in MRMS Method 1 due to large overlaps between the area-averaged boxes. For instance, two adjacent MRMS QPE grid points that both exceed 32 mm h^{-1} would have boxes that overlap almost entirely, meaning that their area-averaged means would be very similar, and the grid points within the box would be shared with multiple other drawn boxes nearby. For these reasons, an additional method, defined here as MRMS Method 2, was developed to address these concerns by attempting to mitigate the issue of oversampling. A schematic representing the second method is shown in Fig. 4.7.

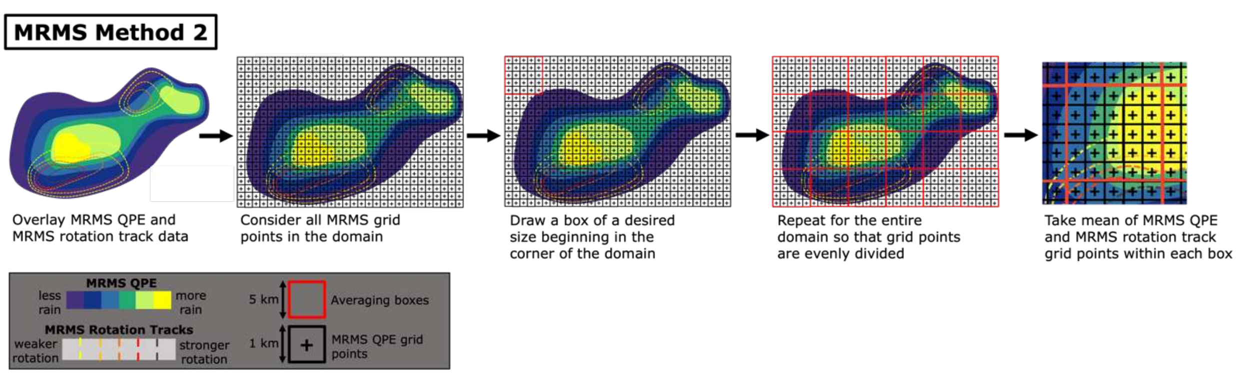

Figure 4.7: As in Fig. 4.6, but for MRMS Method 2, except the averaging boxes are shown as solid (rather than dashed) red boxes (note area-maximum values were not calculated with MRMS Method 2).

Rather than drawing averaging boxes based on an estimated rainfall accumulation threshold, MRMS Method 2 coarsens the MRMS grid independently of the MRMS QPE values. This is done by dividing the domain into equally-sized small boxes that remain spatially identical across the entire period, rather than allowing their locations to vary with each time step based on the locations of the QPE values. Within each of the boxes, the values of the MRMS QPE and MRMS rotation track grid points that fall within the box are averaged. This approach prevents the same grid points from being sampled multiple times and effectively coarsens the grid. This approach is tested using three different coarsened resolutions of approximately 2 km x 2 km, 5 km x 5 km, and 10 km x 10 km (Fig. 4.8). As

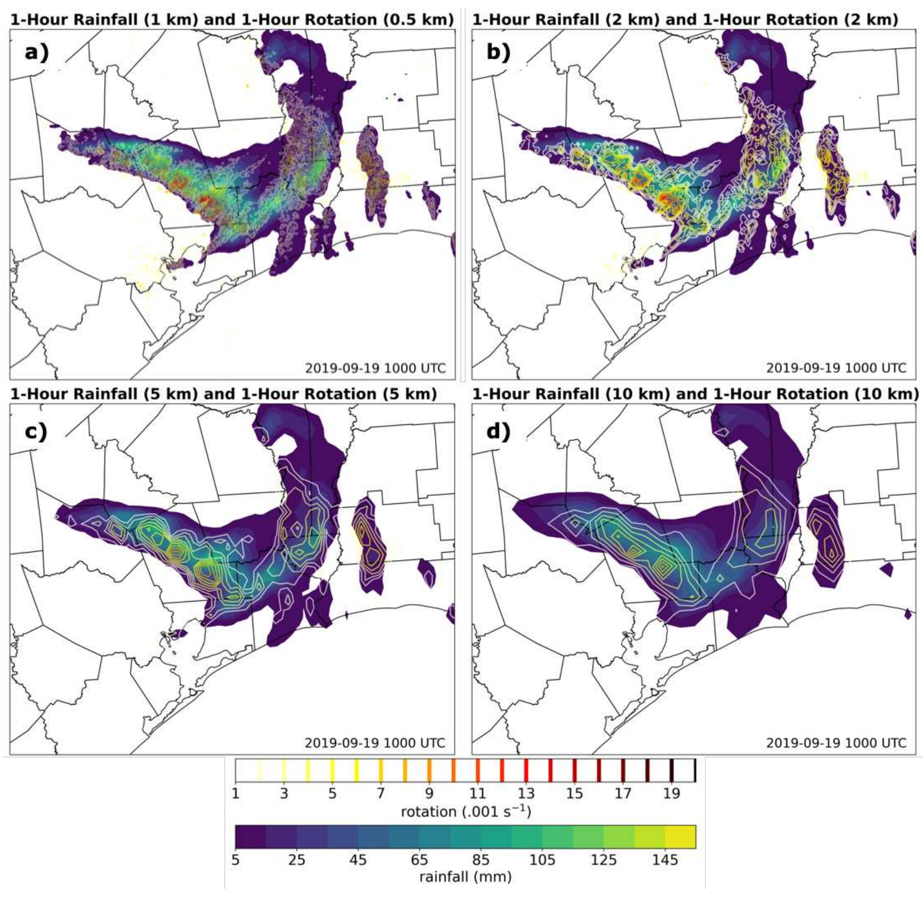

Figure 4.8: Example of the Multi-Radar Multi-Sensor (MRMS) Method 2 grid coarsening for MRMS local gauge bias-corrected one-hour radar quantitative precipitation estimate (QPE) (fill) and MRMS one-hour accumulated 0-2 km rotation tracks (contour) for 19 September 2019 at 1000 UTC. The datasets are shown with the original resolutions (1 km for precipitation, 0.5 km for rotation) in (a), then with their resolutions coarsened to 2 km (b), 5 km (c), and 10 km (d).

with MRMS Method 1, the area-averaged MRMS QPE and MRMS rotation track values for each averaging box remain paired together for analysis across the 18-hour time period. Note that in order to exclude small values in the analysis, only area-averaged values that exceed 0.001 s^{-1} for the MRMS rotation tracks and 4 mm for the MRMS QPE are included.

4.3 Results and Discussion

4.3.1 Hovmöller Diagrams

From the perspective of the longitudinally-averaged Hovmöller diagram (Fig. 4.9), there is evident spatial overlap between the MRMS QPE and the MRMS rotation when viewed over the 18-hour period. During the first four hours of the period, the highest longitudinally-averaged precipitation values are focused near 30° N (Fig. 4.9a), which is where the axis of back-building precipitation began to form (Fig. 4.10a). Around 0500 UTC, east-west averaged precipitation begins to increase as the convective line intensifies (Fig 4.9a), as does east-west averaged rotation (Fig. 4.9b) as embedded rotation begins in the eastward portion of the line (Fig. 4.10b). Longitudinally-averaged rotation begins to intensify again between 0600 UTC and 0800 UTC between 29.75° N and 30.0° N very near a developing precipitation maximum at the same time (Fig. 4.9c). Several rotating elements can be seen within some of the heaviest reflectivity areas (Fig. 4.10c), which aligns well with the longitude-averaged rotation seen in Fig. 4.9b.

The west-northwest east-southeast oriented convective line becomes more well-organized over the next few hours, with embedded rotation present throughout most of it (Fig. 4.11a), which is indicated by the longitudinally-averaged MRMS rotation maximum just north of 30.0° N (Fig. 4.9b). Note that the area of most intense east-west averaged precipitation aligns very well with the averaged

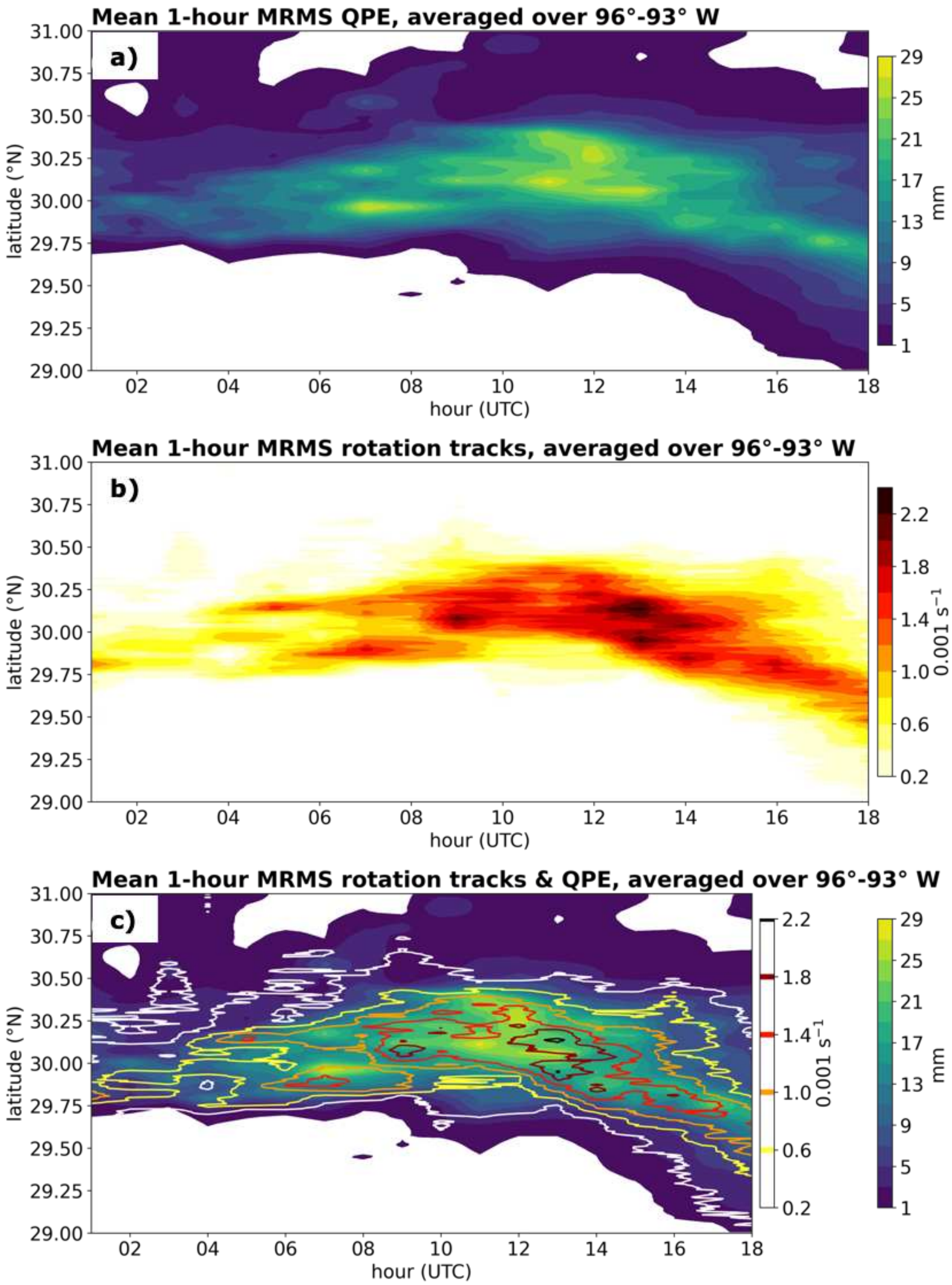

Figure 4.9: Hovmöller diagrams showing mean 1-hour Multi-Radar Multi-Sensor (MRMS) quantitative precipitation estimate (QPE) (mm) (a), mean MRMS one-hour accumulated 0-2 km rotation tracks (0.001 s^{-1}) (b) between latitudes 29° N to 31° N from 0000 UTC to 1800 UTC on 19 September 2019. Data from (a) and (b) are overlaid in (c), with the QPE shaded and the rotation tracks contoured. For all plots, the QPE and rotation tracks are averaged over longitudes 96° W to 93° W.

rotation (Fig. 4.9c). These rotating features remain present for several hours (Fig. 4.11b) as the system begins to bow southward, which is evident from the MRMS QPE footprint (Fig. 4.5c). The

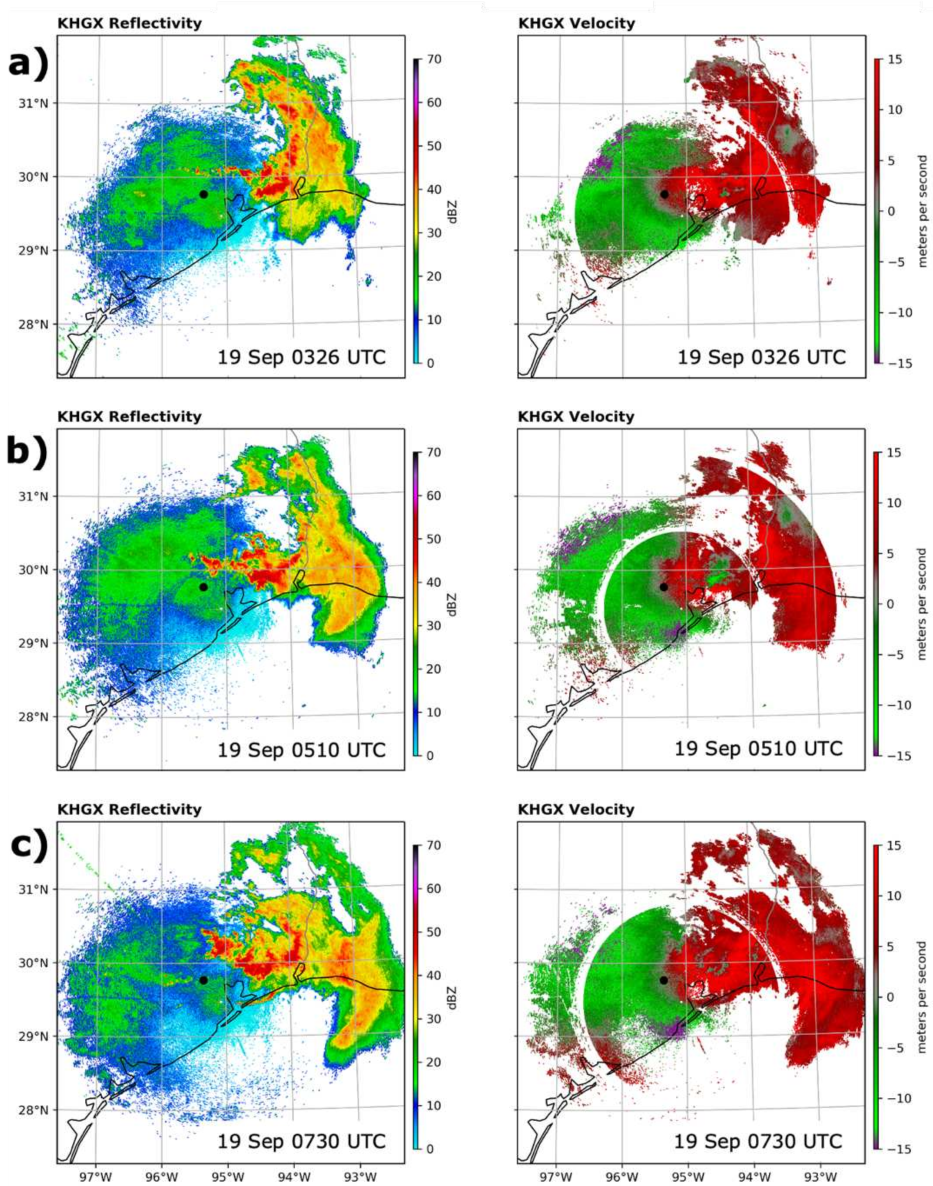

Figure 4.10: Radar reflectivity and velocity from the Houston-Galveston radar in League City, Texas (KHGX) at 0326 UTC (a) 0510 UTC (b) 0730 UTC (c) on 19 September 2019. The black dot indicates the approximate location of downtown Houston, Texas.

convection producing the most intense precipitation can be seen advancing southwestward by 1500 UTC (Fig. 4.9c), though the line slowly begins becoming less organized (Fig. 4.11c).

The north-south averaged MRMS QPE and MRMS rotation fields provide additional insight on the time-evolution of the intense convective band and associated rainfall and rotation (Fig. 4.12a-c). Similar to Fig. 4.9, averaged MRMS rotation and MRMS QPE often overlap spatially with each other

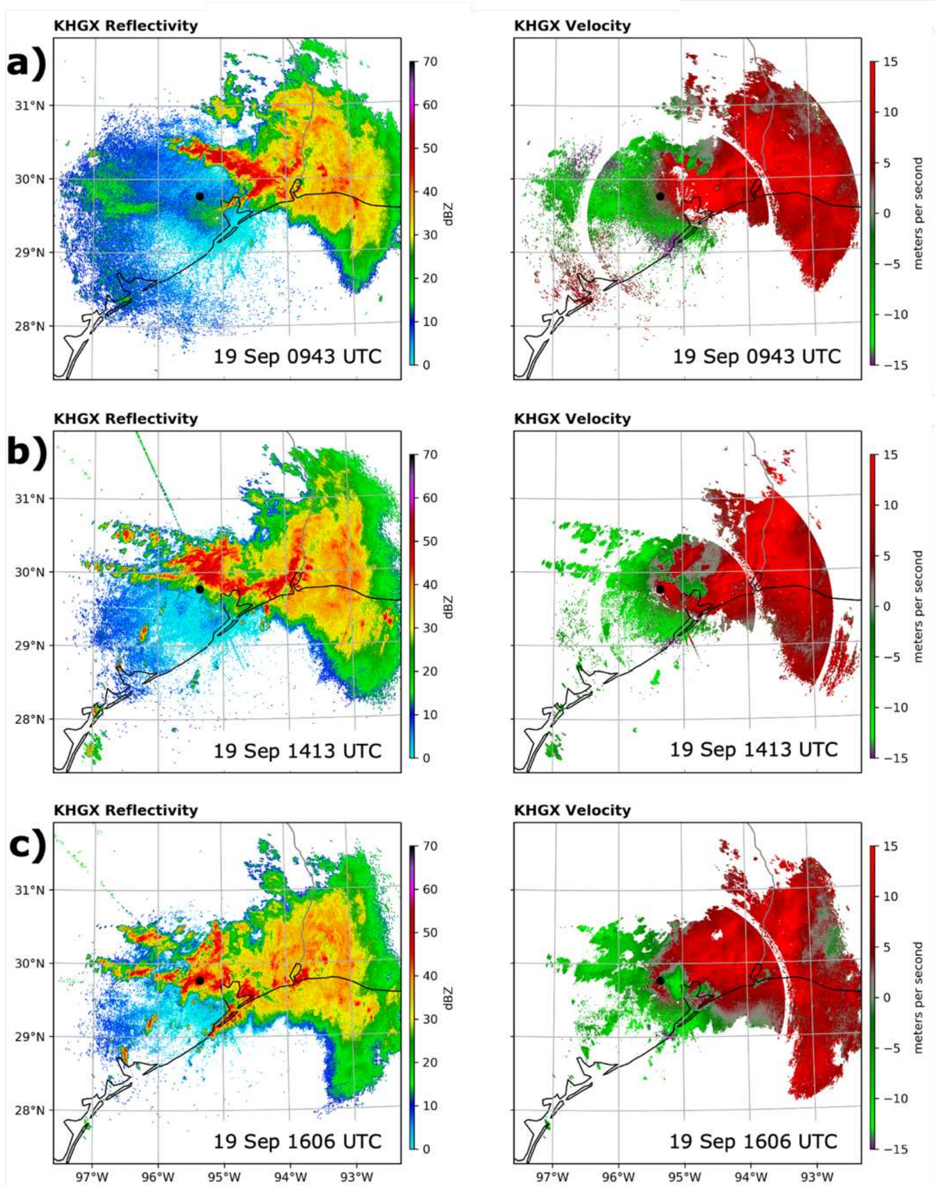

Figure 4.11: As in Fig. 4.10 but at 0943 UTC (a) 1413 UTC (b) and 1606 UTC (c).

across the period. In a general sense, the fields shown from this perspective suggest that the precipitating system becomes longer in the east-west direction throughout the period, as does the extent of the heavier precipitation.

Unlike Fig. 4.9b, Fig. 4.12b shows more clearly that there are multiple areas in the domain that indicate well-maintained embedded rotation. One of these rotating features is present from around

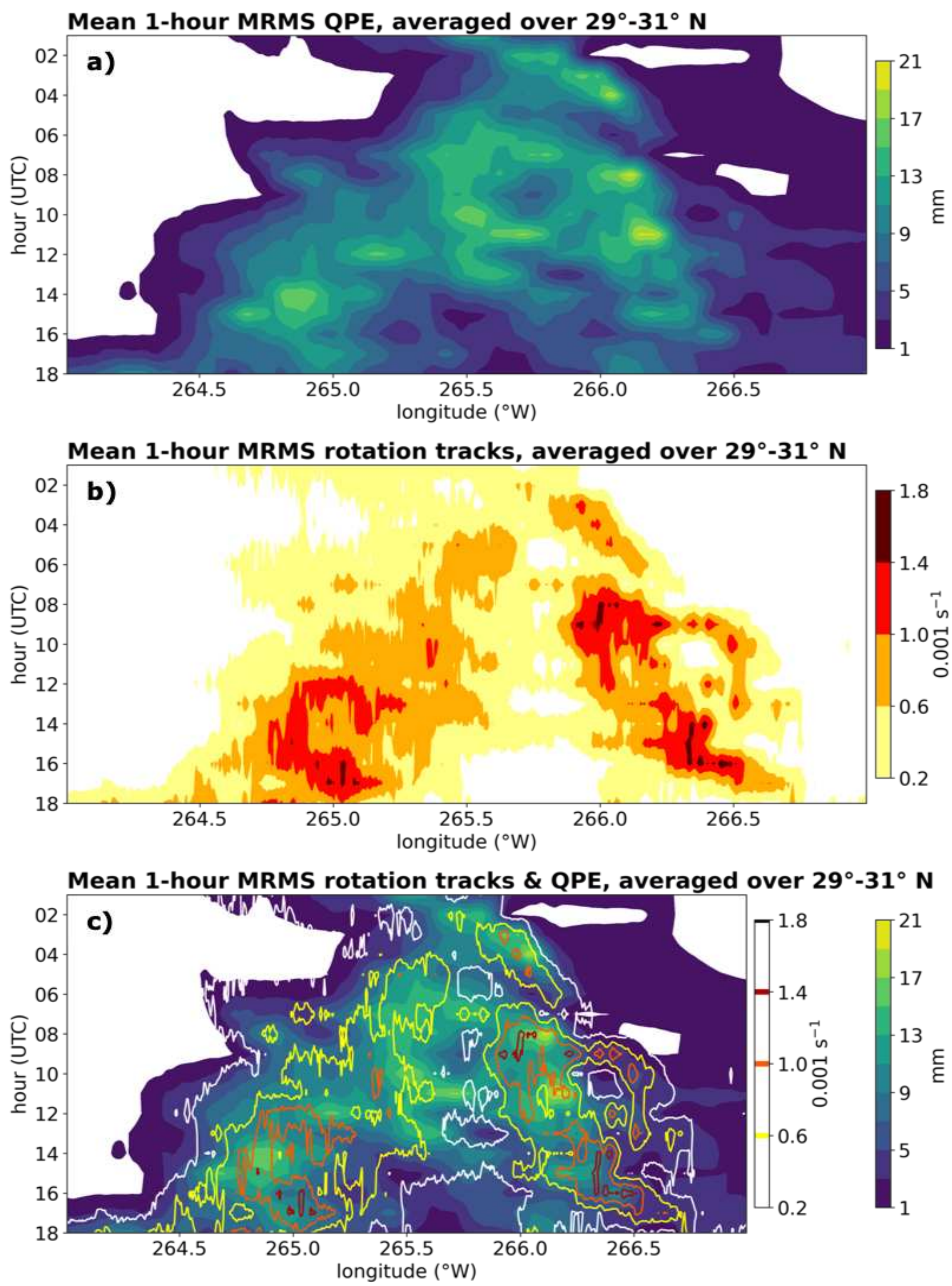

Figure 4.12: As in Fig. 4.9, but averaged over latitude (29° N to 31° N) instead of longitude. Data shown for 93° W to 96° W.

0300 UTC to 0600 UTC (Fig. 4.12b) and appears to originate within an eastward-moving bowing convective band centered near 94° W that originated as a TC rainband (Fig. 4.10a). The northward extent of this north-south oriented band decays over time (Fig. 4.10b), and while KHGX velocity shows little in the way of rotation in the area at this time, the latitudinally-averaged MRMS QPE and MRMS rotation fields indicate eastward propagation of the co-located rotating feature and accompanied rainfall during this time (Fig. 4.12c). A few hours later, another, broader area of latitudinally-averaged rotating features develops after 0700 UTC along a similar line of longitude (Fig. 4.12c). This area of embedded rotation moves very little in the east-west direction through 1300 UTC, and Fig. 4.9b suggests that they do not deviate in the north-south direction very much during this period either, though they do overlap well spatially with the latitudinally-averaged MRMS QPE (Fig. 4.12a). Again, radar images do not indicate very much rotation in the area during these times, though this is likely because the KHGX radar beam may be too high to capture the low-level rotation in this area that would be better detected by the KLCH radar. In the region of this ongoing rotation, the once-broader area of intense convection (Fig. 4.11a) narrows longitudinally into a narrower north-south oriented line (Fig. 4.11b). While the rotating features can be seen moving eastward in Fig. 4.12b, the latitudinally-averaged MRMS QPE do not reflect this eastward motion as clearly (Fig. 4.12a), suggesting a lessening degree of co-location than had been identified previously.

Meanwhile, further west, the orange shades near 94.5° W beginning around 0500 UTC in Fig. 4.12b correspond to the developing rotation within the back-building convective line (Fig. 4.10b). Due to the north-south averaging and the west-northwest east-southeast orientation of the line, these areas of rotation do not appear as intense. Nonetheless, the rotation remains nearly continuous through the end of the period as the line drifts southwestward, with the magnitude of the latitudinally-averaged MRMS rotation and MRMS QPE increasing (Fig. 4.12c) as the system becomes less linear and broadens in the north-south direction (Fig. 4.11b; c). In general, the latitudinally-averaged MRMS QPE and MRMS rotation are co-located quite well throughout the convective line's lifetime.

4.3.1 MRMS Methods 1 and 2

Beginning with MRMS Method 1, 51,276 total grid cells exceeding 32 mm h^{-1} in the one-hour MRMS local gauge bias-corrected QPE product were identified within the established domain (Fig. 4.4) between 0000 UTC to 1800 UTC 19 September 2019. Hexbin plots of the area-averaged hourly MRMS QPE and area-averaged MRMS one-hour accumulated 0-2 km rotation tracks suggest a relatively strong positive relationship between the two variables (Fig. 4.13). This relationship is present

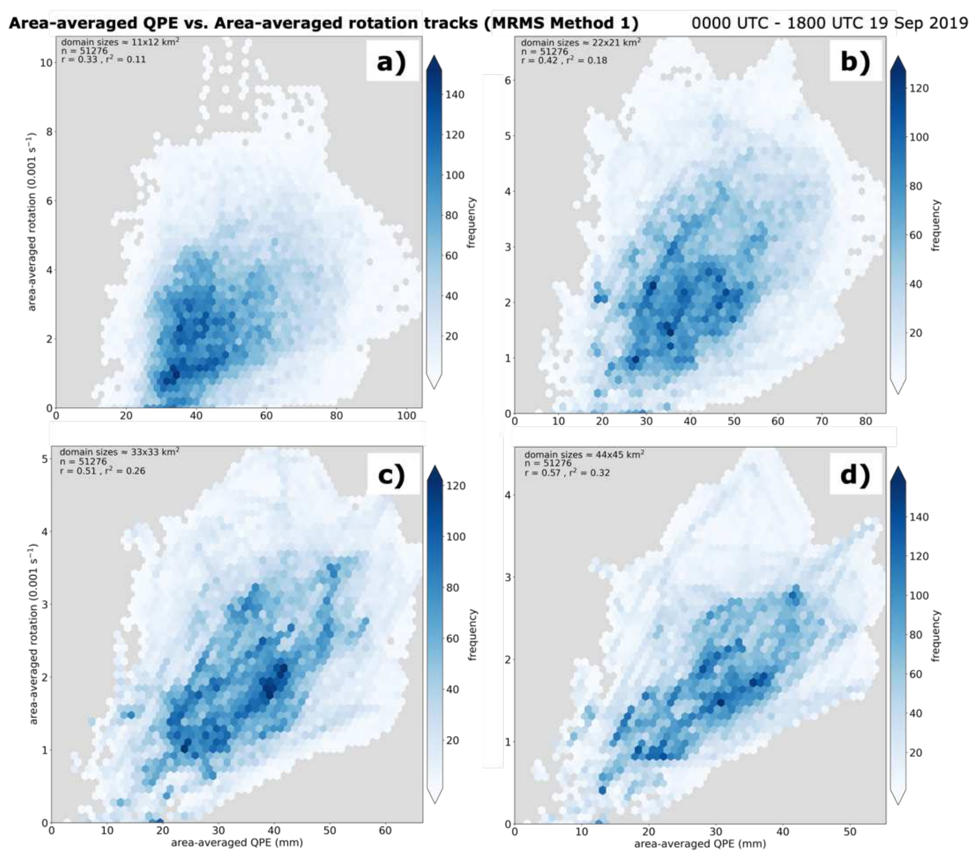

Figure 4.13: Hexbin plots of area-averaged Multi-Radar Multi-Sensor (MRMS) one-hour quantitative precipitation estimate (QPE) (mm) and area-averaged MRMS one-hour accumulated 0-2 km rotation tracks calculated from horizontal domains of approximate sizes of 11 km x 12 km (a), 22 km x 21 km (b), 33 km x 33 km (c), and 44 km x 45 km (d) as described by MRMS Method 1. Note the differences in scale on the colorbars and axes. The number of horizontal domains being sampled (which is based on the number of QPE grid points that are greater than 32 mm h^{-1}) are annotated with the r and r^2 values for each domain size.

regardless of the sizes of the averaging boxes that are used to conduct the spatial averaging, though as the size of the averaging boxes being drawn increases, the correlation also increases. This is not surprising, given that as the averaging boxes become larger in size, there is more overlap between the boxes, meaning that the spatial averages calculated among them become more similar. Therefore, the calculated correlation coefficient (r) is weakest for the averaging boxes of size 11 km x 12 km. This smallest size of averaging box yields a correlation coefficient of 0.33, with the majority of the averaging boxes having an hourly MRMS QPE between 25 mm h^{-1} and 60 mm h^{-1} and mean hourly accumulated rotation track between $0.5*0.001s^{-1}$ and $4.5*0.001s^{-1}$, which equates to an area-averaged mean of 1.8 and 16.2 tracks h^{-1} respectively (Fig. 4.13a).

As the size of the averaging boxes increases, the magnitudes of the spatially-averaged MRMS QPE and MRMS rotation tracks become less extreme (Fig. 4.13b-d). This trend exists because the isolated extreme values begin to get averaged-out as more grid points are averaged together. By the time the box size is 44 km x 45 km (Fig. 4.13d), an r-value of 0.57 is reached, though the area-averaged maximum MRMS QPE and area-averaged maximum MRMS rotation are approximately 55 mm h^{-1} and $4.5*0.001s^{-1}$ respectively, which were characterized more as mid-range values when the averaging boxes were smaller (e.g., Fig. 4.13a).

In addition to examining the area-averaged mean QPE and rotation track values within the various sized boxes, the maximum grid point values found within each of the boxes can also be examined at each time step within the 18-hour period (Fig. 4.14). This perspective is helpful because the grid points with larger magnitudes do not get smoothed out by the averaging. In general, the relationships between the maximum one-hour MRMS QPE and maximum one-hour MRMS rotation taken among the different sized boxes were less strong compared to the area-averaged relationships of the same sized boxes (Fig. 4.14). Notably, the differences in r-values between the area-averaged relationships and area-maximum relationships of the MRMS QPE and MRMS rotation are smaller for the smaller sized averaging boxes (e.g., cf. Figs. 4.13a; 4.14a) than the larger sized averaging boxes (e.g., cf. Figs. 4.13d; 4.14d). While it is interesting that the correlations between the maximum QPE versus maximum rotation values are higher when compared to the correlations of the area-averaged QPE and area-averaged rotation, this result should be interpreted with caution. Care should be taken because the area-maximum values are only representative of a single 1x1 km (for QPE) and 0.5x0.5 km (for rotation) grid point within each of the boxes, meaning that those values may not fully represent what is occurring within each box.

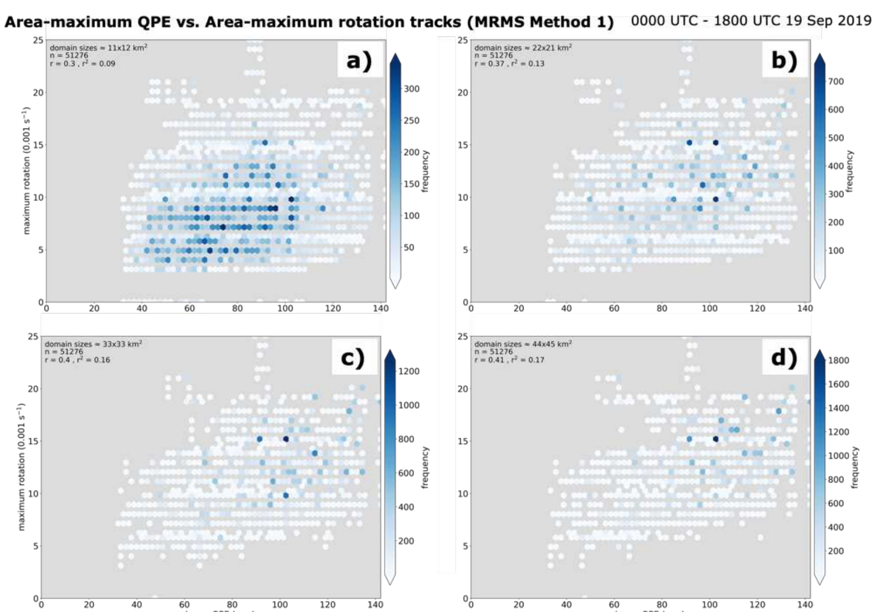

Figure 4.14: As in Fig. 4.13, but for area-maximum Multi-Radar Multi-Sensor (MRMS) one-hour quantitative precipitation estimate (QPE) (mm) and area-maximum MRMS one-hour accumulated 0-2 km rotation tracks. Note the differences in scale on the colorbars and axes.

Analyzing the results of the MRMS Method 2 reveals that there is still a positive relationship between the area-averaged MRMS rotation and the area-averaged MRMS QPE, though the correlations are less strong than those that were found with MRMS Method 1 (Fig. 4.15). Because the oversampling issue is alleviated with MRMS Method 2, it is not surprising that the relationships are not as prevalent, since the values of the averaging boxes being analyzed with this second method will undoubtedly be less similar to each other. As with MRMS Method 1, the correlation between the area-averaged MRMS QPE and area-averaged MRMS rotation increases as the grid becomes coarser.

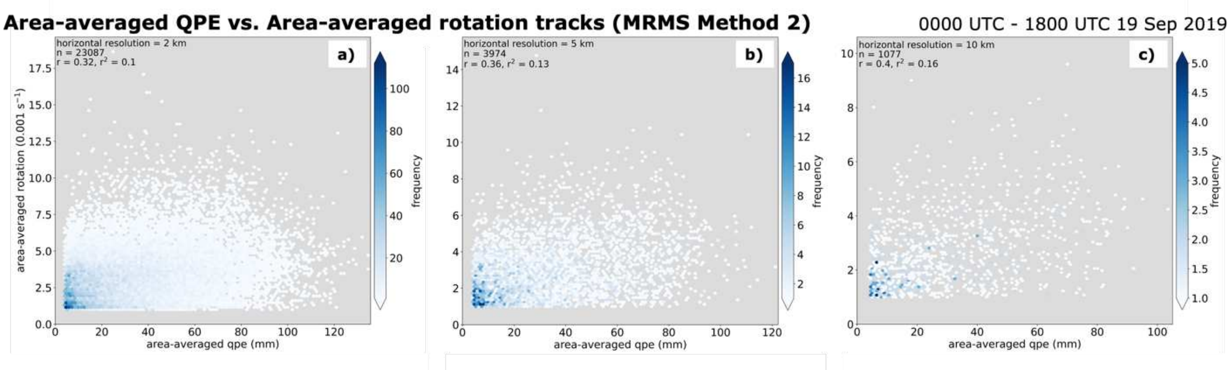

Figure 4.15: Hexbin plots of area-averaged Multi-Radar Multi-Sensor (MRMS) one-hour quantitative precipitation estimate (QPE) (mm) and area-averaged MRMS one-hour accumulated 0-2 km rotation tracks calculated from coarsened grids with horizontal resolutions of 2 km (a), 5 km (b), and 10 km (c) as described by MRMS Method 2. Only coarsened grid boxes that have an area-averaged one-hour QPE greater than 4 mm and an area-averaged one-hour accumulated rotation track greater than 0.001 s^{-1} are included. Note the differences in scale on the colorbars and axes.

The hexbin plots in Fig. 4.15 show the majority of the area-averaged values are centered in the lower left-hand corner of the plots. This makes sense given the method of only incorporating each grid point (which will predominantly be small values) into the area-averages once, meaning the majority of the QPE and rotation tracks will fall on the lower end of the spectrum, with large values of each being much more isolated. These smaller values are responsible for much of the strong positive correlation, as the data becomes less correlated as smaller values are removed (not shown). This is not surprising, as none of the plots show the absence of high QPE/low rotation and low QPE/high rotation that was prevalent in the plots associated with MRMS Method 1 (Fig. 4.13). Thus, this particular finding is not consistent with what is shown in Fig. 4.13, where there were very few boxes with strong rotation for low QPE values or vice versa. However, all averaging boxes used in MRMS Method 2 are all as small or smaller than the averaging boxes used with MRMS Method 1, which could also be why the plots in Fig. 4.15 have more spread compared to those in Fig. 4.13. Coarsening the grid further with MRMS Method 2 does not add much more value, as the resolution of the datasets becomes very low, and the number of averaging boxes to analyze are reduced significantly (not shown). Nonetheless, it does appear that in general, areas that had a higher area-averaged QPE tended to also have higher area-averaged rotation, suggesting that there is some positive relationship between low-level rotation and estimated rainfall accumulations.

4.4 Summary

This analysis utilized hourly MRMS local gauge bias-corrected QPE and hourly-accumulated MRMS 0-2 km rotation tracks to examine the spatial and temporal relationships between heavy rainfall and low-level storm-scale rotation in Tropical Storm Imelda. The MRMS QPE and MRMS rotation were overlaid across one-hour time steps from 0000 UTC to 1800 UTC on 19 September 2019, which was a period characterized by extreme rainfall rates and embedded rotation based on previous analyses of gauge precipitation and radar imagery.

Three analyses were conducted to assess the relationship between the MRMS QPE and MRMS rotation. The first method aimed to examine the spatial overlaps over time using both latitudinally-averaged and longitudinally-averaged Hovmöller diagrams. The second two techniques (MRMS Method 1 and MRMS Method 2) involved sampling the MRMS grid cells using two different approaches, then analyzing them over different horizontal areas by calculating area-averages and area-maximums. In all three cases, spatial-averaging methods needed to be applied because comparing individual overlapping MRMS QPE and MRMS rotation grid cells to one another would be too fine of a resolution (1 km and 0.5 km respectively) to study the relationship of rainfall and rotation on the meso-/storm-scales.

The Hovmöller diagrams suggest a consistent spatial and temporal overlap between the MRMS QPE and MRMS rotation during the 18-hour period. This finding was true both in a latitudinally-averaged and longitudinally-averaged sense. Persistent rotating features could be identified in multiple parts of the system, and the high MRMS QPE values were frequently located in very similar areas as high MRMS rotation values. These results also suggest that as rotation intensified, precipitation tended to increase during the 18-hour period of study, implying that there is a positive relationship between rotation in the low levels and rainfall at the surface.

The results of MRMS Method 1 and MRMS Method 2 indicate a positive correlation between area-averaged hourly MRMS QPE and area-averaged hourly MRMS rotation. In other words, locations that saw a larger amount of rotation in the low levels of the atmosphere also tended to see greater area-averaged accumulated rainfall.

With MRMS Method 1, there were few to no boxes that contained high area-averaged MRMS QPE and low area-averaged MRMS rotation, nor were there many boxes that contained high area-averaged rotation and low area-averaged MRMS QPE. This characteristic suggests that for this particular event, it was uncommon for strong embedded rotation to take place in locations receiving relatively small amounts of rainfall, nor was it likely that locations receiving large amounts of rainfall would see very little rotation in the low levels. As averaging area increased (i.e., the size of the boxes) using MRMS Method 1, the correlation became stronger, though this is likely due to the fact that area-averaged boxes became more similar to each other as more of the same grid points began to be included in the same boxes, which made the area averages more similar.

MRMS Method 2 also shows a positive relationship between these two sets of data, though the correlations are less strong than those found with MRMS Method 1. However, this difference may be partially due to the fact that area-averaging of the MRMS QPE and MRMS rotation occurred over areas as large or larger in MRMS Method 1, and overlaps between the averaging boxes were also permitted in that method. MRMS Method 2 did not show the similar absence of low rotation/high QPE and high rotation/low QPE in the area-averaging that was seen in the results of MRMS Method 1, which does cast some doubt over the relationship between rainfall and rotation in this particular analysis. Nonetheless, the majority of the evidence provided by the Hovmöller diagrams and MRMS Methods 1 and 2 largely support a positive spatiotemporal correlation between MRMS low-level rotation and MRMS accumulated rainfall.

Given the positive correlation between embedded rotation and rainfall rates that were found in the MRMS products, this result is consistent with previous studies that have established physical connections between these two processes via modelling (e.g., Nielsen and Schumacher 2018, 2020b). Further, these results agree with the results of Brauer et al. (2020), which showed that MRMS rotation tracks tended to be co-located with areas of enhanced rainfall accumulations and high precipitation efficiencies in LTC supercells. Lastly, the positive correlation and spatiotemporal overlap between embedded rotation and rainfall agrees with previously-examined observations that have shown a positive relationship between these two features in continental convective systems (Nielsen and Schumacher 2020a).

CHAPTER 5: LIMITATIONS, NEXT STEPS, CONCLUSION

5.1 Limitations

There are a few limitations with this study that should be addressed, beginning with the downsides of using only one case, Tropical Storm Imelda, in these analyses. Because this is a case study, sweeping generalizations about observations of embedded rotation and extreme rainfall in LTCs cannot be made. In particular, Tropical Storm Imelda was relatively messy given its weak, short-lived nature, and its most extreme rainfall occurred when the system had been reduced to remnants. This means that while the relationship between embedded rotation and rainfall rates shown here may translate to other LTC remnants, the relationship of these two mechanisms in LTCs with better-developed structures remain outside the scope of this work. Nonetheless, Imelda's transition from traditional weak TC structure to its remnants becoming a quasi-stationary MCS with extreme precipitation rates and embedded rotating features arguably make the system worthy of a case study at the least.

Shifting focus to the radar and rain gauge analysis presented in Chapter 3, one of the most obvious limitations is that the presence of rotation is determined subjectively rather than using an algorithm or some other automated classification scheme, meaning that the identified rotation could vary by individual interpretation. While this concern is valid, multiple steps were taken to ensure that the classification scheme was very conservative with identifying rotation images. Further, manual radar analysis is frequently relied on in the literature, not only for identifying mesoscale rotation (e.g., Nielsen and Schumacher 2020a), but also for classification of system types, such as with MCSs (e.g., Parker and Johnson 2000; Schumacher and Johnson 2005, 2006; Keene and Schumacher 2013), making this approach not unreasonable. Another potential limitation to this analysis is that the rotation classification scheme is binary—that is, radar velocity images are not categorized further based on the structure or magnitude of the embedded rotation. Because of this relatively simplistic approach, not much can be said about the relationship between the observed strength or structure of the rotation and the quantity of rain that was observed with this method. However, the methods did seek to only include rotation that was relatively strong, well-defined, and between storm- and meso-γ scale, which did inherently constrain the type and strength of the rotation that was identified.

One other key limitation that should be addressed with the radar and rain gauge analysis is the temporal variability between the paired radar images and the 5-minute rainfall observations. The method used here allowed there to be anywhere between 1 and 5 minutes of lag time from the radar image to the gauge observation. Because of this approach, some 5-minute observation periods may have begun several minutes before the time stamp of the radar image, while others may have occurred entirely after the radar image was captured. Further, some 5-minute observations were neglected entirely if they fell between certain radar timestamps (e.g., the 0225 UTC gauge observation would be neglected for radar scans occurring at 0218 UTC and 0226 UTC). Though these issue do complicate the comparisons that were drawn between the time-matched radar images and rainfall observations, this time resolution is an improvement from Nielsen and Schumacher (2020a), which paired observations of meso-γ scale rotation and rainfall observations on hourly time scales. Potential improvements to the method described here will be included in the subsection of this chapter that focuses on avenues for future work.

Lastly, there are a few limitations that need to be noted with regards to the MRMS analysis presented in Chapter 4. One concern with the results presented is autocorrelation, i.e., that the paired MRMS rotation and MRMS QPE values calculated from the averaging boxes are correlated with themselves over time. Autocorrelation is to be expected because consecutive time stamps are being evaluated, thus it is anticipated that the observations to be somewhat related over time. The evident spatial overlap shown among the rotation and QPE makes this issue somewhat less concerning. Nonetheless, this study only examines the relationship between two variables, and it is likely that there are confounding variables that were not explored here. An additional concern lies with the MRMS system itself, particularly in regard to the calculations of rainfall rates, which are used for the QPE products. At the time of Imelda, the MRMS QPE products relied on relatively simple "Z-R" relationships, which uses the radar reflectivity factor (or SHSR in the case of MRMS) (Z) to calculate rainfall rate (R). While the algorithm does adjust the Z-R relationship based on precipitation type (Zhang et al. 2016), recent work has found that these calculations tend to underestimate very heavy rainfall rates in some cases and overestimate it in others, which is why recent updates to the MRMS system have begun incorporating dual-pol variables in an effort to improve rain rate calculations (Zhang et al. 2020). Further, in the algorithm before the update, the maximum rain rate for tropical-stratiform mixed rain and convective rain was 147.4 mm h^{-1} and 103.8 mm h^{-1} respectively (Zhang et al. 2016). Though the maximum rain rate of 142.2 mm h^{-1} that was identified in the MRMS QPE for Imelda implies that the algorithm correctly identified the environment in at least some cases, many of the hourly gauge observations come very close to this value (Fig. 3.3), and misidentification of the rainfall type could clearly have significant limitations of the rainfall rate that is being calculated for the

QPE products. Thus, the shortcomings of radar-based QPE estimations are something that should be kept in consideration when digesting the results of this study.

5.2 Conclusion

This analysis explores observations of embedded rotation and heavy rainfall in LTCs through a case study of Tropical Storm Imelda. In order to further the understanding of the relationship of these mechanisms, this study had three objectives: 1) to identify the multiscale mechanisms that contributed to Imelda's excessive rainfall, 2) to explore the spatial and temporal relationship between embedded meso- to storm-scale rotation and the extreme rain rates that occurred during Imelda using observations, and 3) to identify the magnitude and significance of this relationship. The synoptic and mesoscale analysis presented in Chapter 2 revealed that extreme rainfall rates that occurred during Imelda resulted from a combination of several factors. Specifically, the co-location of high column-integrated moisture, moderate instability, mid-level positive vorticity advection, a LLJ, and converging winds impinging perpendicularly on the warm side of a mesoscale temperature gradient provided sufficient moisture, lift, instability, and rising motion to support the development of the heavy rainfall-producing system. The radar-rain gauge analysis in Chapter 3 revealed a statistically significant positive relationship between the presence of embedded rotation and 5-minute rainfall observations, showing that nearly two times as much total rainfall fell when there was rotation present compared to when there was no rotation present. Lastly, Chapter 4 showed a positive correlation between low-level rotation and rainfall rates using rotation tracks and QPE products from the Multi-Radar Multi-Sensor system. It additionally demonstrated that the heavy rainfall and embedded rotation tended to track together over time. Together, this evidence supports the claim that there is some correlation between embedded rotation and rainfall rates in LTC environments, and these findings can be translated into improved forecasting practices in multi-hazard situations. Specifically, it suggests that in LTC environments, convection with embedded mesovorticies should not only be monitored for their tornadic potential, but also for their localized flash flood threat, particularly when there is evidence of backbuilding or training.

5.3 Future Work

The work presented in Part I of this manuscript sparks ideas for several avenues for future research. One of the first paths would be to apply the MRMS methods shown in Chapter 4 to other recent LTC cases that have included flash flood-producing rainfall and associated tornadoes, including slow-moving systems like Imelda (e.g., Hurricane Florence (2018)) and systems that were faster-moving flash flood-producers but also produced a greater number of tornadoes (e.g., Isaias (2020), Ida (2021)). Expanding the cases in the MRMS analysis would 1) clarify the significance of the results found with Imelda and 2) determine if there is variability in the relationships shown between the heavy rainfall and embedded rotation among various "types" of LTCs. It would also be interesting to apply the rain gauge/radar analysis presented in Chapter 3 to other cases as well, though the lack of densely-populated rain gauge networks would hinder this possibility some. Nonetheless, if this test were to be repeated, applying some kind of weight to the rainfall observations to account for the variable time offset between the gauge and radar timestamps would be beneficial. Lastly, this study focuses solely on observations of heavy rainfall rates and embedded rotation in LTCs, but numerical modelling introduces an entirely new dimension to these results. There is ongoing collaboration with other researchers who have been focused on running such simulations in LTCs (including Imelda), and their results along with those from the observations used in this study will be compared.

PART II: EVOLVING EXPERIENCES OF GULF COAST RESIDENTS DURING HURRICANE HARVEY USING TWITTER

Previous chapters in this manuscript have demonstrated through observations that heavier rainfall may occur when there is embedded mesoscale rotation present, specifically in a landfalling tropical cyclone (LTC). Knowledge that these two processes are related is significant because both can lead to co-located, concurrent hazards at the surface: flooding and tornadoes. Understanding that relationships between precursors to these overlapping hazards exist is important from a forecasting perspective, as their occurrence can complicate the warning-issuing process by dividing meteorologists' attention and result in unintentional amplification of one threat over the other (Henderson et al. 2020), which can ultimately lead to failures in communication to end users.

Though it is necessary to make sense of the physical mechanisms that drive coincident tornadoes and flooding in LTCs because of the impacts on operational forecasting, it is also crucial to consider members of the general public that receive forecasts and information about these hazards, as they can experience impacts to themselves (mentally and/or physically) and their property. Numerous studies have shown that personal experience with significant meteorological events can shape the thoughts, perceptions, actions, and decision-making processes of those who have lived through them, all of which can then influence their behaviors in future disasters. Understanding how these behaviors and thoughts manifest is critical to improving communication by decision-makers and operational forecasters who wish to minimize loss of life and property.

In Part II of this thesis, the ways in which current experiences are informed by past events are explored. Specifically, the following chapters examine the ways in which past experience emerges and evolves across different stages of a weather-related disaster. The methods employed here examine these experiences through the lens of Twitter data collected from a 12-day period encompassing Hurricane Harvey, a significant LTC that impacted the western Gulf Coast in 2017. Geographically, this study focuses on tweets from users located in southeast Texas and southern Louisiana, all of whom expressed awareness of the multiple hazards (specifically tornadoes and flooding) that accompanied Harvey, as well as demonstrated knowledge of past meteorological events (primarily tropical cyclones, or TCs). By using knowledge of these past events as a proxy for experience, this work addresses the following two research questions:

> *Q1: How does experience emerge through the lens of the past event tweets during Hurricane Harvey?*
>
> *Q2: What are the different ways in which past events are discussed by users during the various stages of Hurricane Harvey?*

CHAPTER 6: BACKGROUND AND MOTIVATION

6.1 Experience with Past Weather Hazards

Experience has been studied in the context of numerous natural hazard-related events, from hurricanes, to floods, to tornadoes, to earthquakes. However, the definitions of what classifies as "experience" and the proxies used to characterize it have been broad. Historically, these definitions have drawn designations between direct and indirect experiences, which can be tangible and/or intangible. As Demuth (2018) writes in the context of weather and disaster-related experiences, a direct experience can be broadly classified as "one's own, unmediated participation in a threat and/or event", whereas an indirect experience is "mediated by reading, viewing, or hearing information… from others" (p. 1928). For a review of the different ways in which experience has been defined in weather-related studies, see Demuth (2018).

Direct experiences, which can be both tangible and intangible, have been explored on several occasions in the context of LTCs. Definitions of what qualifies as a direct experience with a LTC vary among studies, though some authors assert that in order for an experience to be direct, the person having a the experience must be located in an area affected by a LTC while it was occurring (e.g., Trumbo et al. 2011; Goldberg et al. 2020). Tangible direct experiences in LTC scenarios could include evacuating an area where a LTC was imminent, or experiencing some kind of personal damage or loss (e.g., Trumbo et al. 2011; Demuth et al. 2016; Rickard et al. 2017). Meanwhile, an intangible direct experience in the context of LTCs could include emotions that arise as a result of the storm, such as distress (Demuth et al. 2016). Tangible and intangible direct experiences are not necessarily mutually exclusive, though they can occur in tandem. In other words, intangible direct experiences can occur even when tangible experiences are not reported, though it is common for people to experience both types at the same time (Demuth et al. 2016).

Indirect experiences have also been studied in LTC settings. By definition, indirect experiences can only be intangible, since there is a mediating person or object that stands between the person having the experience and the event itself. Examples of indirect experiences that could be associated with LTCs could include knowing someone who was personally impacted by a LTC (e.g., Trumbo et al. 2011; Rickard et al. 2017) or developing emotions while watching LTC aftermath on television. The existence of indirect experiences further confirms that intangible experiences can occur in isolation from tangible experiences (Demuth et al. 2016).

One reason that past experiences with LTCs are important to make sense of is because they can provoke changes to future perceptions. For instance, perception of hurricane impacts tends to be higher among people who have had a past hurricane experience (e.g., Huang et al. 2012), as do risk perceptions (e.g., Demuth et al. 2016; Goldberg et al. 2020) and risk judgements (e.g., Rickard et al. 2017). Hurricane experience can also skew perceptions of LTC severity relative to other events of similar meteorological intensity. That is, when comparatively worse impacts are endured in one's own area from a particular storm, that event is perceived to be more intense, even if the same area is impacted by an event of similar strength (though sees fewer impacts) (Senkbeil and Schneider 2010). With knowledge of the Saffir-Simpson scale (the scale used to rate hurricane intensity based on wind speed) being limited in scope (e.g., Senkbeil and Schneider 2010; Knox et al. 2016), and with impacts of LTCs being highly variable across areas that are affected, people's past experiences with hurricane events may cause them to misjudge future events as a result.

Experience can also influence behaviors and actions. For instance, people with past hurricane experience may be more likely to take additional preventative action, such as having a hurricane evacuation kit prepared (Horney et al. 2008) or choose to evacuate (e.g., Brommer and Senkbeil 2010). However, more studies have found that the connections between experience and actions are not necessarily simple and straightforward. Specifically, beliefs and perceptions can serve as mediators or predictors between experience and behavior (see Fig. 6.1 for an example theoretical model). Demuth et al. (2016) showed that past experience with a hurricane can shape efficacy beliefs and perceived risk, which when elevated, tend to have a positive effect on evacuation intentions (Fig. 6.1). Even among

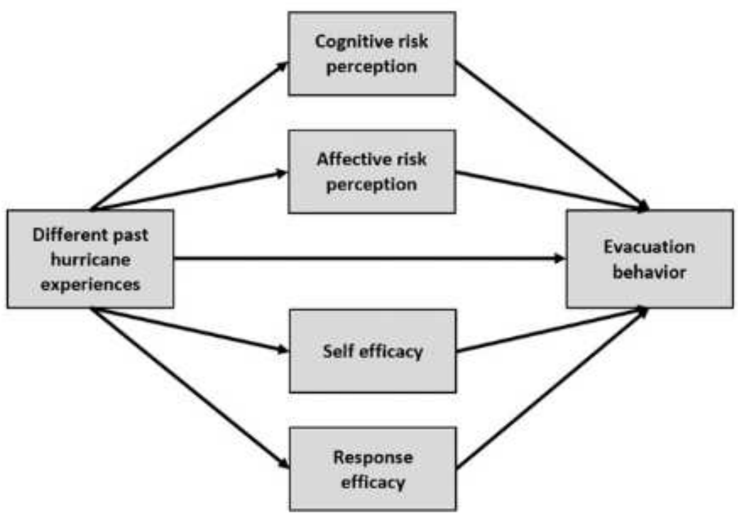

Figure 6.1: From Fig. 1 in Demuth et al. (2016), showing a theoretical model of hurricane experience and evacuation behavior with mediating variables (i.e. perception and efficacy).

meteorologists, past experience can play a role in their own risk perceptions of certain hazards, which can unintentionally lead to certain hazards being focused on over others during forecasting operations (Henderson et al. 2020). It has also been shown that experience can be coupled with other factors, such as confidence in past decisions, to predict future actions (Goldberg et al. 2020). These studies all demonstrate that experience cannot necessarily be examined in isolation, but rather, the interplay of thoughts, perceptions, and belief systems must all be considered in tandem with experience. Yet, these elements of experience remain difficult to capture, analyze and measure.

Many of the experience-related studies described above share a methodological commonality, which is that they were conducted using either surveying (e.g., Huang et al. 2012; Demuth et al. 2016; Rickard et al. 2017; Demuth 2018; Goldberg et al. 2020) or interviewing techniques (e.g., Horney et al. 2008; Henderson et al. 2020). Because of this choices in methods, most studies have examined experience in the context of weather-related events after the weather-related event(s) took place. Very little has been done to assess the ways in which past experiences emerge in real-time while the weather-related disaster is taking place. This work attempts to address this gap in the literature by examining experience as it emerges during a real-time weather event by using archived tweets from Twitter.

6.2 Use of Twitter Data in Weather Hazards Research

The social media platform Twitter presents an opportunity to examine statements, behaviors, and perceptions of users as they are captured online in real-time during disasters, as opposed to after the event is over. Unlike other social media sites, each qualitative data point (i.e., a tweet) on Twitter must be succinct—that is, no longer than 280 characters[6] —which helps make the data somewhat more digestible. Data on the site is also easily accessible. Through application programing interfaces, or APIs, large volumes of tweets can be queried based on specific keywords or hashtags over designated

[6] Twitter increased the maximum character count permitted in tweets from 140 to 280 in late 2017.

periods of time, allowing groups of interest to be identified. Twitter users can also be identified based on geographic location, though this approach is limited by the fact that relatively few tweets are geotagged (approximately 1-2%) and those that are frequently tagged are riddled with inaccuracies, since location can be manually selected by the user (Palen and Anderson 2016). Sophisticated techniques have developed tools to sift through tweets more effectively than traditional APIs to specifically target disaster-related tweets that can be used to help focus recovery efforts (e.g., Ashktorab et al. 2014).

The ways in which disasters are discussed on social media platforms, including Twitter, is typically dependent on the type of disaster that is occurring (Vieweg et al. 2010; Palen and Hughes 2018). In LTC-related disasters specifically, tweets have been shown to cover a wide variety of topics and themes. For example, Anderson et al. (2016) and Demuth et al. (2018) found that some common risk perception themes among tweets sent during Hurricane Sandy included sharing of environmental cues, noting preparatory or protective actions, and circulating of coping mechanisms. Other studies have shown that users display a variety of emotions through their tweets during LTCs, ranging from negative affectivity (e.g., fear, worry) to use of humor (Spence et al. 2015; Anderson et al. 2016; Knox et al. 2016; Demuth et al. 2018). Other uses of the social media platform include memorializing victims and coordinating relief efforts in the aftermath of LTCs (Takahashi et al. 2015), and discussing evacuation information ahead of them (Demuth et al. 2018; Xu et al. 2019). Using Twitter to disseminate information to at-risk individuals before and after a hurricane serves a meaningful purpose, though misinformation and irrelevant or distracting discourse can easily drown out tweets containing pertinent data (Knox et al. 2016).

The characteristics of the information shared on Twitter during LTC events can also be time-dependent. For instance, Kogan and Palen (2018) found that during the height of Hurricane Sandy's impacts, Twitter users interacted with an above average number of users and tended to have longer, slower-paced conversations compared to other periods of the event. On the contrary, other studies have suggested that tweet activity peaks at the height of the event, which for LTCs tends to be centered around the time when landfall occurs (Anderson et al. 2016; Morss et al. 2017; Xu et al. 2019).

The subject matter of information that is shared throughout a natural disaster can also change as the event progresses, and there are various ways to monitor such temporal trends. One way to examine changes in tweet content over time is through examining how themes evolve among individual users (e.g., Morss et al. 2017; Demuth et al. 2018). As an example, Fig. 6.2, which comes from Fig. 5 in Morss et al. (2017) shows the temporal evolution of tweets by an individual user tweeting from Far Rockaway, New York during Hurricane Sandy. This graphic shows that even when only one user is examined, the type of information being discussed on social media can vary throughout the course of a disaster.

Recent studies have also examined the use and limitations of Twitter in the context of Hurricane Harvey specifically, which is the target of this study as well. One study by Vera-Burgos and Griffin Padgett (2020) examined tweets sent by a high-profile user, the mayor of Houston, during the event, finding that his account was used for purposes such as to communicate with key partners and encourage unity among local residents. Residents of the impacted areas also used the social media platform for communication purposes, such as to assist with rescue efforts for people stranded by the

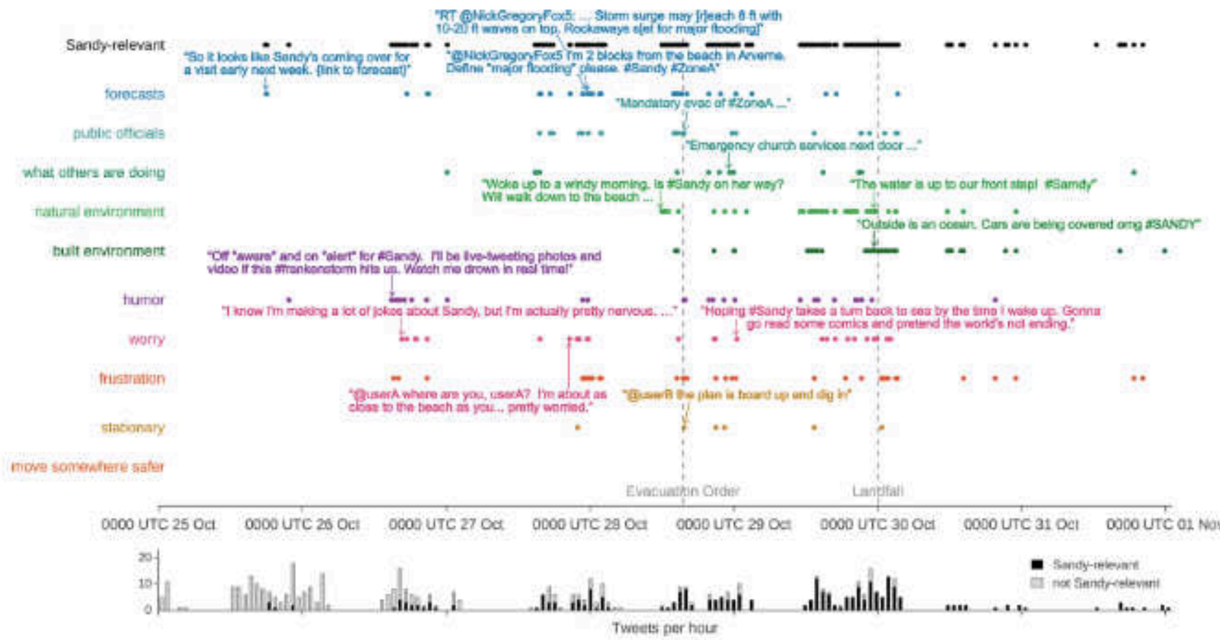

Figure 6.2: From Fig. 5 in Morss et al. (2017), which shows a graphical depiction of a tweet stream from a user tweeting from Far Rockaway, New York during Hurricane Sandy. The bar plot on the bottom shows hourly tweets (both Sandy-related and non-Sandy-related) over time. Sandy-related tweets over time are also shown as black dots along the top of the plot. Colored dots correspond to Sandy-related tweets over time that correspond with a particular theme, which are listed on the left in corresponding colors. Some tweets of interest are included and color-coded by theme. Time of the New York City evacuation order and Sandy's landfall are included as vertical dashed lines.

rising flood waters (Mihunov et al. 2020). While Twitter did prove to be helpful with sharing information and coordinating aid, the site was not equally accessible by all western Gulf Coast residents during Harvey. Studies found that while the disaster was taking place, the website was used disproportionately more often by users who were not particularly geographically vulnerable (Zou et al. 2019) and were of higher socioeconomic status (Mihunov et al. 2020). This work alludes to the broader issue of the "digital divide" among individuals who are more socially, economically, and geographically vulnerable, and highlights the benefits of specifically targeting such users in disaster studies involving Twitter data (Anderson et al. 2016; Demuth et al. 2018) who would otherwise be lost within the large datasets.

Other methods have employed models to separate the event into various stages or periods, which can assist with studying themes over time among tweets authored by many users at once. One of these models, known as the Fink crisis model (Fink 1986), has been applied in several disaster studies utilizing Twitter data, including ones focused on LTCs (Spence et al. 2015; Xu et al. 2019). In short, the model breaks crises into four stages: prodromal, acute, chronic, and resolution (Fink 1986). The prodromal stage represents the period before the crisis. It is followed by the acute stage, which is the crisis itself, beginning with a "triggering" event. The chronic stage comes after, and it encapsulates the period when the peak of the crisis has passed, though the crisis still continues as the aftermath must be dealt with. The final stage, resolution, is marked by the end of the crisis. Applying the Frink crisis model to studies of tweets during LTCs shows that preparatory actions (Xu et al. 2019) and information related to the status of the meteorological phenomenon itself (Spence et al. 2015) tend to be present in the earlier stages of LTC events. Meanwhile, dialogue surrounding impacts and damage become more popular topics in the middle of the event (Xu et al. 2019) followed by recovery and relief information, affectivity, and political debate in the later stages of the event (Spence et al. 2015; Xu et al. 2019).

A few studies that have analyzed tweets from Twitter have noted that some people do indeed refer to past LTC events while they are being impacted by another LTC (e.g., Anderson et al. 2016; Knox et al. 2016; Xu et al. 2019). However, these conversations have not been studied in-depth, and it is hypothesized that there is rich information about experience that can be extrapolated from tweets that reference past events. In this study, the Fink crisis model is used to temporally analyze the tweets as other LTC-related studies have done before (e.g., Spence et al. 2015; Xu et al. 2019), but it is used to specifically examine experience in real-time as it emerges across different stages of a hazard (i.e., Harvey). Then, experience is assessed in more specific ways, first in how it emerges in individual past events, and then how it evolves among the individual users themselves. Therefore, this analysis provides a new contributions to the existing literature in three ways: 1) by investigating past events as a proxy for experience, 2) by exploring past experience as it unfolds in real-time rather than as it is recalled post-disaster, and 3) by considering the individual's purpose for referencing a past event during a real-time event.

The remainder of Part II of this thesis proceeds as follows. Chapter 7 includes a meteorological overview of Hurricane Harvey as well as the methods for Twitter user selection and analysis and the research questions of this study. Chapter 8 presents the results and discussion. Chapter 9 offers a summary of Part II, limitations of this analysis, and avenues for future work.

CHAPTER 7: EVENT OVERVIEW AND METHODS

7.1 Site: Hurricane Harvey

Hurricane Harvey began as a disturbance in the waters off the west coast of Africa on 12 August 2017 as a broad area of convection (Blake and Zelinsky 2017). The system tracked westward and eventually organized into a named tropical storm by 1800 UTC on 17 August a few hundred kilometers east of the Lesser Antilles. National Hurricane Center (NHC) track data (Landsea and Franklin 2013) shows that Harvey made landfall in Barbados, then St. Vincent as a tropical storm on 18 August, before weakening in a tropical wave about one day later. The remnants of Harvey continued westward across the Caribbean and through the Yucatan Peninsula before entering the Bay of Campeche around 1200 UTC 22 August. The tropical wave reformed into a tropical storm by 1800 UTC 23 August, then intensified into a hurricane 24 hours later (Fig. 7.1). Harvey drifted northward, then northwestward as it underwent rapid intensification, becoming a 105 knot Category 3 hurricane by 1800 UTC 25 August. The TC continued intensifying, becoming a Category 4 hurricane before it made landfall near Rockport, Texas on San José Island around 0300 UTC 26 August, then the Texas mainland three hours later.

Harvey made landfall between two upper-level troughs to its west and east, as well as south of a shortwave ridge to its north (Fig. 7.2a). This pattern set up very weak flow in the upper levels over the southeast Texas region, and while the trough-ridge pattern remained progressive, the stronger flow remained north of southeast Texas, which supported a prolonged period of weak winds aloft over the region (Fig. 7.2b). Weak steering currents are typical in LTCs that produce particularly heavy rainfall

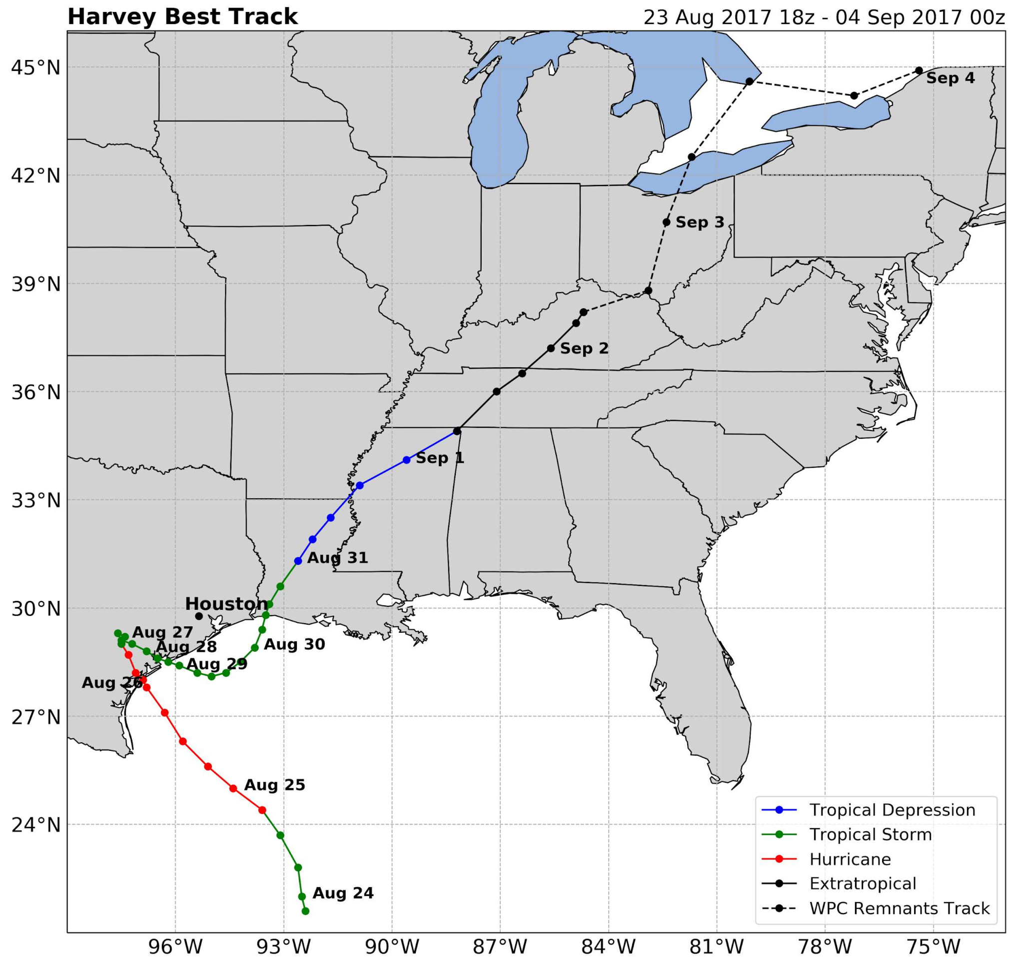

Figure 7.1: Hurricane Harvey track from the time at which it became a renamed tropical storm to its dissipation using National Hurricane Center HURDAT2 best track data (1800 UTC 23 August to 1200 UTC 2 September) (Landsea and Franklin 2013) and Weather Prediction Center surface analysis data (1200 UTC 2 September to 0000 UTC 4 September). Annotated dates are shown at 0000 UTC for each day. Additional points along the track are generally shown every six hours, with additional points being included if there was a change in intensity reported during a different hour.

because they allow deep, tropical moisture to remain over a given area for an extended period of time. Thus, this feature contributed to Harvey's excessive rainfall, but in addition, forcing for ascent associated with a baroclinic zone (i.e., a stationary front) was co-located with the tropical moisture (Fig. 7.3), providing a lifting mechanism to support heavy rainfall that is not often found in even the top rain producing TCs (Galarneau and Zeng 2020). This feature is clear in the precipitable water fields, which show little change in moisture between the time just before Harvey made landfall (Fig. 7.2c) and nearly 48 hours after being inland (Fig. 7.2d).

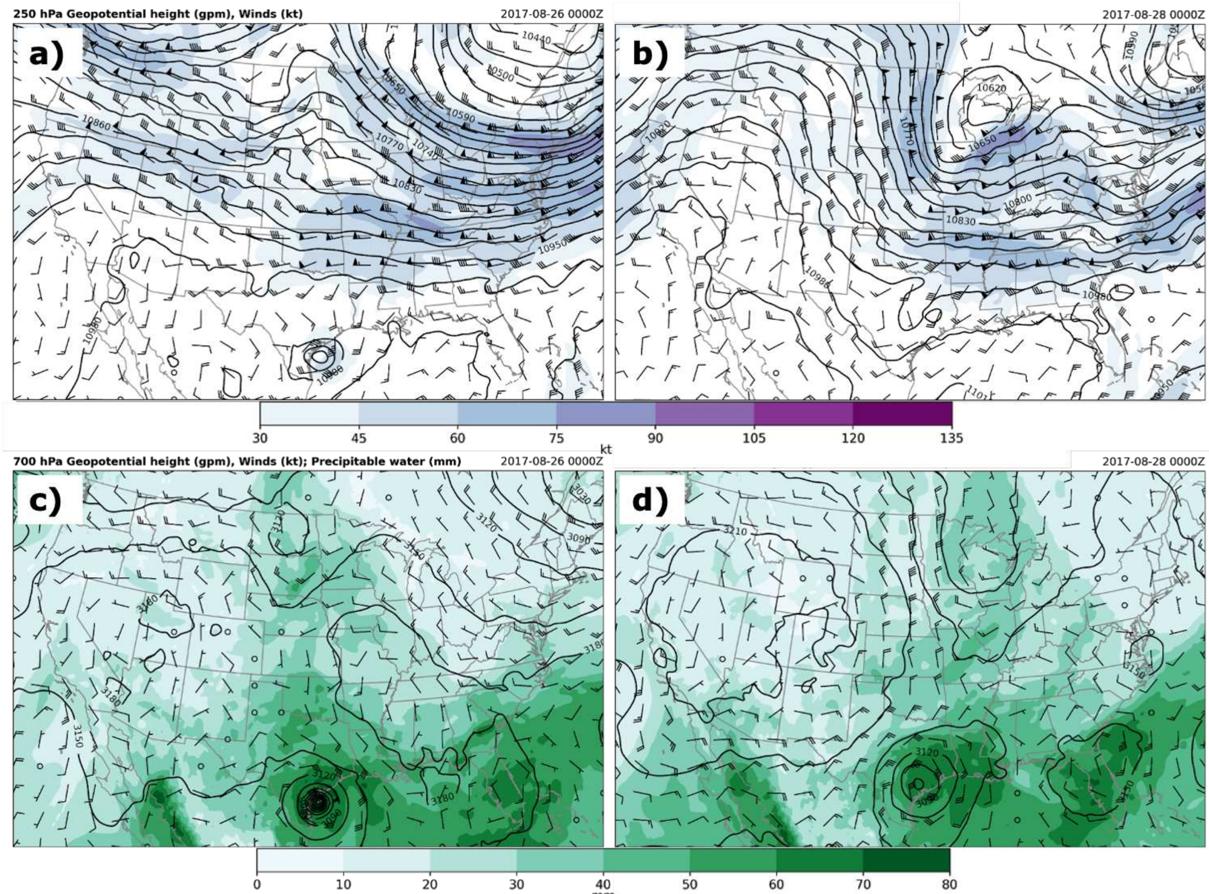

Figure 7.2: 13-km Rapid Refresh (RAP) analysis showing 250 hPa heights and 250 hPa winds (30+kt shaded) on 26 August 2017 at 0000 UTC (a) and 28 August 2017 at 0000 UTC (b) as well as 700 hPa heights, 700 hPa winds, and column-integrated precipitable water on 26 August 2017 at 0000 UTC (c) and 28 August 2017 at 0000 UTC (d).

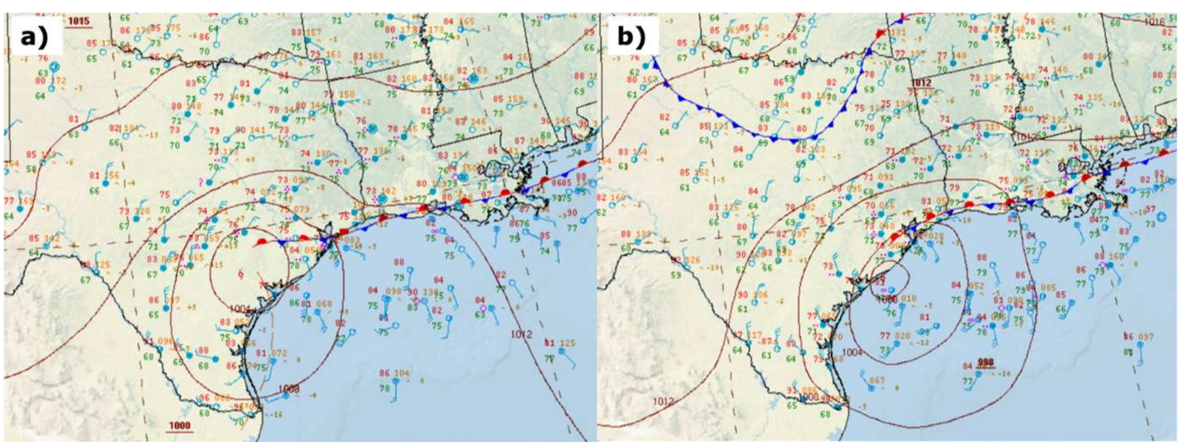

Figure 7.3: Weather Prediction Center surface analysis showing the location of Harvey and the stationary front at 1800 UTC 27 August (a) and 1800 UTC 28 August (b).

Slow storm motion, rich and prolonged moisture availability, and localized forcing all contributed to Harvey's historic rainfall, making many other flood-producing southeast Texas rainfall events appear insignificant in comparison (Fig. 7.4). Rainfall totals in excess of 500 mm occurred over a broad area and led to widespread flooding across southeast Texas and southern Louisiana (Fig. 7.5b). Maximum storm total precipitation in excess of 1500 mm set numerous all-time records, including one for wettest recorded TC to impact the CONUS. In addition to the excessive rainfall, Harvey's category 4 winds led to extensive damage in the Corpus Christi area, and it also spawned 52 confirmed tornadoes from Texas to Tennessee. Harvey ultimately left over 30,000 people displaced from their residences, left 89 dead, and cost an estimated $133.8 billion USD in damages (NOAA National Centers for Environmental Information 2021b).

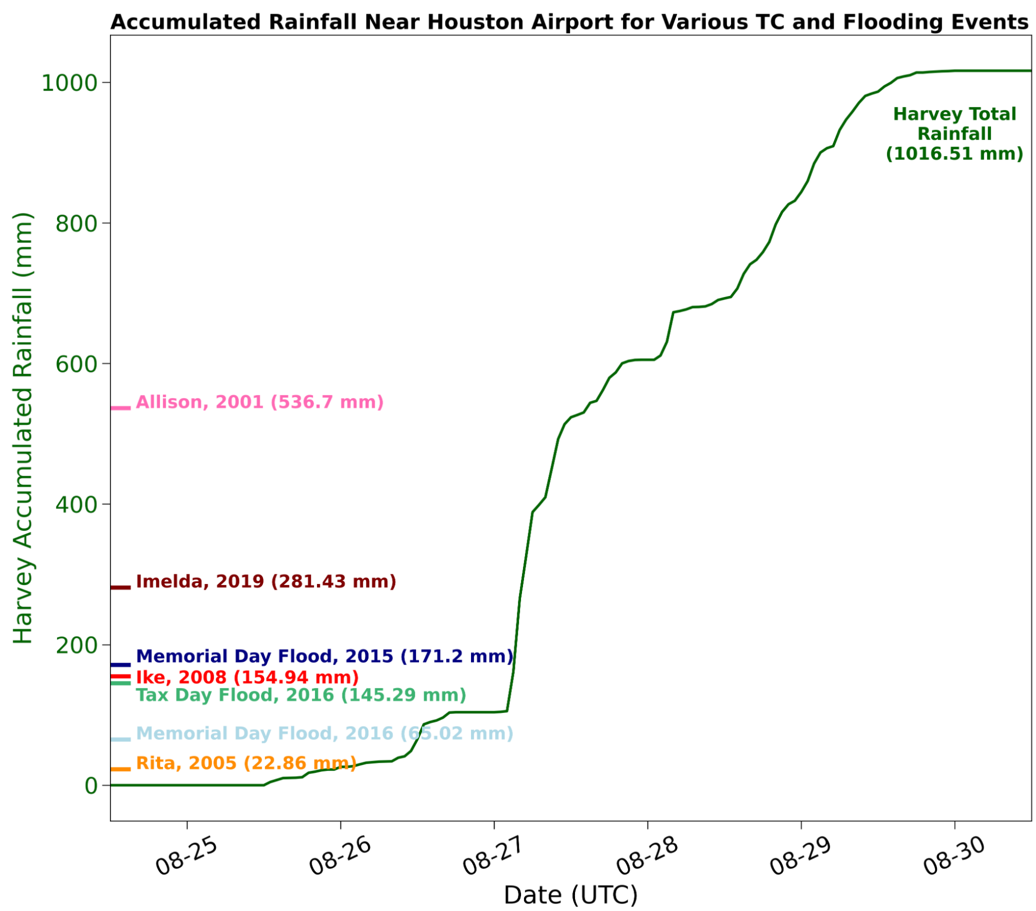

Figure 7.4: Accumulated rainfall during Hurricane Harvey, using an average of hourly readings from 4 Harris County Flood Warning System rain gauge stations located near the William P. Hobby airport in Houston. Also shown are various TC and non-TC flooding events that have impacted the Houston area, as well as their storm total rainfall accumulations according to the same 4 gauges. Note that these are not the event-maximum rainfall totals.

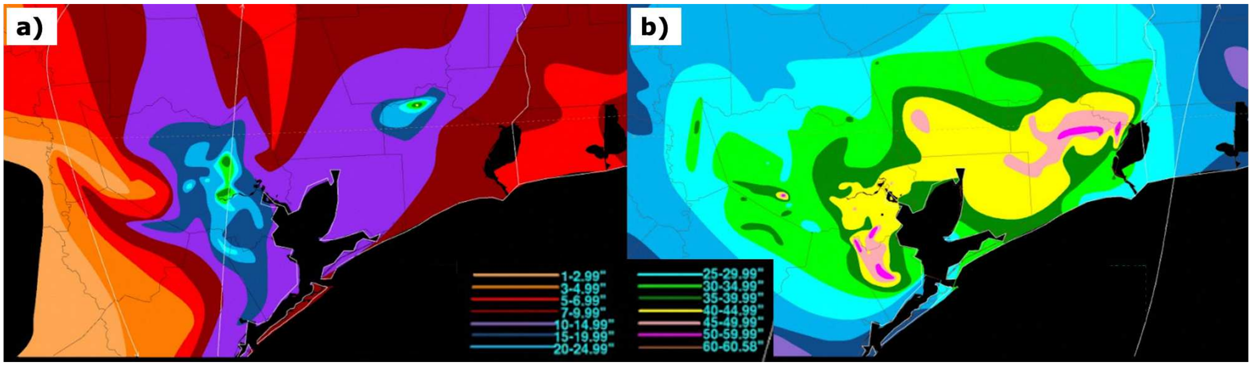

Figure 7.5: Rainfall totals (inches) over southeast Texas for Tropical Storm Allison (2001) (a) and Hurricane Harvey (2017) (b). Image from National Hurricane Center Tropical Cyclone Report on Hurricane Harvey.

7.2 Data Collection Methods

In order to use past events as a proxy for experience during Hurricane Harvey, several rounds of both automated and manual data collection and classification were required to produce a relevant, manageable database of "past event tweets". As will be described in more detail in the methods below, the users that were ultimately collected share the following characteristics:

1) Located in or evacuated from southeast Texas or southern Louisiana, where Harvey made landfall
2) Members of the general public, who were seeking information and advice about the storm
3) Awareness of and experience with tornadoes and flooding associated with Harvey
4) Knowledge of past meteorological events involving TCs and/or their hazards

Those methods, in addition to the methods used to analyze the data, are described in the following subsections. A summary of the methodological steps described in the next four sections can be found in Fig. 7.6.

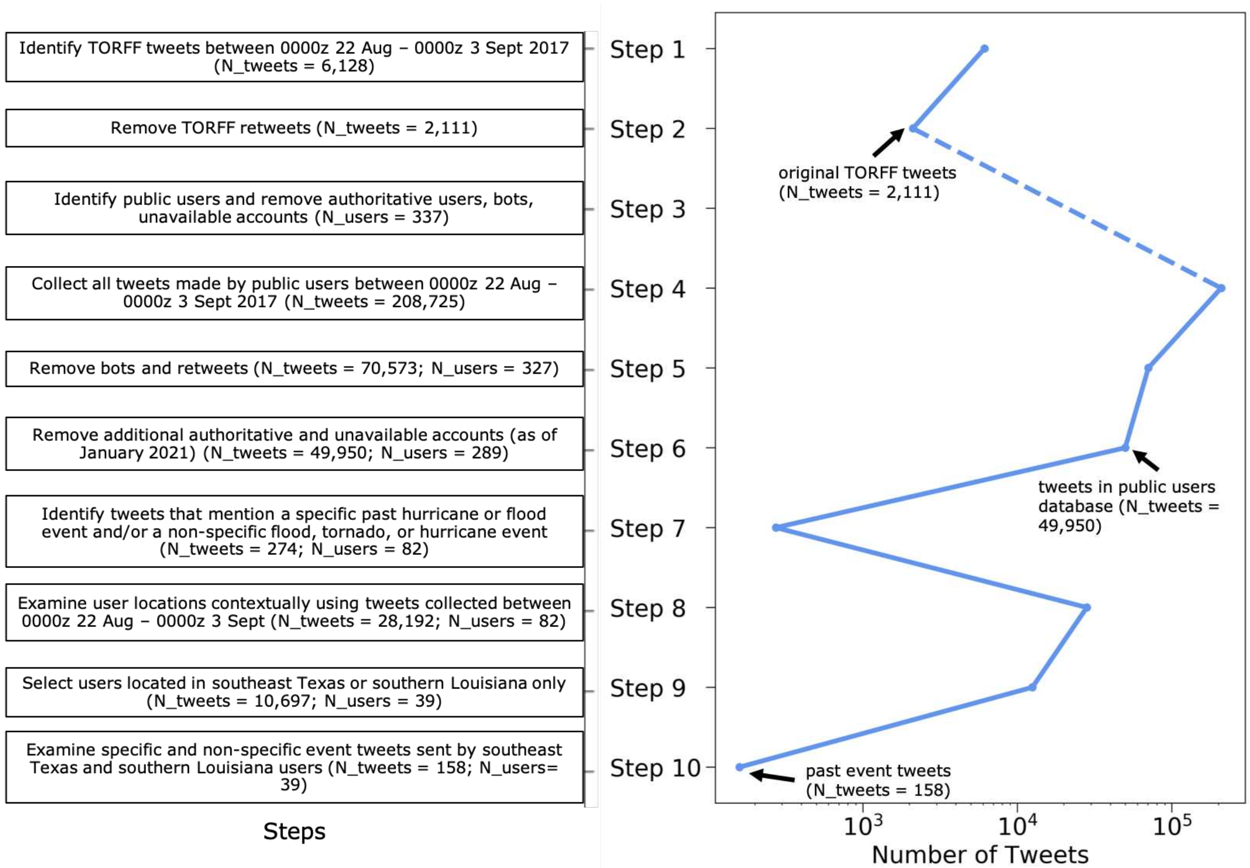

Figure 7.6: Summary of steps for selecting users and tweets (left) and line plot showing the number of tweets corresponding to each step (right). Interpolated data where the number of tweets was not determined is shown as a dashed line. N_tweets and N_users refer to the number of tweets and number of users corresponding to each step, respectively, where data is available.

7.2.1 Sampling Strategies

7.2.1.1 People Tweeting about Tornados and Flash Floods (TORFFs)

In order to connect this work to the broad theme of tornadoes and flash flooding as overlapping hazards, the initial data collection aimed to identify users who had experienced both of these phenomena. In an effort to achieve this goal, a Twitter API was used by a team of previous researchers to identify tweets made between 0000 UTC 22 August to 0000 UTC 3 September 2017 that featured at least one tornado-related word and at least one flood-related (from rain or from surge) word (Table 7.1). The time frame begins a couple days before Harvey was re-upgraded to tropical storm status (Fig. 7.1) and ends with its dissipation into a remnant low pressure system over the Ohio River Valley. These tweets will be referred to hereafter as tornado and flash flood, or "TORFF", tweets. This terminology offers an expansion on the meteorologically defined "TORFF events" described by Nielsen et al. (2015). In their paper, the term a "TORFF event" encompasses both a "TORFF warning" (co-located tornado warning and flash flood warning that occur within 30 minutes of each other) and a "verified TORFF" (a recorded tornado path and flash flood local storm report that occur within 50 kilometers and 3 hours of each other) (Nielsen et al. 2015). A total of 6,128 TORFF tweets were identified using the aforementioned search criteria across the 12-day collection timeframe (Fig. 7.6, Step 1). Given that retweets (i.e., the sharing of an original tweet created by someone else) do not capture a user's original content, these tweets were removed by the researcher team, leaving a total of 2,111 original, unique TORFF tweets.

Table 7.1: Search criteria used to identify TORFF tweets between 0000 UTC 22 August and 0000 UTC 3 September 2017.

Hazard Type	**Key Words**
Tornado	tornado #tornado \funnel cloud\ funnelcloud
Flood	flood \flash flood\ flashflood \storm surge\ stormsurge

7.2.1.2 Manual Classification of Public Users

Previous disaster-oriented research has demonstrated the value of distinguishing between different types of users on social media. For instance, Takahashi et al. (2015) showed that celebrities, government officials, the media, and laypeople used Twitter for different purposes before, during, and after Typhoon Haiyan impacted the Philippines. For this study, profiles of users who created each of the TORFF tweets were scanned and categorized by a previous group of researchers into 3 different types of users: public, authoritative, and bots/unavailable. Public users represent profiles that do not demonstrate professional or in-depth knowledge of meteorology or weather forecasting, nor do they present themselves as a member of the media or a government authority. Typically, their accounts were not dedicated to sharing Harvey-related weather information, but rather focused on their own thoughts and experiences as they evolved during the event, including seeking information. This contrasts with authoritative users, which include professional meteorologists (broadcast, public, and private), storm chasers, weather enthusiasts, news outlets, journalists, and government agencies. These accounts focus primarily on disseminating Harvey-related information to other Twitter users throughout the event, rather than amplifying their own personal experiences. The third category of users includes accounts that had been deleted, suspended, or unavailable (i.e., had "gone private" or made their tweets "protected"), as well as accounts that appeared to be "bots". Bots are classified here as accounts that were primarily sharing links, often to news articles, with no apparent personal commentary or varied syntax, and they typically tweet automatically. 337 users that had issued TORFF tweets were classified as public users, and additional analysis stemmed from this subset of users.

7.2.1.3 API Query of Contextual Tweet Streams

The goal of this step was an attempt to develop a richer picture of the content that the 337 public users shared on Twitter throughout the lifecycle of Hurricane Harvey. To do so, in-depth summaries or "narratives" were composed for each user along with a team of three other researchers by collecting and analyzing all tweets that were sent by the users over the 12-day period (Bica et al. 2021; Palen and Anderson 2016). These "contextual tweet streams" (Bica et al. 2021; Palen and Anderson 2016), were then organized into a spreadsheet by a previous group of researchers for a total of 208,725 tweets during the 12-day period (Fig. 7.6, Step 4). Again, all retweets were excluded since they do not provide original content by the users. During additional refinement of these categories, authoritative accounts, bots, and unavailable users were again removed. At the time that the remainder of the database assembly was complete (i.e., January 2021), there were 289 public users who posted 49,950 total original tweets between 0000 UTC 22 August and 0000 UTC 3 September 2017 (Fig. 7.6, Step 6).

7.2.2 Analysis Strategies

7.2.2.1 Identifying Past Events

The remaining methods attempt to capture mentions of past events related to LTC events and their associated hazards among the public users described above. The database of the 289 remaining users was mined using a variety of 66 search terms (Table 7.2). The first step in this process involved searching the database for mentions of any retired TCs that occurred during any Atlantic hurricane season between 2000-2017[7]. This range of dates was selected in order to capture references to all Atlantic TCs in the 21st century that were damaging enough to be deemed worthy of retirement, with the idea being that such events would be most salient in the minds of the majority of users given their

[7] Only retired Atlantic TCs that occurred before Harvey in 2017 were included in the search.

Table 7.2: Alphabetized search terms for querying the Twitter database for mentions of specific and non-specific past hurricane, tornado, and flooding events.

Search Terms		
“alica”	“hugo”	“lili”
“alicia”	“humberto”	“lilly”
“alisha”	“hurricaneike”	“lily”
“alison”	“hurricaneotto”	“matthew”
“allison”	“hurricanes”	“memorial”
“andrew”	“ ike”	“michele”
“been through”	“igor”	“michelle”
“bill”	“ingrid”	“noel”
“carla”	“irene”	“ondoy”
“catrina”	“iris”	“opal”
“charley”	“isabel”	“ otto”
“charly”	“isidore”	“otto ”
“cindy”	“ivan”	“rita ”
“dean”	“jeanne”	“paloma”
“dennis”	“joaquin”	“sandi”
“erika”	“juan”	“sandy”
“fabian”	“kartina”	“ stan ”
“felix”	“katarina”	“tax day”
“frances”	“katirna”	“taxday”
“gone through”	“katrin ”	“tomas”
“gustauv”	“katrina”	“wilma”
“gustav”	“keith”	“yolanda”

significant impacts. Furthermore, the Texas and Louisiana coasts (i.e., the region primarily impacted by Harvey), saw landfalls from numerous retired systems during the earlier half of this period (Allison (2001), Isidore (2002), Lili (2002), Ivan (2004), Katrina (2005), Rita (2005), Gustav (2008), and Ike (2008) (NOAA National Hurricane Center; NOAA National Ocean Service 2021). The choice to focus only on 21st century events was made because prior to Allison in 2001, Louisiana had not seen a retired LTC since Andrew (1992), and Texas had not seen a landfall from a retired TC since Hurricane Alicia (1983), marking a significant amount of time over which the region impacted by Harvey did not see a LTC worthy of retirement. Further support for this decision comes from the population of Twitter users, who tend to be young relative to overall population demographics (e.g., Sloan et al. 2015; Wojcik and Hughes 2019). In the United States specifically, 73% of Twitter adult users were between 18-49, whereas that same age group only makes up approximately 54% of the adult population (Wojcik and Hughes 2019). Thus, it would be reasonable to anticipate that the sample of users here would also be younger and therefore less likely to recall memorable LTCs that took place several decades ago. However, inductive analysis of the tweets revealed references to other systems, including non-retired TCs and TCs that occurred before the year 2000. Thus, when a new TC that had not been previously searched for was found, the entire database was re-queried for that system. For TCs with more complicated spellings, variations in spelling were used to capture typos and misspellings (e.g., Allison vs. Alison), a step that has shown to be valuable in previous hurricane research involving Twitter data (Knox et al. 2016).

Outside of specific named TC events, other recent, non-TC-related flood events that impacted the southeast Texas region were identified upon inductive analysis of the database. These events included the Memorial Day floods (occurring both in 2015 and 2016), as well as the Tax Day flooding event (2016). Given that inland flooding due to heavy rain was one of the most devastating hazards associated with Harvey, the database was queried for mentions of these systems as well.

In addition to these specific events, a few additional search terms were included upon inductive analysis in order to expand the number of tweets included in the analysis. For instance, the database was mined for phrases such as "gone through [a non-specific weather-related event]" and "been through [a non-specific weather-related event]". The intent behind including these search terms was to identify tweets that implied that the user had experienced a non-specific (or "unnamed") past weather event. The overarching term "hurricanes" was also searched for in an effort to find users that mentioned experience with non-specific past TC events. Lastly, inductive analysis of the user contextual streams revealed a few more tweets referencing past TCs and/or their accompanying hazards[8], so those tweets were included as well.

When combined, these initial search criteria yielded a list of 274 tweets from 82 active (i.e., not deleted, suspended, or private) users as of January 2021 (Fig. 7.6, Step 7). Tweets identified through the various searches described above will hereafter be referred to as "past event tweets".

7.2.2.2 Refining Location and Identifying Final Group of Users

Given that this study seeks to understand the role of past experiences as users experience in real-time, it is crucial that the users that are being analyzed are, in fact, experiencing the event. In order to do this, a definition for what constitutes as "experience" must be provided for the study. As was stated in the literature review, one way that experience (specifically, direct experience) is defined in LTC events is that the person being studied must have been located in the area being affected by the LTC (e.g., Trumbo et al. 2011; Goldberg et al. 2020). When experience is defined in this way, it generally implies that the person is experiencing direct impacts from the event to themselves and/or their property because they are local to where it is occurring. Refining the dataset to focus on users who are tweeting from the location where the disaster is unfolding rather than from afar is a common step that is taken in disaster research involving Twitter data (e.g., Vieweg et al. 2010; Ashktorab et al. 2014; Takahashi et al. 2015; Knox et al. 2016; Anderson et al. 2016; Demuth et al. 2018).

[8] This method was applicable for only two users.

In order to identify the user locations, the locations that were "affected by Harvey" need to be defined. The focus area extends as far west as Austin, Texas, as far south as Corpus Christi, Texas, as far east as New Orleans, Louisiana, and as far north as a line running between College Station, Texas and Alexandria, Louisiana (Fig. 7.7). In short, the domain includes the area where the hurricane made its three contiguous United States (CONUS) landfalls. Although there were areas impacted by Harvey and its multiple hazards outside of this area, including by the remnants of system (e.g., Mississippi, Tennessee, Kentucky), these locations were excluded, as the impacts to those areas could be characterized as being less severe (in terms of number of warnings, rainfall accumulation, and ambient wind speeds, for instance) and on a much shorter time scale due to the system's acceleration after it made its final landfall (Fig. 7.1).

Figure 7.7: As in Fig. 7.1, but zoomed in to southeast Texas, southern Louisiana, and southern Mississippi. Shaded light blue area shows the approximate domain where Twitter users analyzed for this study must be located.

For the final analysis, the user must have either 1) been located in (either permanently or temporarily) the area of study or 2) had recently evacuated but was a permanent resident of the study area. Although Twitter allows its users to list a location in their biography, it is impossible to determine whether a person's listed location is accurate or current. Further, the database did not include any additional geolocation information, meaning an alternative approach needed to be taken to determine user locations.

To determine location, the detailed narratives that were composed for each user from the contextual streams were analyzed for contextual evidence that implied a location, with locations listed on profiles only being used to add confidence to the location assessment. Examples of location-related contextual evidence include self-identifying location in a tweet, sharing a photo that reveals a current location (e.g., a radar image), reporting a direct encounter with Harvey's impacts (e.g., photo of flooding that the user takes themselves), or describing preparatory actions ahead of the LTC. In most cases, multiple forms of contextual evidence could be identified among users, and the tweets that implied a location typically matched the self-reported biographical locations.

As of June 2021, 39 of the 82 public users were identified as being located in southeast Texas or southern Louisiana (Fig 7.6, Step 9). It is this group of users and their past event tweets (158 of them) that are the focus of the analysis.

7.2.2.3 Analyzing the Tweets

To review, the final set of users that was collected using the methods above share the following characteristics:

1) Located in or evacuated from southeast Texas or southern Louisiana, where Harvey made landfall
2) Members of the general public, who were seeking information and advice about the storm

3) Awareness of and experience with tornadoes and flooding associated with Harvey
4) Knowledge of past meteorological events involving TCs and/or their hazards

For all parts of the analysis, each of the past event tweets shared by the 39 users in the southeast Texas and southern Louisiana regions were examined for context and purpose. Every tweet was studied in isolation unless it was part of a thread or conversation with another user, in which ambient context was then taken into account. Common themes were identified among the past event tweets. Analyses are conducted on three different "scales", beginning with the broadest/most generalized, which is a temporal analysis that is organized by stages in a crisis model. The second analysis is more specific, focusing on themes that are attached to individual LTCs. The third analysis, which investigates the personal experiences among individual users, is the most personalized and nuanced.

For the first portion of the analysis, and in order to organize the past event tweets over time, the Fink crisis model (Fink 1986) is used. The stages of the model and the time periods they correspond to for this analysis on Harvey are listed in Table 7.3. In this study, the prodromal stage is defined as the start of the tweet collection period (0000 UTC 22 August) through 0000 UTC 26 August, which is when conditions began to rapidly deteriorate in many areas of southeast Texas. The acute stage begins immediately after, with the "triggering event" being this onset of TC conditions for southeast Texas. The stage ends at 0800 UTC 30 August, at which point Harvey had largely weakened and was making its final landfall in Louisiana. This marks the beginning of the chronic stage, which then continues through the end of the tweet collection period (0000 UTC 3 September). The final stage, resolution, was not included in this study because the period over which the data was collected does not include the point at which the crisis was fully resolved. Therefore, the tweets are only sorted among the prodromal, acute, and chronic stages for the analysis. Using this model as a framework, emerging thematic and temporal trends in the past event tweets among the different stages of Harvey are identified.

Table 7.3: Four stages of crisis defined by Fink 1986, as well the dates and times defined for each stage over the 12-day period of study for Harvey.

Stage	**Description**	**Time Period**
Prodromal	Before the crisis	0000 UTC 22 Aug - 0000 UTC 26 Aug
Acute	Crisis itself, beginning with a triggering event	0001 UTC 26 Aug - 0800 UTC 30 Aug
Chronic	Crisis ongoing/ “clean-up” stage	0801 UTC 30 Aug - 0000 UTC 3 Sep
Resolution	End of crisis	N/A

For the second part of this analysis, past event tweets pertaining to three of the most frequently-mentioned events (all of which are LTCs) are assessed for themes individually. Commonly held themes or “identities” that many of the users tie to each storm are discussed. The relationship of these identities related to events unfolding during Harvey is also explained.

For the third part of the analysis, the past event tweets are examined to see the ways in which past experiences emerge among them. In order to identify the nature of these experiences, direct versus indirect experiences must be explicitly defined. For this study, a qualifying direct experience requires that the user’s past event tweet contains evidence to support that they were a permanent resident of or temporary visitor to the area the referenced event influenced at the time it occurred, temporarily fled (i.e., evacuated) the affected location just before the event or visited the site of the disaster after it happened. Direct experiences can be further classified as being tangible or intangible. Tangible direct experiences are defined here as being able to be touched, measured, or seen by others, whereas intangible direct experiences are "invisible" and not easily measured. Indirect experiences, which can only be intangible, are defined as tweets that reference a past event and include an explicit statement that the experience they describe was mediated through someone or something other than themselves, such as the media, friends, or family, and/or there is obvious evidence that the person was not at the site of the past event. In any case, intangible experiences are frequently equated to expressions of emotion.

Though their information is public at the time of these analyses, the identity of the Twitter users is protected by anonymizing all usernames. Additionally, the wording of the tweets presented herein is altered slightly (without compromising the original meaning) to further protect user identity (e.g., Demuth et al. 2018). These steps follow guidelines for ethical Twitter research as suggested by Fiesler and Proferes (2018). Note that some tweets contain spelling and grammar errors that are reflective of the non-altered tweets, and there are a few instances of strong language.

CHAPTER 8: RESULTS AND DISCUSSION

In this section, the results corresponding to the two research questions presented at the start of Part II are shared. After offering some general statistics for the users and their tweets in section 8.1, the temporal trends of the past event tweets are discussed in section 8.2. Section 8.3 highlights the unique themes that accompanied three frequently mentioned LTCs in the past event tweets. Section 8.4 describes the ways in which individual experiences emerged in the past event tweets. Section 8.5 provides discussion for sections 8.1-8.4.

8.1 Statistics on Users and Their Tweets

The 39 users of interest collectively sent a total of 10,697 original tweets (i.e., non-retweets) over the period of study (Fig. 8.1, Step 10). The range in number of tweets per user was large, with the selected users tweeting anywhere between 28 and 1049 times over the 12-day period. The mean number of tweets per user during this time was approximately 274. Additional statistics can be found in Fig. 8.1. Despite a broad domain being set over southeast Texas and southern Louisiana, the majority of users resided in Houston and its surrounding suburbs at the time of Harvey, with only a handful coming from other areas of Texas or Louisiana. While the fact that the Houston metropolitan area is the fifth largest in the United States by population (United States Census Bureau 2019) could help explain the disproportionalities within the sample, there could be other explanations for this characteristic. For instance, the lack of spread in user locations could be a result of residents in other parts of Texas (such as Corpus Christi), which were located closer the eye of Harvey as it made landfall and thus experienced stronger winds and more widespread power outages early in the event than areas such as Houston, which were further from the center of the storm when it was at its peak intensity. This factor could have hindered communication for residents who experienced impacts in the early stages of Harvey's landfall, which would have likely prevented them from ever sending TORFF tweets (i.e., the first query that was used to identify the group of users that was included in the analysis) during the height of the impacts, effectively eliminating their likelihood of ever being included in the database.

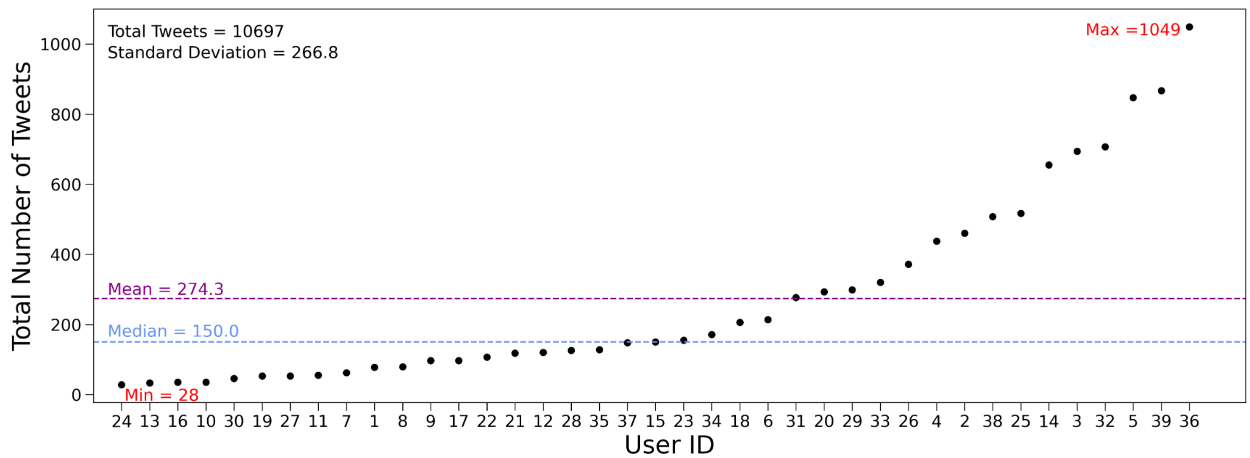

Figure 8.1: Total number of tweets shared by each of the 39 southeast Texas/southern Louisiana users between 0000 UTC 22 August and 0000 UTC 3 September 2017.

34 of the 39 users identified explicitly referenced at least one specific past event in a past event tweet, while the remaining 5 users exclusively alluded to non-specific experience with weather-related events. There were 13 specific events referenced, and these events were referenced a total of 186 times, indicating that several of the tweets collected included more than one event in them (Table 8.1).

There was a wide distribution in the number of times a given hurricane or flooding event was mentioned by the users. By far, the most frequently referenced event was Hurricane Katrina (2005), mentioned at least twice as frequently as all other storms (Table 8.1). Hurricane Ike (2008) was the second most mentioned storm (33 references) followed by Hurricane Rita (2005) and Tropical Storm Allison (2001) (referenced 30 times each). All other events were referenced no more than 6 times.

Table 8.1: Specific events mentioned in tweets during the period of study by Twitter users identified as being located in the southeast Texas and southern Louisiana region.

Event	**Number of Mentions**
Carla (1961)	1
Alicia (1983)	3
Andrew (1992)	3
Allison (2001)	30
Katrina (2005)	67
Rita (2005)	30
Wilma (2005)	1
Ike (2008)	33
Gustav (2008)	2
Sandy (2012)	6
Memorial Day Floods (2015; 2016)	5
Bill (2015)	2
Tax Day Flood (2016)	3
ALL EVENTS	186

8.2 Temporal Analysis of Past Event Tweets Using the Fink Crisis Model

In this section, the past event tweets are investigated in a relatively broad sense, as they are discussed thematically during different stages of the disaster (according to the Fink crisis model). To summarize these findings, these results show that tweets sent during the prodromal stage tended to focus on sharing direct experiences and drawing comparisons between Harvey's predicted intensity and past events that they are familiar with. The acute stage, which was the most active period of tweeting, had several embedded crises within it (both meteorological and sociopolitical), each of which the users collectively associated with a past, analogous event. Further, a shift from meteorological comparisons to impact-based comparisons was evident among the past event tweets that were sent during the acute stage. This shift to impact-based comparisons continued into the chronic stage, which is when past events began to be discussed in more of a reflective tone.

8.2.1 Broad Temporal Trends in Tweeting and a Brief Connection to TORFFs

When all tweets sent by the users are examined temporally by the three Fink crisis model stages that are being evaluated (Fig. 8.2), the hourly rate of tweeting was generally highest during the acute stage compared to the prodromal or chronic stages. The mean rate of tweeting was 53.47 tweets h^{-1} during the acute period, which was more than twice that of the prodromal (27.42 tweets h^{-1}) and chronic (28.45 tweets h^{-1}) stages. As would be anticipated, there is a clear diurnal trend in the tweets, with most activity occurring during the daytime hours. There is one exception to this however, which is the night of 26-27 August. During that period, there were many tornado warnings, flash flood

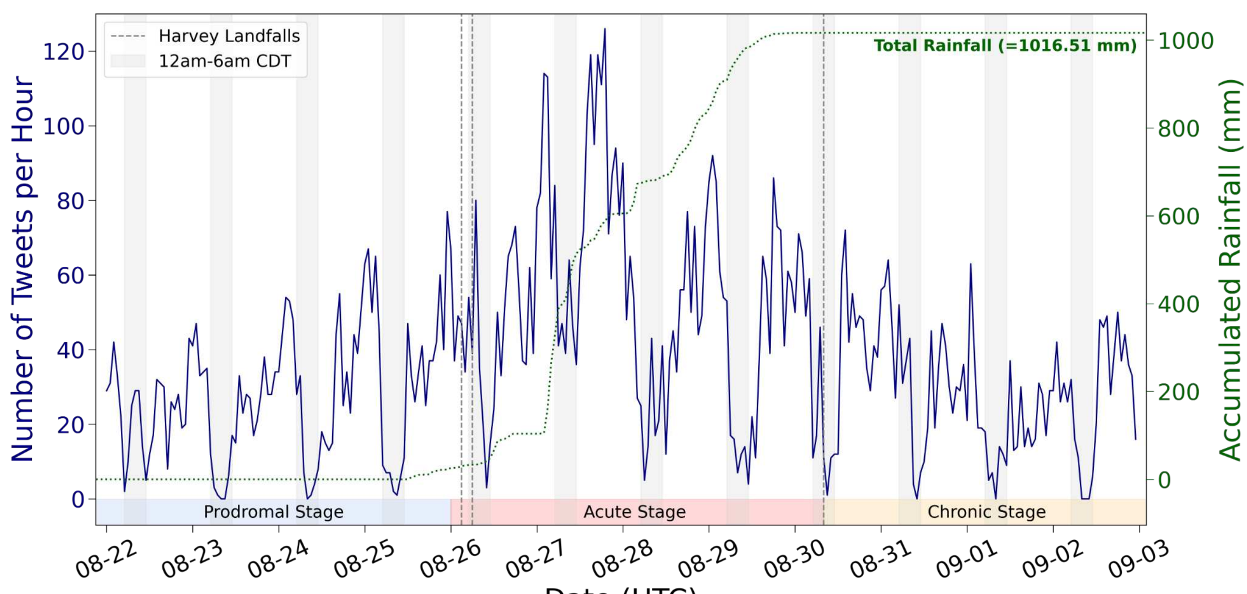

Figure 8.2: Time series of tweets per hour by the 39 users (solid navy line) and accumulated rainfall (dashed green line, as in Fig. 7.4). Also shown are the times of Harvey's 3 landfalls (vertical dashed grey line) and overnight hours (defined as 12am-6am CDT, grey shading). The time periods representing the first three stages of the Fink crisis model (as defined in Table 7.3) are labeled and shaded at the bottom of the plot.

warnings, and TORFF warning overlaps that occurred across the area of study (Fig. 8.3), which illustrates the severity of the storm during this particular time period.

When only the 158 past event tweets were examined, the acute stage was again the most active period of tweeting among the three stages of the Fink crisis model that were used. Nearly two-thirds of them (101 tweets) were sent during that period compared to the prodromal (29 tweets) and chronic (28 tweets) stages.

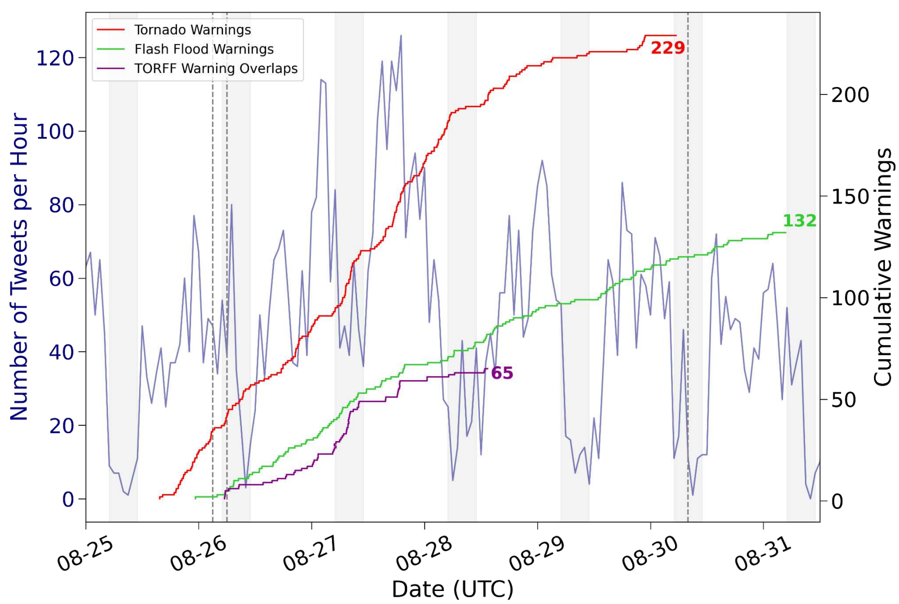

Figure 8.3: As in Fig. 8.2, but zoomed in to dates between 25 Aug 0000 UTC and 31 Aug 1200 UTC. Also shown are cumulative Harvey-related tornado warnings (red), flash flood warnings (light green), and tornado and flash flood (TORFF) overlaps (purple) across the Corpus Christi, Austin/San Antonio, Houston, Lake Charles, Shreveport, and New Orleans National Weather Service county warning areas. Numbers annotated by each of the lines represents the total number of each warning type that occurred over the period. Tornado and flash flood warning data are courtesy of Iowa State University Iowa Environmental Mesonet NWS warnings archive, and TORFF overlapping warning data are courtesy of Erik Nielsen, and TORFF warning overlaps follow the definition provided in Nielsen et al. (2015).

8.2.2 Prodromal Stage: Recalling Personal Experiences and Assessing Uncertainty

Beginning with the 29 tweets associated with the prodromal stage, the past event tweets mentioned at this stage of Harvey were largely connected to individualized past experiences. That is, as details on Harvey's forecast began to emerge, users thought back on the experiences they had during past events. This theme will be discussed in more detail in section in section 8.4, but to include a few examples here:

> @user7, 25 Aug 0111 UTC: @user Oh I see. I'm in Barker/Cypress. Oh my! So you will have to monitor Spring Creek! When Ike came, roofs were damaged but no flooding.
>
> @user36, 25 Aug 0341 UTC: @user Thank you. My neighborhood didn't flood in Ike, but rain doesn't falls the same way twice.

Others draw or seek meteorological comparisons between the forecast for Harvey and forecasts for past events that they are able to recall:

> @user29, 24 Aug 2120 UTC: This won't be fun… Harvey looks like Allison on steroids
>
> @user3, 25 Aug 0320 UTC: Hurricane Ike hit at 1 AM in 2008. Hutticane Harvey is hitting at 1 AM this is déjà vu!!!
>
> @user15, 25 Aug 1837 UTC: @meteorologists in comparison, how much rain did we have with Ike and Allison?

8.2.3 Acute Stage: Comparing Past Impacts and Political Responses

As was seen in the prodromal stage, direct experience tweets were also shared during the acute stage, though since there were more than three times as many past event tweets shared during this stage compared to the two other stages, that theme is much less prevalent during this stage.

An interesting feature in the acute stage of the tweet collection period is that there appears to be smaller temporal trends with regards to when specific storms are mentioned within various parts of that stage. To visualize this, cumulative sums of three of the most-mentioned events in the dataset (Tropical Storm Allison, Hurricane Rita, and Hurricane Katrina) during the tweet collection period are shown in Fig. 8.4.

For Tropical Storm Allison specifically, there are sharp increases in the cumulative number of Allison-referenced tweets that were sent during the earlier part of the acute stage. According to Fig.

8.4, a sharp increase in Allison-related mentions begins soon after 0500 UTC on 27 August, which is midnight local time. A total of 9 tweets referencing Allison are sent over the 8-hour period between

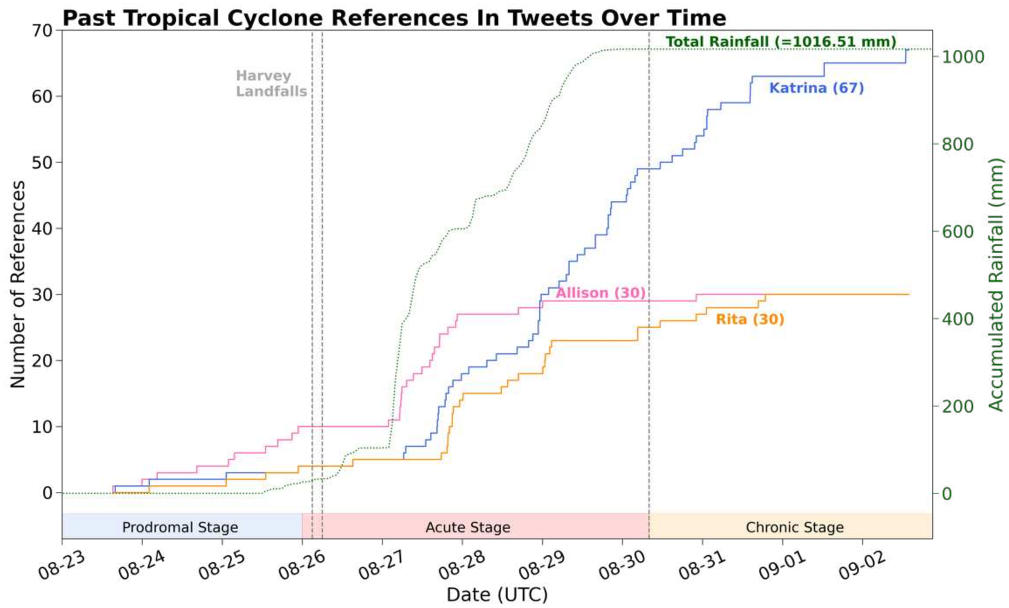

Figure 8.4: Cumulative references to 3 frequently-referenced tropical cyclones for the 39 users analyzed. Storm names are color-coded with their respective data, and the numbers next to each event represent the total number of mentions for each event over the 12-day period. The vertical dashed grey lines show the times of Harvey's 3 contiguous United States landfalls, and the green dotted line shows accumulated rainfall gauge-averaged rainfall near the Houston airport, as described in Fig. 7.4. Fink crisis stages are shaded and labeled along the x-axis, as in Fig. 8.2.

0500 UTC and 1300 UTC, which accounts for nearly one-third of all Allison-related tweets collected over the 12-day period. During this period, several users share that Harvey's storm-total rainfall surpassed the maximum rainfall total associated with Allison—a fact which many of them heard on the news and is supported by the rapidly accumulating rainfall shown in Fig. 8.4. Although it was a Saturday night, timestamps show that users were awake during the overnight and early morning hours and were monitoring the situation:

> @user36, 27 Aug 0510 UTC: Harvey move your ass, this one mph shit is bullshit, I told him he shouldn't listen to Allison. She was a bitch

> @user38, 27 Aug 0553 UTC: Trump's 1st natural disaster is in US's 4th largest city!! Under flood emergency. Worse than Allison... may beat Alisha!

> @user25, 27 Aug 0626 UTC: The news says Harvey has surpassed Allison's rain. If you aren't familiar, highways were underwater. #HurricaneHarvey

@user9, 27 Aug 0920 UTC: The news says the water levels are greater than they were during TS Allison 😳 #Harvey2017

Similar tweets continue throughout the day as heavy rainfall continues, with users largely comparing Harvey to Allison, specifically in terms of rainfall:

@user5, 27 Aug 1625 UTC: #Harvey record rain fall is unprecedented, I've never seen a #houston flood like this. The closest was #Allison 18 yrs ago...

@user25, 27 Aug 1743 UTC: Another hospital evacuation. Houston metro had historic flooding with Allison. Seems like it's happening again. #Houstonflood

Much like Allison, there is a prevalent increase in the number of Rita references in the past event tweets during the acute stage, but the increase occurs later in the acute stage compared to Allison. Tweets related to Allison largely level off by 1800 UTC 27 August, which is approximately when tweets related to Rita begin to ramp up. Over the next eight hours, 10 tweets containing references to Rita are sent. In these tweets, users strongly defend the decisions made by officials not to evacuate Houston during this time period, including by using anecdotal evidence about their own evacuation decisions:

@user36, 27 Aug 1954 UTC: Unless you sat on the interstate during Rita when 4 million people, tried to leave on 3 roads, stop shit talking

@user5, 27 Aug 2059 UTC: I evacuated for Rita. Houston to Austin normally: 4 hrs max. Then: 26 hrs! Leaving would have been MORE dangerous!

@user24, 27 Aug 2335 UTC: I have mixed feelings about Mayor Turner, but he's right that an evacuation would have made #Harvey an even bigger disaster (see Rita).

Another, smaller period of increased Rita-related tweet activity occurs around 0000 UTC 29 August, though this spike can be largely attributed to a single user sending multiple Rita-related evacuation tweets in a short time span.

As the Rita references wane, the latter part of the acute stage (beginning after around 0000 UTC 29 August) consists of past event tweets containing mostly Katrina references. This seems to partially because 29 August marked the 12-year anniversary of Katrina, which many users, particularly those with ties to New Orleans, are able to recall:

> @user16, 29 Aug 0212 UTC: It's the eve of Katrina's anniversary, and we have warnings for tornadoes and flash floods in New Orleans. God, bless the south😔🚧🌪🌊🛶
>
> @user33, 29 Aug 1554 UTC: Today is the 12 year anniversary of Hurricane #Katrina #TwitterNewsChat
>
> @user2, 29 Aug 1711 UTC: Trump just said "No one has ever seen something like this" on the anniversary of Katrina hitting new Orleans.
>
> @user18, 30 Aug 0146 UTC: 8:45 pm: why I am thankful. 12 years ago, Katrina was impacting my hometown of New Orleans. It... [link to facebook]
>
> @user35, 30 Aug 0229 UTC: Some perspective... Hurricane Katrina dropped 16" of rainfall on New Orleans 12 years ago today #HurricaneHarvey #houstonflood

This latter acute stage also includes a few periods where one user rants about Joel Osteen not opening his megachurch for Harvey victims, something the user seems to believe also happened to Katrina victims (see section 8.3.2 for additional context).

By stepping back to examine the acute stage as a whole, there appears to be a shift where users begin to view Harvey more as a disaster, rather than a meteorological phenomenon. While in the earliest part of the stage, users drew comparisons between rainfall and wind between Harvey and past events, as the rainfall continued and the flooding worsened, comparisons became more impact-based and disaster-focused. This transition generally began when scenes of rescue and recovery began to emerge and get coverage in the media, soon after rainfall totals surpassed those from Tropical Storm Allison. By mid-afternoon on 27 August, residents had begun fleeing their homes:

> @user39, 27 Aug 1957 UTC: Looks just like Katrina , people trapped on highways and bridges, not knowing whats next? System overwhelmed

As users watched the scenes of widespread flooding and rescue operations, discussion transitioned from being less focused on the rain and flooding (which were often mentioned win association with Allison) but instead focused on the impacts of it. Evidence of this includes the increased references to the Rita evacuations, where users defend the decisions made by local officials. Focus also shifts to concern for the victims and evacuees, where outrage is sparked over them being called "refugees" (see section 8.3.2 for more details) and the controversial move by Joel Osteen to delay opening of his church as a shelter for them.

8.2.4 Chronic Stage: Reflecting on Societal and Personal Trauma

By the chronic stage, meteorological comparisons related to Harvey and past events are non-existent. However, the focus does remain on drawing impact-based comparisons between Harvey and past events, specifically Katrina:

> @user25, 30 Aug 2207 UTC: This. Is. Worse. Than. Katrina. Its impacting the entire coast of Texas and Louisiana too.
>
> @user39, 2 Sep 1254 UTC: @user Harvey will be more costly than Katrina. There was bad flooding even in places with modern drainage systems
>
> @user39, 2 Sep 1336 UTC: @user Those are just early estimates. [Damage costs] will be higher. Harvey damage area is MUCH larger than post-Katrina New Orleans

Additionally, a couple of users appear to become reflective on past events as the focus shifts from disaster management towards disaster recovery after Harvey. One user acknowledges feeling fortunate that they did not experience worse impacts, while another uses a thread to reflect on their experience with post-Katrina disaster victims:

> @user31, 30 Aug 1452 UTC: - I really dodged a bullet with Hurricane Ike & Harvey. Now it's time to help friends recover they've lost so much including a life.
>
> @user6, 31 Aug 1416 UTC: When I was a sophomore at CU Boulder, a some students from LSU, who were displaced after Katrina, came to classes with us.
>
> @user6, 31 Aug 1419 UTC: I was nice to the LSU kids displaced after Katrina and I thought I understood them. Looking back, I didn't understand at all
>
> @user6, 31 Aug 1454 UTC: Harvey brings back so many memories of Katrina.

8.3 Thematic Explication of Individual Events

Themes that were specific to an individual past TC were found among three events: Tropical Storm Allison (2001), Hurricane Katrina (2005), and Hurricane Rita (2005). These findings show that each of these storms were described as having their own "identity" in the past event tweets—that is, they were bound by a common topic of conversation. To summarize, Allison's identity was tied to rainfall amounts, Katrina's was frequently referenced in the context of sociopolitical issues, and Rita's was discussed in tandem with evacuations.

8.3.1 Tropical Storm Allison: Meteorological Comparisons

Among the five most-frequently mentioned events, Tropical Storm Allison (2001) is the most appropriate comparison to Harvey from a meteorological standpoint. Though much weaker than Harvey in terms of wind speed, the system lingered over the Gulf Coast region for several days, which allowed tropical moisture to remain stagnant and led to widespread, flood-producing rainfall (see Fig. 7.5 for a comparison of Harvey and Allison rainfall). The Allison-related tweets by the users demonstrate familiarity with the event meteorologically, and Harvey seems to trigger some of these memories, prompting them to draw comparisons to Harvey. They recall the slow motion of the storm and that Downtown Houston saw significant flooding, both of which also occur with Harvey:

> @user36, 27 Aug 0510 UTC: Harvey move your ass, this one mph shit is bullshit, I told him he shouldn't listen to Allison. She was a bitch

> @user25, 27 Aug 1743 UTC: Another hospital evacuation. Houston metro had historic flooding with Allison. Seems like it's happening again. #Houstonflood

Despite living in Houston for Allison, one user refers to Harvey's widespread tornadoes and flooding as being an unprecedented experience for them:

> @user3, 27 Aug 0535 UTC: I was here in Allison & you're right this feels like a non-stop nightmare! I've never seen so many tornados & flooding!

Several other users compare the two events and argue that Harvey is worse, though they are not explicit as to which aspect of the event they are referring to (e.g., flooding, damage, etc.):

> @user29, 24 Aug 2120 UTC: This won't be fun… Harvey looks like Allison on steroids

```
@user38, 27 Aug 0545 UTC: Harvey AIN'T weakening in Houston. Might be worse than Allison
and Alisha

@user5, 27 Aug 1434 UTC: I'm from Houston can say it hasn't been like this since 2001,
Allison? It is way worse than the memorial day flood
```

Allison was also frequently compared to Harvey by media outlets, which was a unique theme found attached to that storm specifically. Users explicitly noted that the information they were passing along to their followers was from "the news". Their tweets involved comparisons related to rainfall amounts, flooding, and estimated disaster-related costs:

```
@user25, 27 Aug 0626 UTC: The news says Harvey has surpassed Allison's rain. If you
aren't familiar, highways were underwater. #HurricaneHarvey

@user9, 27 Aug 0920 UTC: The news says the water levels are greater than they were during
TS Allison 😳 #Harvey2017

@user33, 27 Aug 1538 UTC: @newsanchor just said this weather event is considered to be
"worse than" Allison flooding.

@user3, 27 Aug 2310 UTC: The news said Allison had $5 billion of damage but
#HurricaneHarvey is going to exceed that by far!!!!!
```

Regardless of whether the users were receiving explicit forecast information from the news or they were relying on their own memories, users almost always associated Allison with heavy rainfall or flooding when they tweeted about the event.

8.3.2 Hurricane Katrina: Evoking Lessons Learned

Hurricane Katrina was an unprecedented storm, though less-so for its meteorological impacts, but rather for the failures that ensued during recovery efforts. There were sociopolitical issues that unfolded, from inappropriate news reporting, to delays in relief supplies, to neglect by political administrations. Katrina-related tweets tended to draw on these subjects while they were being shared during Harvey. For example, on several occasions, users expressed disappointment in the media when the word "refugees" was used to describe Harvey victims rather than "evacuees" or "residents"—a lesson that they believe should have been learned from Katrina:

@user2, 28 Aug 0013 UTC: They're not refugees - same mistake was made with Katrina. Evacuees please.

@user33, 28 Aug 1650 UTC: #HurricaneKatrina Lesson: Please, do not call our neighbors "Refugees." They're residents and citizens of Houston, Rosenberg, Rockport ...

Another user cautioned reporters to be more sensitive in the way they conduct their journalism in general, since many Katrina victims relocated to Texas after the disaster (e.g., Sastry and Gregory 2014; Jan and Martin 2017):

@user38, 29 Aug 2026 UTC: @CNN & other news media: we have Katrina evacuees who relocated here. Please respect, many of them are going through HELL again

In addition to the controversy surrounding the media's coverage of Harvey, local and national politics also prompted users to refer back to sociopolitical issues that occurred with Katrina. Some users recall the failures of the government and their abandonment of the residents who were impacted:

@user39, 27 Aug 1924 UTC: Houston reminds me of Katrina right now. A system overwhelmed and people having to help others and themselves #houstonflood

@user39, 28 Aug 1140 UTC: @user Houston has mirrored Katrina without as many deaths and huge incompetence. The expenses are going to be staggering #HoustonStrong

@user20, 31 Aug 0315 UTC: Neighbor saving neighbor. Katrina showed don't rely on the government to rescue you. Save yourself and save your neighbors

Other users expressed concern specifically over Former President Donald Trump's ability to handle Harvey recovery based on their opinions of his presidential track record:

@user2, 23 Aug 2358 UTC: [Trump being president] makes me worried just as much as Harvey itself. Katrina showed how officials at the local, state, and federal levels have to work together.

@user38, 27 Aug 1459 UTC: Remember Houston opened the Astrodome for Katrina victims? Now who will open the doors for Houston? Not Trump!

@user2, 27 Aug 1906 UTC: I have lived in New Orleans and housed Katrina evacuees. The lack of leadership by POTUS is astounding #HoustonFlood

One user also tweeted frequently (over 15 times) about Joel Osteen, a pastor at a large Houston church, who while not a politician, sparked controversy when he did not initially open his building for Harvey evacuees (Dart 2017). The author of the tweets alleges that this was an action that he also did not take during Katrina, though that claim was not able to be validated. Given the frequency of the tweets, this issue appears to be very personal to the user, and/or they feel very passionate about the issue. For an example of one of these tweets:

> @user38, 29 Aug 2039 UTC: Osteen and his Megachurch had to be shamed to open. They NEVER opened for Katrina evacuees. They DONT deserve good PR!

In essence, as additional issues other than weather-related damages began to arise in areas impacted by Harvey, such as slow-moving rescue operations or mistakes by local leaders, Katrina was evoked by the users as an analog to the events they were witnessing, since they collectively recall the event as having numerous sociopolitical issues that were ultimately more severe than the LTC itself.

8.3.3 Hurricane Rita: Legitimizing Evacuation Decisions

Hurricane Rita was a unique TC disaster in that the majority of impacts came during storm preparations rather than during or after the event. Specifically, massive mandatory evacuations left thousands stranded on interstates in gridlocked traffic. With residents fearful of the aftermath that Katrina brought, many more people evacuated than needed to, and combined with the lack of supplies and extreme heat, over 100 people died on the interstate (Baker 2018). For these reasons, Rita was largely recalled by users in conjunction with evacuations among the past event tweets. In fact, evacuations and Rita were arguably the most obvious tie between theme and storm with this analysis: 19 of the 29 tweets that reference Rita also explicitly mention evacuations, and evacuations were rarely mentioned in association with other past storms. Several users explicitly state that they were in the Rita evacuations themselves and recall the dense traffic and deaths on the roadways:

> @user30, 27 Aug 2110 UTC: @newsanchor and @user In Rita we tried to evacuate. After 13 hours we had only driven 43 miles.

> @user5, 27 Aug 2202 UTC: @bethreinhard In Rita I remember TRYING to evacuate, it was a disasters in it of itself, a 4 hr ride became 26 hrs!

> @user38, 29 Aug 0043 UTC: @user I agree. I was in the evacuation during Rita and 100 people died in traffic incidents

Even if they did not explicitly state that they were in the evacuations themselves, most users in the sample seemed to be strongly against mandatory evacuations in the case of Harvey and supported their opinion by using Rita as an example. Others explicitly backed up the decisions of state and local lawmakers to not issue a mandatory evacuation in Houston by exemplifying the failures associated with Rita. Often, the users also assert that experience with Rita is a prerequisite to being able to hold a legitimate opinion on whether or not Houston should have been placed under mandatory evacuation:

> @user36, 27 Aug 1954 UTC: Unless you sat on the interstate during Rita when 4 million people, tried to leave on 3 roads, stop shit talking
>
> @user24, 27 Aug 2335 UTC: I have mixed feelings on Mayor Turner, but he is right that an evacuation (see Rita) would have made #Harvey disaster even bigger.
>
> @user11, 28 Aug 1335 UTC: Don't tell us shit about evacuations unless you know about #Rita. Keep #Houston outta your mouths ok?
>
> @user5, 29 Aug 0247 UTC: @user pls stop doggin @SylvesterTurner if you had lived in Houston and tried to leave during Rita, you'd know why!!
>
> @user5, 29 Aug 0500 UTC: y'all blamin @SylvesterTurner @GregAbbott_TX 4 not coordinating a evac. U obviously did not live in Houston during Rita!

In other words, the users share their experiences to put themselves in a place of authority that not only allows them to have an opinion on the handling of Harvey evacuations, but also, in their minds, allows them to use experience to gatekeep opinions on the matter by restricting valid criticism to only those who had experienced the failed evacuations themselves.

8.4 Individual Direct Experiences with Past Events

The previous two sections have viewed experience in a broader sense. In this section, the finer details of experience among the users are further examined. These results show that within the past event tweets, users shared direct experiences, both tangible and intangible, that are personal and unique to them. Both types of direct experience appear to be equally prevalent among the data.

Some examples of direct tangible experiences from the dataset include:

@user32, 24 Aug 2356 UTC: naw they said ike was supposed to hit bad and i was at the park in crestmont. 😂

@user3, 25 Aug 0340 UTC: OMG 2 wks??? With hurricane Ike I was without power for 3 days in 100 degree heat & that was unbearable!!!!

@user36, 25 Aug 0343 UTC: @user I lived in Baytown during Allison and the downstairs of my apartment building was flooded.

@user36, 25 Aug 1301 UTC: @user I lived in Baytown during Allison and there was really bad flooding, luckily I lived in a second floor apartment,

@user37, 25 Aug 1324 UTC: We're not going to be sitting ducks. I survived Ike and Rita doing that, and know my luck is going to run out. #HurricaneHarvey

@user38, 25 Aug 2248 UTC: When Tropical Storm Allison stalled over Houston area as is expected with #Harvey, it took me 36 hours to get home!

@user21, 26 Aug 0127 UTC: @user Stay safe. We're near Galleria hopefully shld be dry ☝🏻 B4 Ike packed freezer w/water bottles. Kept food & water cold longer when power out

@user5, 27 Aug 2058 UTC: @user yep. Evacuation would have actually put more ppl in danger. I evacuated for Rita, and a 4 hr drive turned into 26 hrs!!!

@user24, 27 Aug 2342 UTC: Even with mandatory evacuation I would've stayed home where I survived Ike, Memorial Day flood, Tax Day flood. Take responsibilities seriously.

@user2, 31 Aug 0530 UTC: True story: ironically one of my very first tweets was telling my 0 Twitter followers that I was evacuating for Ike.

In the above tweets, each user makes it clear that they were in the location of the storm when it occurred and that they personally had a tangible experience. The specific tangible experiences that the users described as having happened directly to themselves mostly focus on impacts to their property, barriers to travel, or externally driven disruptions to their livelihood. Additionally, there are several users who note that during some of the past, significant events, they had decided not to evacuate—a choice that also constitutes a tangible direct experience given that it is something that is able to be seen by others. These past evacuation decisions are described by the users for two reasons. The is to allude to how their past decision to not evacuate during an event that they directly experienced informed their evacuation decision for Harvey. The second is to use their past decision to not evacuate as a way of helping them make sense of the current information they are receiving on the severity of Harvey.

Instances of direct, intangible weather-related experiences were also identified among the past event tweets. The experience is direct because the user states that they were physically present at the location where the event occurred, and it is intangible because the effects being described cannot be seen, heard, etc.:

> @user28, 23 Aug 1516 UTC: I'm beginning to panic. I think I may have PTSD from the last big flood we had.
>
> @user36, 24 Aug 0207 UTC: Tropical Storm Allison was my first Houston storm experience and she was a bitch.
>
> @user25, 24 Aug 1615 UTC: After #HurricaneAndrew I went through there with my Dad. The dead animal smell was overwhelming.
>
> @user23, 24 Aug 1624 UTC: I've ridden through many hurricanes in my life, & have been lucky. Just minor damages & crossing my fingers for this 1, it worries me
>
> @user31, 25 Aug 0153 UTC: I lived in Galveston Island for 6yrs and was there in Katrina, Rita and Gustav. It was the scariest thing ever!
>
> @user26, 25 Aug 1633 UTC: So 4 those of u who don't know: my ptsd started w/ surviving a tornado as a child. They found us in a field and we lost everything we owned
>
> @user26, 25 Aug 1641 UTC: I've survived many storms, we were in Houston during Ike. I'm prepped - even tho my hyper vigilance tells me to do more more more
>
> @user4, 26 Aug 1330 UTC: In Florida I've been through Hurricanes, but I've never seen one so stationary and big! I wish it would just move! 🙃☔ #Harvery
>
> @user36, 26 Aug 1506 UTC: Seeing some of the damages out of Rockport and Port A, I feel for those people. After Ike I woke up crying and shit was a mess
>
> @user3, 27 Aug 0535 UTC: I was here in Allison & you're right this feels like a non-stop nightmare! I've never seen so many tornados & flooding!
>
> @user29, 27 Aug 1944 UTC: I have been in Houston for Rita, Allison, Ike, the Memorial flood and now #Harvey. By far Harvey is absolutely the worst.
>
> @user18, 28 Aug 1012 UTC: This is only day 3 of what is supposed to be day 5 or 6. Im from NOLA and katrina wasn't this bad. Maybe it was. This feels like agony
>
> @user27, 28 Aug 0720 UTC: I can't believe it. In the developing world I grew up with hurricanes and earthquakes and my worst experience is in the developed world
>
> @user14, 28 Aug 2312 UTC: I am deadass not tryna re-experience Katrina 🤦🏽‍♀️
>
> @user31, 30 Aug 1452 UTC: I dodged a bullet in Ike and Harvey. Now I need to help friends- they lost so much even a life

Here, intangible experiences are seen broadly in the form of emotions or feelings. Specifically, the users use words that express several negative emotions, including fear, worry, exacerbation, and being overwhelmed. In a couple cases, emoticons in the tweets help to portray the feelings of the users. Beyond the negative emotions, past experiences also seem to be associated with some mental health challenges in a few of the users, which is evident in the references to PTSD (posttraumatic stress disorder) and anxiety, for example.

It appears that the emotion associated with the intangible experiences are described on three different time scales. In some cases, the user recalls their emotions or trauma as feelings that occurred in the past—that is, concurrently with the past event that they describe. In other examples, the users express that they feel the negative emotions in the present, meaning that the feelings may have originated during the time that the past event took place, but the anticipation of Harvey's impacts in the days before the event is reinvigorating those emotions. On a third time scale, even though the tweet mentions a past event, it appears that the feelings that the user expresses are new: they develop during Harvey and are not associated with a past event that they went through. In other words, the user either 1) reflects on how they felt during a past event, 2) evokes their experience with the past event to help them attend to the emotions they feel as Harvey is beginning to reignite feelings from the past, or 3) develops new negative emotions as they experience Harvey that are separate from the past event.

There also seems to be some temporal variability with regards to the types of emotions that are felt during different stages of the storm. For example, many of the negative emotions that are described in the earlier part of Harvey (i.e., in the prodromal or early acute stages) are anticipatory, such as expressions of fear of the unknown or hypervigilance. As time goes on and Harvey lingers over the area, it seems that the negative emotions shift to become more characteristic of exasperation or exhaustion. In the last several days of the event, intangible direct experience (as well as tangible) is almost nonexistent in the dataset of past event tweets.

Lastly, it is worth noting the interconnectedness of the tangible and intangible experiences. Namely, in several of the tweets, tangible effects are mentioned alongside the intangible effects.

Furthermore, the intangible experiences appear to be just as prevalent in the past event tweets as tangible experiences are based on the number of times that each type of direct experience is referenced.

8.5 Discussion

The results presented above suggest that there are two overarching reasons that users attend to past events during Hurricane Harvey. First, they refer to the past event because they have some personal connection to the storm. Second, the users use the event as an analog to help them contemplate and make sense of the events that are unfolding around them during Hurricane Harvey. Drawing on the results presented above, the following discussion demonstrates how the above analyses of the past event tweets can contribute to a better understanding of experience in the context of weather-related disasters. Applications of these results with regards to practices by decision-makers and leaders, such as emergency managers, meteorologists, and political figures are also considered.

To summarize, the temporal analysis suggests that experiences with past events are described in ways that reflect stages of a disaster, like the Fink model, because past events share similarities with the specific circumstances that are unfolding throughout the current hazard (which is Harvey in this case). These personal experiences with past events are also recalled to help the users make sense of these events over time. Results that examined specific TCs suggest that some past events have become a shared experience among multiple users. Additionally, as Harvey unfolds, the individual storm references in the past event tweets also serve as a timeline that can be used to track the multiple crises embedded within Harvey (e.g., impacts of record flooding). Past event tweets examined across individuals show that different types of experience with past events (e.g., tangible or intangible) can be long-lasting and insightful to the users' understanding of the circumstances they face throughout

Harvey. Further, though there are some commonalities in the ways that users describe certain past events, these results suggest that for individual users, personal experience is incredibly complex and variable, depending on the aspects of the past storm that people endured. As a whole, these findings show that by examining experience through the lens of past events across various dimensions, insight on the ways in which the public manages weather-related disasters can be gained.

8.5.1 Temporal: Experience Across Crisis Stages

The temporal analysis of the past event tweets demonstrates that during an event, collective experience can be inferred based on the frequency of the tweets, as well as the events that are taking place during a particular stage. Using the Fink crisis model, the results above showed that the acute stage was a much more active period of tweeting compared to the prodromal and chronic stages, a finding that is consistent with Xu et al. (2019)'s application of the same model to tweets that were sent throughout Hurricane Irma. Additionally, there was a period (26-27 August) in the acute stage where the nocturnal maximum in tweeting was much less pronounced compared to other overnight periods in the analysis. These elevated periods of tweeting suggest that the acute period was when users were most attuned to the hazards taking place around them. It appears that they were using social media as a distraction, source of information, or coping mechanism while they were going through the most severe impacts of the event. These increases in attention mirror the increased frequency of warnings and the rainfall rates that were taking place at the time, suggesting that individuals may have been actively tweeting more because of local impacts of hazards and warnings for them.

The temporal analysis of the past event tweets also suggests that past events are evoked to help users make sense of the circumstances that they encountered at different stages of the event. For example, tweets in the prodromal stage largely focused on emotional impacts and disruptions to life that resulted from past events. At this point in the disaster, users were anticipating the impacts of the impending crisis, though because the impacts had not yet begun, the past events were not being evoked to draw comparisons to Harvey (except with forecasted meteorological impacts). Since the acute stage began alongside the meteorological impacts, users could see application of the past experiences they had with previous storms to the situation that was unfolding with Harvey. As the crisis shifted into the chronic stage, users could begin to reflect on the aftermath of Harvey, including the humanitarian crisis that persisted after the meteorological impacts had ended. By acknowledging that past events are evoked to help people process various stages of a present disaster they face, decision-makers could use this information to adjust crisis management practices across different stages of the disaster.

8.5.2 Individual Tropical Cyclones: Collective Storm Identities

By thematically assessing past event tweets by individual storms (section 8.3), these results suggest that some past events are referenced in the same ways by several users, indicating that they have a shared experience or memory of the event. This claim is supported by the collective identities that are developed by multiple users for some of the frequently-referenced LTCs. Even though Rita, Katrina, and Allison all took place over a decade before Harvey, many of the users share a common recollection of them, associating them with a common theme or idea—that is, evacuation failures, sociopolitical issues, and flood-producing rainfall (respectively). Given these shared long-term memories that were revealed in this dataset, it would be reasonable to anticipate that a collective view of Harvey would also stem from the users who experienced it, as would occur with future LTCs as well. Using this information, it is worth pondering how this knowledge might be used by communicators, such as broadcast meteorologists or emergency managers. Knowing that some LTCs have long-term shared memories tied to them, this information could assist with communication efforts in that the past event could be used to prepare the public for some aspect of the storm, such as flooding. However, certain aspects of LTCs are not always easy to predict (e.g., the evacuation disaster that unfolded with Rita was unexpected). Further, for LTC events that are poised to be unprecedented (as Harvey was in terms of rainfall totals), comparisons to crises embedded within the storm might be more challenging to design (particularly since even the communicators would not have a conceptual understanding of the magnitude of the impacts). Plus, any forecast will always have some element of uncertainty that could ultimately make leaders hesitant about making these comparisons. Nonetheless, evidence that the public can hold on to a collective vision of a past event is powerful knowledge because it shows that people not only consider these memories as they experience a new disaster, but also because it provides insight to political leaders, emergency managers, and forecasters on what the public is thinking about during these events.

In a similar way that the users studied here experience embedded overlapping hazards (e.g., tornadoes and flash floods) throughout the all-encompassing hazard (i.e., a LTC), the thematic analysis of the tweets referencing specific TCs also reveals that the users experience multiple overlapping crises (e.g., rising flood waters, political controversy) that are embedded within a primary crisis (i.e., Harvey). The results presented above show that Allison, Rita, and Katrina tend to be referenced during different time periods of the event, with each of them being associated with a crisis that unfolds during Harvey—that is, its historic rainfall, the criticism of political figures for evacuation decisions, and the transition from meteorological event to humanitarian crisis (respectively). Essentially, references to each of these events serve as a proxy for chronologically tracking between the embedded crises as they become the dominant issue in the overarching crisis, with discourse about the past event becoming amplified on social media as an analogous crisis in the current crisis unfolds. This finding is consistent with results shown in Morss et al. (2017) and Demuth et al. (2018). Additionally, this finding could once again be applicable to decision-makers, including emergency managers and political officials, as the past event references provide information on where the public's primary concerns lie at a given point of the event, which could allow leaders to continuously reassess the needs of the people that they serve. Given the relevance of past events to the evolving, overlapping crises embedded within a larger crisis, perhaps these past events could be implemented into existing algorithms that have been built to scrape information from Twitter than is pertinent to disaster response efforts (e.g. Ashktorab et al. 2014).

8.5.3 Individual Direct Experiences: Unique Visible and Invisible Impacts

By taking this analysis a step deeper to the individual users (section 8.4), the past event tweets suggest that experience is complex and varies significantly between users, with each person experiencing their own individual physical or emotional impacts from the past event that they describe. In other words, the users' own experiences (e.g., direct and indirect) with past weather-related events are dependent on the specific impacts they encountered—each of which is unique to them. Results show that these impacts are disruptive to each person's life in different ways, regardless of whether the impacts are tangible or intangible. It is important to recognize these nuances in past experiences as new crises unfold because it highlights that not all people hold the same picture of what an event looks like, and these viewpoints could differ depending on the impacts that the person sustained, which can depend on factors such as geographic location, resource availability, local infrastructure, and individual perceptions. As a recent example of this variability in experience, people who were impacted by Hurricane Ida in August 2021 when it first made landfall along the Gulf Coast could hold very different memories of the event than people residing in the northeast who witnessed the remnants of the storm. These varying experiences could be attributed to factors such as differences in primary meteorological hazards (e.g., storm surge and hurricane-force winds along the Gulf versus inland flash flooding and tornadoes in the Northeast) or variable impacts (e.g., long-term power outages for Gulf Coast residents versus short-term infrastructure flooding or deaths in flooded basement apartment in the Northeast). In Harvey, even though there were several commonalities amongst many of the users (e.g., long-term residents of a similar geographic area, direct experiences with the same LTCs), there are still unique details that are specific to an individual's experience. One implication may be that while decision-makers might garner information from the collective identities of past LTCs to use as analogs in conveying risk, they should recognize that each person enters a crisis with a unique collection of experiences, which may impact the ways in which they interpret information being disseminated to them.

Results also show that the visible and invisible impacts that the users experienced from past events are equally important, as they both to help them make sense of the events that they are experiencing with Harvey in real-time. The prevalence of the invisible impacts that were described (i.e., the intangible experiences) is particularly noteworthy, as these types of experiences have historically been focused on less in the literature than tangible experiences. This finding supports results described by Demuth et al. (2016), which highlighted the importance of considering both tangible and intangible impacts when characterizing experience with LTCs, particularly since they can occur independently of one another.

CHAPTER 9: CONCLUSIONS, LIMITATIONS, AND FUTURE WORK

9.1 Summary and Conclusion

In Part II of this thesis, discourse related to past weather-related events and experience was explored using Twitter data from a 12-day period in late August through early September, when Hurricane Harvey impacted the western Gulf Coast. Through many rounds of refinement, 158 tweets that referenced past meteorological events, specifically LTCs and/or the hazards that accompany them, were collected from a group of 39 users who identified as members of the public and resided in the hardest-hit regions of southeast Texas and southern Louisiana. Using this dataset of "past event tweets", this research sought to answer two questions:

> *Q1: How does experience emerge through the lens of the past event tweets during Hurricane Harvey?*
>
> *Q2: What are the different ways in which past events are discussed by users during the various stages of Hurricane Harvey?*

By exploring these questions and using Hurricane Harvey as the case, this work aims to address three less-investigated areas of the literature by 1) evaluating past events as a proxy for experience, 2) examining how past experiences evolve in real-time rather than after the disaster is over, and 3) contemplating the purposes for which past events are referenced while an event is occurring. To address these gaps, the past event tweets were examined thematically and over time using the Fink crisis model.

This analysis found that users attended to past events during Harvey for two main reasons: first, because they are important to them and they have a personal connection with them, and second to use them as analogs to help them to process, understand and/or discuss the events that are taking place around them in real-time. Section 8.2 shows that certain past events were referenced for various reasons, and the subject matter surrounding the past event tweets was largely connected to the events that occurred during different stages of Harvey. Section 8.3 shows that frequently mentioned storms tend to be associated with a particular aspect of them, effectively giving them an "identity". These identities were described by the users through the past event tweets to both highlight their connection with the storm as well as help them process the scenes that were unfolding with Harvey. Lastly, section 8.4 demonstrates that users reference past events throughout Harvey because they have a tangible or intangible direct experience with them, meaning that the storm they are referencing is personal to them.

In summary, past events can be used to reflect certain aspects of the crisis that is happening in the present. They can hold an identity that many people share, as well as be seen in a unique way depending on the individual experience that a person had with that event. Understanding that past weather-related events and experiences are being recalled and shared on social media can help provide insights to the thoughts and needs of the public as a severe weather event is unfolding, which is helpful to decision-makers throughout a crisis. Additionally, understanding these thought processes of the public can help communicators develop strategies to draw accurate comparisons between past events that the public has familiarity with, which would likely help many members of the public make sense of the current threat that they face.

Lastly, though not related to the analysis or discussed in Part II, there are a couple things that can be said about the past event tweets in relation to TORFFs in LTCs based on these results. For instance, the specific past events that were mentioned were either flood events or LTC events, rather than tornado outbreaks. It is hypothesized that this finding could result from tornado outbreaks not often being given specific names that they can be universally referred to as that they can be referred to as or or lack of tornado events altogether. Additionally, past event tweets do not mention tornadoes nearly as much as they mention flooding, suggesting that hazard may have been the primary focus of the users (at least when it came to also referencing past events). It seems that according to these results, it seems that users may have good analogs for several LTC events, but when it comes to TORFF events, users do not memorialize them in the same ways (if at all).

9.2 Challenges, Limitations, and Future Work

One of the first limitations of this study that needs to be addressed is the limited scope of the dataset that was developed. The methods for selecting the tweets that were used for this analysis began with only selecting users that made a tweet containing some variation of the words "tornado" and "flash flood" (i.e., "TORFF tweets") during the 12-day period. While this decision did help refine the dataset to users who were aware of overlapping hazards in Harvey and was a convenient choice given that the data had already been queried by a research team, it also likely eliminated many users who may have been tweeting about past events but did not send a TORFF tweet. Beginning the initial data search with different criteria may have yielded a slightly larger sample. Further, these results only come from a single LTC event. Each LTC brings different impacts of various magnitudes and presents its own unique challenges to different populations of people. The results described in this study may not apply to different LTC events given these nuances. Lastly, this analysis only sought to examine experience through the lens of past events, though past experiences may emerge in real-time during

LTCs in many other ways that were not explored here. Other methods may reveal more instances of indirect experiences (for example) which were difficult to identify in this particular dataset.

There are additional issues and concerns that can result from using Twitter data in research as a whole. While tweets are valuable data for scientific analysis, they can pose unique methodological challenges. One of these issues revolves around data availability. In this study, the content of the tweets is downloaded at a single point in time and organized into a spreadsheet. Because the data is downloaded, the tweet content remains accessible to researchers indefinitely, though some data may no longer be available on the Twitter platform at various points in time as a result of users deleting individual tweets, privatizing or deactivating their account, or being suspended by the site. This issue brings up two challenges with these methods: one being ethical concerns and the other being potential for misinterpretation of the available data. To address ethical concerns, the database was frequently monitored to ensure that deleted or privatized data were not used, and for data that were used for publication, efforts were made to protect user privacy by anonymizing users and altering their tweets slightly. While these steps are in disagreement with the requests of Twitter (Twitter 2021) and are not required given the public nature of the platform, they fall in agreement with recommendations of recent publications that discuss the ethical use of social media data in research (Evans et al. 2015; Fiesler and Proferes 2018). Ultimately, updating the database according to data availability must be a finite process in order to finish the study, meaning that some tweets may become inaccessible after results are published, but it is believed that the anonymization efforts will help to protect user identities even if their data is no longer publicly available on the platform. In addition to privacy concerns, deleted data can also increase chances for misinterpretation of the available data during contextual analysis due to missing information. While some of these misunderstandings are unavoidable due to the limited scope of social media data, remaining vigilant that assumptions are not made beyond what the content of the tweets provide is one way to curtail such issues.

There are a couple of additional concerns with use of Twitter data in disaster research, particularly with regards to the demographics of the sample population. For example, using this platform could exclude older adults, who are less likely to have social media accounts (Sloan et al. 2015; Wojcik and Hughes 2019), as well as people of lower socioeconomic status, who may have limited access to internet services and other technology. When data from the platform is used in disaster research specifically, the widespread extent of the damage in events such as Harvey could restrict internet access for an even larger population, including those that may be considered less vulnerable, which may affect the demographics of the sample users further. For similar reasons, users who are in particularly dire circumstances may be more focused on rescue and survival, rather than posting on social media, which would also exclude them from the sample[9]. Remaining aware of these biases and making targeted efforts to specifically include members of the general population who may not frequently appear on online platforms as often as others are some ways that the demographics can be made more diverse in studies using social media data.

With these shortcomings considered, future studies may consider methods to develop a system where hyperlinks to mined tweets are automatically updated in real time, so broken links would be flagged, meaning that tweets would not have to be manually monitored for deleted or unavailable

[9] However, many users did use social media for rescue purposes during Harvey specifically (e.g., Mihunov et al. 2020).

content. Future studies should also continue to seek ways to address the "digital divide" when using Twitter data, so all populations can be examined in detail. Determining other ways to mine Twitter for experience could also be explored. Additionally, these results focus on the discussion of these past experiences throughout a single evolving LTC, but there are many other applications where similar methods could be applied, such as with other weather-related events or over longer periods of time with many LTC events included. Lastly, there is ongoing work being conducted with the same public database described in this paper that aims to investigate themes surrounding overlapping tornado and flash flood events, which will provide additional insight on the social science side of overlapping hazards research.

REFERENCES

Anderson, J., and Coauthors, 2016: Far far away in far rockaway: Responses to risks and impacts during Hurricane Sandy through first-person social media narratives. *Proc. Int. ISCRAM Conf.*,.

Ashktorab, Z., C. Brown, M. Nandi, and A. Culotta, 2014: Tweedr: Mining twitter to inform disaster response. *ISCRAM 2014 Conf. Proc. - 11th Int. Conf. Inf. Syst. Cris. Response Manag.*, 354–358.

Ashley, S. T., and W. S. Ashley, 2008: Flood fatalities in the United States. *J. Appl. Meteorol. Climatol.*, **47**, 805–818, https://doi.org/10.1175/2007JAMC1611.1.

Ashley, W. S., 2007: Spatial and temporal analysis of tornado fatalities in the United States: 1880-2005. *Weather Forecast.*, **22**, 1214–1228, https://doi.org/10.1175/2007WAF2007004.1.

Bai, L., Z. Meng, K. Sueki, G. Chen, and R. Zhou, 2020: Climatology of tropical cyclone tornadoes in China from 2006 to 2018. *Sci. China Earth Sci.*, **63**, 37–51, https://doi.org/10.1007/s11430-019-9391-1.

Baker, K., 2018: Reflection on Lessons Learned: An Analysis of the Adverse Outcomes Observed during the Hurricane Rita Evacuation. *Disaster Med. Public Health Prep.*, **12**, 115–120, https://doi.org/10.1017/dmp.2017.27.

Benjamin, S. G., and Coauthors, 2016: A North American hourly assimilation and model forecast cycle: The rapid refresh. *Mon. Weather Rev.*, **144**, 1669–1694, https://doi.org/10.1175/MWR-D-15-0242.1.

Bica, M. and Coauthors 2021: "Can't Think of Anything More to Do": Public Displays of Power, Privilege, and Surrender in Social Media Disaster Monologues. *Human-Computer Interact.*, in press.

Blake, E. S., and D. A. Zelinsky, 2017: *National Hurricane Center Tropical Cycle Report: Hurricane Harvey*. 1–77 pp. https://www.nhc.noaa.gov/data/tcr/AL092017_Harvey.pdf.

Bluestein, H. B., J. C. Snyder, and J. B. Houser, 2015: A multiscale overview of the El Reno, Oklahoma, tornadic supercell of 31 May 2013. *Weather Forecast.*, **30**, 525–552, https://doi.org/10.1175/WAF-D-14-00152.1.

Brauer, N. S., J. B. Basara, C. R. Homeyer, G. M. McFarquhar, and P. E. Kirstetter, 2020: Quantifying precipitation efficiency and drivers of excessive precipitation in post-landfall hurricane harvey. *J. Hydrometeorol.*, **21**, 433–452, https://doi.org/10.1175/JHM-D-19-0192.1.

Brommer, D. M., and J. C. Senkbeil, 2010: Pre-landfall evacuee perception of the meteorological hazards associated with Hurricane Gustav. *Nat. Hazards*, **55**, 353–369, https://doi.org/10.1007/s11069-010-9532-7.

Burow, D., K. Ellis, and L. Tran, 2021: Simultaneous and collocated tornado and flash flood warnings associated with tropical cyclones in the contiguous United States. *Int. J. Climatol.*, 1–12, https://doi.org/10.1002/joc.7071.

Chappell, C. F., 1986: Quasi-Stationary Convective Events. *Mesoscale Meteorol. Forecast.*, 289–310, https://doi.org/10.1007/978-1-935704-20-1_13.

Cohen, A. E., 2010: Synoptic-scale Analysis of Tornado-Producing Tropical Cyclones Along the Gulf Coast. *Natl. Weather Dig.*, **34**, 99–115.

Curtis, L., 2004: Midlevel dry intrusions as a factor in Tornado outbreaks associated with landfalling tropical cyclones from the Atlantic and Gulf of Mexico. *Weather Forecast.*, **19**, 411–427, https://doi.org/10.1175/1520-0434(2004)019<0411:MDIAAF>2.0.CO;2.

Dart, T., 2017: Why did America’s biggest megachurch take so long to shelter Harvey victims? *The Gaurdian*.

Davis, R. S., 2001: Flash Flood Forecast and Detection Methods. *Sev. Convect. Storms*, 481–525, https://doi.org/10.1007/978-1-935704-06-5_12.

Demuth, J. L., 2018: Explicating experience: Development of a valid scale of past hazard experience for tornadoes. *Risk Anal.*, **38**, 1921–1943, https://doi.org/10.1111/risa.12983.

——, R. E. Morss, J. K. Lazo, and C. Trumbo, 2016: The effects of past hurricane experiences on evacuation intentions through risk perception and efficacy beliefs: A mediation analysis. *Weather. Clim. Soc.*, **8**, 327–344, https://doi.org/10.1175/WCAS-D-15-0074.1.

——, and Coauthors, 2018: ‘“Sometimes da #beachlife ain’t always da wave”’: Understanding People’s Evolving Hurricane Risk Communication, Risk Assessments, and Responses Using Twitter Narratives. *Weather. Clim. Soc.*, **10**, 537–560, https://doi.org/10.1175/wcas-d-17-0126.1.

Doswell, C. A., 1998: Seeing Supercells as Heavy Rain Producers. *Preprints, 14th Conf. on Hydrology, Dallas, TX*, 73–79 http://www.flame.org/~cdoswell/publications/Supercells_heavyrain.pdf.

——, H. E. Brooks, and R. A. Maddox, 1996: Flash Flood Forecasting: An Ingredients-Based Methodology. *Weather Forecast.*, **11**, 560–581, https://doi.org/10.1175/1520-0434(1996)011<0560:FFFAIB>2.0.CO;2.

Dougherty, E., and K. L. Rasmussen, 2019: Climatology of flood-producing storms and their associated rainfall characteristics in the United States. *Mon. Weather Rev.*, **147**, 3861–3877, https://doi.org/10.1175/MWR-D-19-0020.1.

Edwards, R., 2010: Tropical Cyclone Tornado Records For the Modernized NWS Era. *Preprints, 25th Conference on Severe Local Storms*, 1–9.

——, 2012: Tropical Cyclone Tornadoes: A Review of Knowledge in Research and Prediction. *Electron. J. Sev. Storms Meteorol.*, **7**, 1–61.

——, A. R. Dean, R. L. Thompson, and B. T. Smith, 2012: Convective modes for significant severe thunderstorms in the contiguous United States. Part III: Tropical cyclone tornadoes. *Weather Forecast.*, **27**, 1507–1519, https://doi.org/10.1175/WAF-D-11-00117.1.

Evans, H., S. Ginnis, and J. Bartlett, 2015: *#SocialEthics: A Guide to Embedding Ethics in Social Media Research*. https://www.ipsos.com/ipsos-mori/en-uk/ipsos-mori-and-demoscasm-call-better-ethical-standards-social-media-research.

Fiesler, C., and N. Proferes, 2018: "Participant" Perceptions of Twitter Research Ethics. *Soc. Media Soc.*, **4**, https://doi.org/10.1177/2056305118763366.

Fink, S., 1986: *Crisis Management: Planning for the Inevitable*. American Management Association,.

Fujita, T. T., K. Watanbe, K. Tsuchiya, and M. Shimada, 1972: Typhoon-Association Tornadoes in Japan and New Evidence of Suction Vortices in a Tornado Near Tokyo. *J. Meteorol. Soc. Japan*, **50**, 431–453, https://doi.org/10.2151/jmsj1965.50.5_431.

Galarneau, T. J., and X. Zeng, 2020: The hurricane harvey (2017) Texas rainstorm: Synoptic analysis and sensitivity to soil moisture. *Mon. Weather Rev.*, **148**, 2479–2502, https://doi.org/10.1175/MWR-D-19-0308.1.

Gao, S., J. Zhang, D. Li, H. Jiang, and Z. N. Fang, 2021: Evaluation of Multiradar Multisensor and Stage IV Quantitative Precipitation Estimates during Hurricane Harvey. *Nat. Hazards Rev.*, **22**, 04020057, https://doi.org/10.1061/(asce)nh.1527-6996.0000435.

Goldberg, M. H., J. R. Marlon, S. A. Rosenthal, and A. Leiserowitz, 2020: A Meta-Cognitive Approach to Predicting Hurricane Evacuation Behavior. *Environ. Commun.*, **14**, 6–12, https://doi.org/10.1080/17524032.2019.1687100.

Goodison, B., P. Y. T. Louie, and D. Yang, 1998: *WMO solid precipitation measurement intercomparison*. 318 pp.

Guzman, O., and H. Jiang, 2021: Global increase in tropical cyclone rain rate. *Nat. Commun.*, **12**, 1–8, https://doi.org/10.1038/s41467-021-25685-2.

Hall, T. M., and J. P. Kossin, 2019: Hurricane stalling along the North American coast and implications for rainfall. *Npj Clim. Atmos. Sci.*, **2**, 1–9, https://doi.org/10.1038/s41612-019-0074-8.

Helmus, J. J., and S. M. Collis, 2016: The Python ARM Radar Toolkit (Py-ART), a Library for Working with Weather Radar Data in the Python Programming Language. *J. Open Res. Softw.*, **4**, e25, https://doi.org/http://doi.org/10.5334/jors.119.

Henderson, J., E. R. Nielsen, G. R. Herman, and R. S. Schumacher, 2020: A hazard multiple: Overlapping tornado and flash flood warnings in a national weather service forecast office in the Southeastern United States. *Weather Forecast.*, **35**, 1459–1481, https://doi.org/10.1175/WAF-D-19-0216.1.

Hill, E. L., W. Malkin, and W. A. Schultz, 1966: Tornadoes Associated With Cyclones of Tropical Origin--Practical Features. *J. Appl. Meteorol.*, **5**, 745–763, https://doi.org/https://doi.org/10.1175/1520-0450(1966)005<0745:TAWCOT>2.0.CO;2.

Hitchens, N. M., and H. E. Brooks, 2013: Preliminary investigation of the contribution of supercell thunderstorms to the climatology of heavy and extreme precipitation in the United States. *Atmos. Res.*, **123**, 206–210, https://doi.org/10.1016/j.atmosres.2012.06.023.

Horney, J., C. Snider, S. Malone, L. Gammons, and S. Ramsey, 2008: Factors Associated with Hurricane Preparedness: Results of a Pre-Hurricane Assessment. *J. Disaster Res.*, **3**, 143–149, https://doi.org/10.20965/jdr.2008.p0143.

Huang, S.-K., M. K. Lindell, C. S. Prater, H.-C. Wu, and L. K. Siebeneck, 2012: Household Evacuation Decision Making in Response to Hurricane Ike. *Nat. Hazards Rev.*, **13**, 283–296, https://doi.org/10.1061/(asce)nh.1527-6996.0000074.

Jan, T., and B. Martin, 2017: Houston took them in after Katrina. Then Harvey hit. *Washington Post*.

Jing, Z., and G. Wierner, 1993: Two-Dimensional Dealiasing of Doppler Velocities. *J. Atmos. Ocean. Technol.*, **10**, 798–808.

Keene, K. M., and R. S. Schumacher, 2013: The bow and arrow mesoscale convective structure. *Mon. Weather Rev.*, **141**, 1648–1672, https://doi.org/10.1175/MWR-D-12-00172.1.

King, A. P., and R. J. Eckersley, 2019: Inferential Statistics III: Nonparametric Hypothesis Testing. *Stat. Biomed. Eng. Sci.*, 119–145, https://doi.org/10.1016/b978-0-08-102939-8.00015-3.

Knight, D. B., and R. E. Davis, 2009: Contribution of tropical cyclones to extreme rainfall events in the southeastern United States. *J. Geophys. Res. Atmos.*, **114**, 1–17, https://doi.org/10.1029/2009JD012511.

Knox, J. A., B. Mazanec, E. Sullivan, S. Hall, and J. A. Rackley, 2016: Analysis of the Twitter Response to Superstorm Sandy: Public Perceptions, Misconceptions, and Reconceptions of an

Extreme Atmospheric Hazard. *Atmos. Hazards*, **32**, 21–40.

Kogan, M., and L. Palen, 2018: Conversations in the eye of the storm: At-scale features of conversational structure in a high-tempo, high-stakes microblogging environment. *Conf. Hum. Factors Comput. Syst. - Proc.*, 1–13, https://doi.org/10.1145/3173574.3173658.

Kossin, J. P., 2018: A global slowdown of tropical-cyclone translation speed. *Nature*, **558**, 104–107, https://doi.org/10.1038/s41586-018-0158-3.

Lakshmanan, V., T. Smith, K. Hondl, G. J. Stumpf, and A. Witt, 2006: A real-time, three-dimensional, rapidly updating, heterogeneous radar merger technique for reflectivity, velocity, and derived products. *Weather Forecast.*, **21**, 802–823, https://doi.org/10.1175/WAF942.1.

——, C. Karstens, J. Krause, and L. Tang, 2014: Quality control of weather radar data using polarimetric variables. *J. Atmos. Ocean. Technol.*, **31**, 1234–1249, https://doi.org/10.1175/JTECH-D-13-00073.1.

Landsea, C. W., and J. L. Franklin, 2013: Atlantic hurricane database uncertainty and presentation of a new database format. *Mon. Weather Rev.*, **141**, 3576–3592, https://doi.org/10.1175/MWR-D-12-00254.1.

Larson, J., Y. Zhou, and R. W. Higgins, 2005: Characteristics of landfalling tropical cyclones in the United States and Mexico: Climatology and interannual variability. *J. Clim.*, **18**, 1247–1262, https://doi.org/10.1175/JCLI3317.1.

Latto, A., and R. Berg, 2020: *National Hurricane Center Tropical Cyclone Report: Tropical Storm Imelda*. 1–28 pp.

Li, L., and P. Chakraborty, 2020: Slower decay of landfalling hurricanes in a warming world. *Nature*,

587, 230–234, https://doi.org/10.1038/s41586-020-2867-7.

Maddox, R. A., C. F. Chappell, and L. R. Hoxit, 1979: Synoptic and Meso-α Scale Aspects of Flash Flood Events. *Bull. Am. Meteorol. Soc.*, **60**, 115–123.

Mahalik, M. C., B. R. Smith, K. L. Elmore, D. M. Kingfield, K. L. Ortega, and T. M. Smith, 2019: Estimates of gradients in radar moments using a linear least squares derivative technique. *Weather Forecast.*, **34**, 415–434, https://doi.org/10.1175/WAF-D-18-0095.1.

May, R. M., S. C. Arms, P. Marsh, E. Bruning, J. R. Leeman, K. Goebbert, J. E. Thielen, and Z. Bruick, 2021: MetPy: A Python Package for Meteorological Data. *Unidata*, https://doi.org/10.5065/D6WW7G29.

McCaul, E. W., 1991: Buoyancy and Shear Characteristics of Hurricane-Tornado Environments. *Mon. Weather Rev.*, **119**, 1954–1978.

Mihunov, V. V., N. S. N. Lam, L. Zou, Z. Wang, and K. Wang, 2020: Use of Twitter in disaster rescue: lessons learned from Hurricane Harvey. *Int. J. Digit. Earth*, **13**, 1454–1466, https://doi.org/10.1080/17538947.2020.1729879.

Miller, M. L., V. Lakshmanan, and T. M. Smith, 2013: An automated method for depicting mesocyclone paths and intensities. *Weather Forecast.*, **28**, 570–585, https://doi.org/10.1175/WAF-D-12-00065.1.

Moller, A. R., C. A. Doswell, and G. Woodall, 1994: The Operational Recognition of Supercell Thunderstorm Environments and Storm Structures. *Weather Forecast.*, **9**, 327–347.

Moore, T. W., and R. W. Dixon, 2011: Climatology of tornadoes associated with gulf coast-landfalling hurricanes. *Geogr. Rev.*, **101**, 371–395, https://doi.org/10.1111/j.1931-

0846.2011.00102.x.

——, and ——, 2013: Preliminary analysis of the synoptic-scale environment associated with tropical cyclone tornado clusters, 1995-2010. *Pap. Appl. Geogr.*, **36**, 1–10.

——, and ——, 2015: Patterns in 500 hPa geopotential height associated with temporal clusters of tropical cyclone tornadoes. *Meteorol. Appl.*, **22**, 314–322, https://doi.org/10.1002/met.1456.

——, N. J. Sokol, and R. A. Blume, 2017: Spatial distributions of tropical cyclone tornadoes by intensity and size characteristics. *Atmosphere (Basel).*, **8**, 5–7, https://doi.org/10.3390/atmos8090160.

Morss, R. E., and Coauthors, 2017: Hazardous weather prediction and communication in the modern information environment. *Bull. Am. Meteorol. Soc.*, **98**, 2653–2674, https://doi.org/10.1175/BAMS-D-16-0058.1.

Nielsen, E. R., and R. S. Schumacher, 2018: Dynamical Insights into Extreme Short-Term Precipitation Associated with Supercells and Mesovortices. *J. Atmos. Sci.*, **75**, 2983–3009, https://doi.org/10.1175/JAS-D-17-0385.1.

——, and ——, 2020a: Observations of extreme short-term precipitation associated with supercells and mesovortices. *Mon. Weather Rev.*, **148**, 159–182, https://doi.org/10.1175/MWR-D-19-0146.1.

——, and ——, 2020b: Dynamical Mechanisms Supporting Extreme Rainfall Accumulations in the Houston "Tax Day" 2016 Flood. *Mon. Weather Rev.*, **148**, 83–109, https://doi.org/10.1175/mwr-d-19-0206.1.

——, G. R. Herman, R. C. Tournay, J. M. Peters, and R. S. Schumacher, 2015: Double impact:

When both tornadoes and flash floods threaten the same place at the same time. *Weather Forecast.*, **30**, 1673–1693, https://doi.org/10.1175/WAF-D-15-0084.1.

NOAA, 2020: Weather Fatalities 2020. https://www.weather.gov/hazstat/.

NOAA National Centers for Environmental Information, 2021a: NCEI Storm Events Database. https://www.ncdc.noaa.gov/stormevents/.

——, 2021b: U.S. Billion-dollar Weather and Climate Disasters, 1980 - present. *Natl. Centers Environ. Inf.*, https://doi.org/10.25921/STKW-7W73.

NOAA National Hurricane Center, Tropical Cyclone Naming History and Retired Names. https://www.nhc.noaa.gov/aboutnames_history.shtml.

NOAA National Ocean Service, 2021: NOAA Hurricane Tracks.

Novlan, D. J., and W. M. Gray, 1974: Hurricane-Spawned Tornadoes. *Mon. Weather Rev.*, **102**, 476–488, https://doi.org/10.1175/1520-0493(1974)102<0476:hst>2.0.co;2.

Palen, L., and K. M. Anderson, 2016: Crisis informatics—New data for extraordinary times. *Science (80-.).*, **353**, 224–225, https://doi.org/10.1126/science.aag2579.

——, and A. L. Hughes, 2018: Social media in disaster communication. *Handbook of Disaster Research*, Springer International Publishing, 497–518.

Parker, M. D., and R. H. Johnson, 2000: Organizational modes of midlatitude mesoscale convective systems. *Mon. Weather Rev.*, **128**, 3413–3436, https://doi.org/10.1175/1520-0493(2001)129<3413:OMOMMC>2.0.CO;2.

Rappaport, E. N., 2014: Fatalities in the united states from atlantic tropical cyclones: New data and interpretation. *Bull. Am. Meteorol. Soc.*, **95**, 341–346, https://doi.org/10.1175/BAMS-D-12-

00074.1.

Rasmussen, R., and Coauthors, 2012: How well are we measuring snow: The NOAA/FAA/NCAR winter precipitation test bed. *Bull. Am. Meteorol. Soc.*, **93**, 811–829, https://doi.org/10.1175/BAMS-D-11-00052.1.

Rickard, L. N., Z. J. Yang, J. P. Schuldt, G. M. Eosco, C. W. Scherer, and R. A. Daziano, 2017: Sizing Up a Superstorm: Exploring the Role of Recalled Experience and Attribution of Responsibility in Judgments of Future Hurricane Risk. *Risk Anal.*, **37**, 2334–2349, https://doi.org/10.1111/risa.12779.

Rogash, J. A., and R. D. Smith, 2000: Multiscale overview of a violent tornado outbreak with attendant flash flooding. *Weather Forecast.*, **15**, 416–431, https://doi.org/10.1175/1520-0434(2000)015<0416:MOOAVT>2.0.CO;2.

Rogash, J. A., and J. Racy, 2002: Some meteorological characteristics of significant tornado events occurring in proximity to flash flooding. *Weather Forecast.*, **17**, 155–159, https://doi.org/10.1175/1520-0434(2002)017<0155:SMCOST>2.0.CO;2.

Sastry, N., and J. Gregory, 2014: The Location of Displaced New Orleans Residents in the Year After Hurricane Katrina. *Demography*, **51**, 753–775, https://doi.org/10.1007/s13524-014-0284-y.

Schultz, L. A., and D. J. Cecil, 2009: Tropical cyclone tornadoes, 1950-2007. *Mon. Weather Rev.*, **137**, 3471–3484, https://doi.org/10.1175/2009MWR2896.1.

Schumacher, R. S., 2017: Heavy Rainfall and Flash Flooding. *Oxford Research Encyclopedia of Natural Hazard Science*, Oxford University Press.

——, and R. H. Johnson, 2005: Organization and Environmental Properties of Extreme-Rain-

Producing Mesoscale Convective Systems. *Mon. Weather Rev.*, **133**, 961–976, https://doi.org/10.1175/MWR2899.1.

——, and ——, 2006: Characteristics of U.S. extreme rain events during 1999-2003. *Weather Forecast.*, **21**, 69–85, https://doi.org/10.1175/WAF900.1.

——, and ——, 2009: Quasi-stationary, extreme-rain-producing convective systems associated with midlevel cyclonic circulations. *Weather Forecast.*, **24**, 555–574, https://doi.org/10.1175/2008WAF2222173.1.

Senkbeil, J. C., and D. Schneider, 2010: Hurricane and Tornado Hazard Competency in Alabama. *Pap. Appl. Geogr. Conf.*, **33**, 128–136.

Sloan, L., J. Morgan, P. Burnap, and M. Williams, 2015: Who tweets? deriving the demographic characteristics of age, occupation and social class from twitter user meta-data. *PLoS One*, **10**, 1–20, https://doi.org/10.1371/journal.pone.0115545.

Smith, J. A., M. L. Baeck, Y. Zhang, and C. A. Doswell, 2001: Extreme rainfall and flooding from supercell thunderstorms. *J. Hydrometeorol.*, **2**, 469–489, https://doi.org/10.1175/1525-7541(2001)002<0469:ERAFFS>2.0.CO;2.

Smith, T. M., and K. L. Elmore, 2004: The use of radial velocity derivative to diagnose rotation and divergence. *11th Conference on Aviation, Range, and Aerospace*, Hyannis, American Meteorological Society, 5.6 https://ams.confex.com/ams/11aram22sls/techprogram/paper_81827.htm.

——, and Coauthors, 2016: Multi-Radar Multi-Sensor (MRMS) severe weather and aviation products: Initial Operating Capabilities. *Bull. Am. Meteorol. Soc.*, **97**, 1617–1630, https://doi.org/10.1175/BAMS-D-14-00173.1.

Spence, P. R., K. A. Lachlan, X. Lin, and M. del Greco, 2015: Variability in Twitter Content Across the Stages of a Natural Disaster: Implications for Crisis Communication. *Commun. Q.*, **63**, 171–186, https://doi.org/10.1080/01463373.2015.1012219.

Sukovich, E. M., F. M. Ralph, F. E. Barthold, D. W. Reynolds, and D. R. Novak, 2014: Extreme quantitative precipitation forecast performance at the weather prediction center from 2001 to 2011. *Weather Forecast.*, **29**, 894–911, https://doi.org/10.1175/WAF-D-13-00061.1.

Takahashi, B., E. C. Tandoc, and C. Carmichael, 2015: Communicating on Twitter during a disaster: An analysis of tweets during Typhoon Haiyan in the Philippines. *Comput. Human Behav.*, **50**, 392–398, https://doi.org/10.1016/j.chb.2015.04.020.

Trumbo, C., M. Lueck, H. Marlatt, and L. Peek, 2011: The Effect of Proximity to Hurricanes Katrina and Rita on Subsequent Hurricane Outlook and Optimistic Bias. *Risk Anal.*, **31**, 1907–1918, https://doi.org/10.1111/j.1539-6924.2011.01633.x.

Twitter, 2021: Display Requirements: Tweets. *Twitter Dev. Platf.*,. https://developer.twitter.com/en/developer-terms/display-requirements.

United States Census Bureau, 2019: *2019 County Metro Population Estimates*. https://www.census.gov/newsroom/press-kits/2020/pop-estimates-county-metro.html.

Velden, C. S., and L. M. Leslie, 1991: The Basic Relationship between Tropical Cyclone Intensity and the Depth of the Environmental Steering Layer in the Australian Region. *Weather Forecast.*, **6**, 244–253.

Vera-Burgos, C. M., and D. R. Griffin Padgett, 2020: Using Twitter for crisis communications in a natural disaster: Hurricane Harvey. *Heliyon*, **6**, 0–9, https://doi.org/10.1016/j.heliyon.2020.e04804.

Verbout, S. M., D. M. Schultz, L. M. Leslie, H. E. Brooks, D. J. Karoly, and K. L. Elmore, 2007: Tornado outbreaks associated with landfalling hurricanes in the North Atlantic Basin: 1954-2004. *Meteorol. Atmos. Phys.*, **97**, 255–271, https://doi.org/10.1007/s00703-006-0256-x.

Vieweg, S., A. L. Hughes, K. Starbird, and L. Palen, 2010: Microblogging during two natural hazards events: What twitter may contribute to situational awareness. *Conf. Hum. Factors Comput. Syst. - Proc.*, **2**, 1079–1088, https://doi.org/10.1145/1753326.1753486.

Virtanen, P., and Coauthors, 2020: SciPy 1.0: Fundamental Algorithms for Scientific Computing in Python. *Nat. Methods*, **17**, 261–272.

Wang, C. C., H. C. Kuo, R. H. Johnson, C. Y. Lee, S. Y. Huang, and Y. H. Chen, 2015: A numerical study of convection in rainbands of Typhoon Morakot (2009) with extreme rainfall: Roles of pressure perturbations with low-level wind maxima. *Atmos. Chem. Phys.*, **15**, 11097–11115, https://doi.org/10.5194/acp-15-11097-2015.

Weather Prediction Center, Tropical Cyclone Rainfall Maxima. https://www.wpc.ncep.noaa.gov/tropical/rain/tcmaxima.html).

Wilcoxon, F., 1946: Individual comparisons of grouped data by ranking methods. *J. Econ. Entomol.*, **39**, 269, https://doi.org/10.1093/jee/39.2.269.

Wojcik, S., and A. Hughes, 2019: Sizing Up Twitter Users. *Pew Research*.

Xu, Z., K. Lachlan, L. Ellis, and A. M. Rainear, 2019: Understanding public opinion in different disaster stages: a case study of Hurricane Irma. *Internet Res.*, **30**, 695–709, https://doi.org/10.1108/INTR-12-2018-0517.

Zhang, J., Y. Qi, C. Langston, and B. Kaney, 2012: Radar Quality Index (RQI) - A combined measure for beam blockage and VPR effects in a national network. *IAHS-AISH Publ.*, **351**, 388–393.

——, and Coauthors, 2016: Multi-Radar Multi-Sensor (MRMS) quantitative precipitation estimation: Initial operating capabilities. *Bull. Am. Meteorol. Soc.*, **97**, 621–638, https://doi.org/10.1175/BAMS-D-14-00174.1.

——, L. Tang, S. Cocks, P. Zhang, A. Ryzhkov, K. Howard, C. Langston, and B. Kaney, 2020: A dual-polarization radar synthetic QPE for operations. *J. Hydrometeorol.*, **21**, 2507–2521, https://doi.org/10.1175/JHM-D-19-0194.1.

Zou, L., and Coauthors, 2019: Social and geographical disparities in Twitter use during Hurricane Harvey. *Int. J. Digit. Earth*, **12**, 1300–1318, https://doi.org/10.1080/17538947.2018.1545878.